BONNER METEOROLOGISCHE ABHANDLUNGEN

Heft 91 (2020) (ISSN 0006-7156)
Herausgeber: Andreas Hense

Mari Luna Schmidt

IMPROVEMENT OF HAIL DETECTION AND NOWCASTING BY SYNERGISTIC COMBINATION OF INFORMATION FROM POLARIMETRIC RADAR, MODEL PREDICTIONS, AND IN-SITU OBSERVATIONS

BONNER METEOROLOGISCHE ABHANDLUNGEN

Heft 91 (2020) (ISSN 0006-7156)
Herausgeber: Andreas Hense

Mari Luna Schmidt

IMPROVEMENT OF HAIL DETECTION AND NOWCASTING BY SYNERGISTIC COMBINATION OF INFORMATION FROM POLARIMETRIC RADAR, MODEL PREDICTIONS, AND IN-SITU OBSERVATIONS

Improvement of hail detection and nowcasting by synergistic combination of information from polarimetric radar, model predictions, and in-situ observations

Dissertation
zur
Erlangung des Doktorgrades (Dr. rer. nat.)
der
Mathematisch-Naturwissenschaftlichen Fakultät
der
Rheinischen Friedrich-Wilhelms-Universität Bonn

vorgelegt von
Mari Luna Schmidt
aus
Speyer, Rheinland-Pfalz

Bonn, März, 2020

Diese Arbeit ist die ungekürzte Fassung einer der Mathematisch-Naturwissenschaftlichen Fakultät der Rheinischen Friedrich-Wilhelms-Universität Bonn im Jahr 2020 vorgelegten Dissertation von Mari Luna Schmidt aus Speyer, Rheinland-Pfalz.

This paper is the unabridged version of a dissertation thesis submitted by Mari Luna Schmidt born in Speyer, Rheinland-Pfalz to the Faculty of Mathematical and Natural Sciences of the Rheinischen Friedrich-Wilhelms-Universität Bonn in 2020.

Anschrift der Verfasserin: Address of the author:

Mari Schmidt
Institut für Geowissenschaften, Abt. Meteorologie
Universität Bonn
Auf dem Hügel 20
D-53121 Bonn

1. Gutachterin: PD Dr. Silke Trömel,
Rheinische Friedrich-Wilhelms-Universität Bonn
2. Gutachter: Prof. Dr. Clemens Simmer,
Rheinische Friedrich-Wilhelms-Universität Bonn

Tag der Promotion: 21. August 2020
Erscheinungsjahr: 2020

Abstract

Large hail can pose a major threat to people, infrastructure, and property. While polarimetric radar observations enable us to reliably detect hail, discrimination of hail size and strategies to nowcast and predict hail and its size are still subject of research. At S band hail size discrimination algorithms do already exist, while retrievals from C-band radars, which are more widespread in Europe, remain challenging due to resonance scattering effects from large raindrops which tend to interfere with large hail signatures.

Advanced nowcasting tools capable of detecting hail and discriminating its size at C band are required to enable earlier and more precise severe weather warnings being issued by weather services in Europe.

In this thesis 16 severe hail events monitored with the polarimetric C-band radar network of the German national meteorological service (*Deutscher Wetterdienst*, DWD) are investigated together with hail reports from the European Severe Weather Database (ESWD; https://www.eswd.eu/) for precursory information. This data set includes the largest hailstone (14.1 cm in diameter) reported so far in Germany hitting the ground in Undingen on August 6, 2013.

First, an algorithm for correcting anomalously high attenuation in hail-bearing thunderstorms is evaluated using four overlapping C-band radars. Post-processing of polarimetric moments, like spike-filtering of differential phase, is done to reduce noise and improve attenuation corrections. Results illustrate the capability to mitigate attenuation of up to $15\,\mathrm{dB\,km^{-1}}$ but only small overcorrection in precipitation without hail.

Second, T-matrix scattering simulations for dry and wet hail are conducted to adjust a fuzzy logic based hail size discrimination algorithm (HSDA) developed for S band for usage at C band. Hereby, dual-layered spheroids are simulated to mimic melting hail. The revised fuzzy logic utilizes an *ad-hoc* weighting of input variables to improve performance through self-adjustment similar to other unsupervised learning techniques.

Finally, hail precursors and storm dynamics are investigated in an object-based, precipitation system oriented analysis to develop and evaluate nowcasting tools to detect hail growth and predict the hail's terminal diameter. This analysis utilizes a custom-made cell tracker and exploits the results of the attenuation correction algorithm.

Results show that sudden increases of the vertical extent of columns of enhanced differential reflectivity Z_{DR}, so called Z_{DR}-columns, precede peaks of strong signal

attenuation most probably linked to hail. Also, strong attenuation was often accompanied by specific differential phase K_{DP} above $10\,^{\circ}\,\mathrm{km}^{-1}$. It is demonstrated that the intensity of Z_{DR}-columns, described e.g. by their maximum Z_{DR} value, and the height of Z_{DR}-columns above the melting layer, allow for nowcasting hail size at the ground with lead times between 10 and 20 minutes, which can be exploited for warnings.

Contents

Chapter 1

Introduction

Hail is a frequently occurring and potentially destructive phenomenon especially during mid-latitude summertime convective events, for which hail stones with diameters of up to 15 cm have been reported (Púčik et al., 2019). Detection of potentially damaging hail and its distinction from smaller, less or non-damaging hail is crucial for warnings, but still difficult to achieve. Methods to discriminate hail size exist for S-band radars (e.g. Ryzhkov et al., 2013b), but not yet for C band, the wavelength of weather radars mostly used in Europe. Also, except for advecting hail-bearing storms based on their previous tracks (e.g. Hering et al., 2004), nowcasting schemes do not predict hail growth yet. In this thesis, insights from published research of hail size discrimination, research on hailstorm dynamics and hail growth analysis are used to investigate nowcasting and size discrimination of hail.

Precipitation radar observations provide the most important information source for detecting and monitoring hail aloft, and thus also for predicting hail before it reaches the ground. Already since the 1960s non-polarimetric weather radar observations have been successfully applied for detecting hail aloft (e.g. Waldvogel et al., 1979). Witt et al. (1998a) used non-polarimetric reflectivity and the melting layer height to estimate the maximum expected hail size (MESH) and the probability of severe (large) hail (POSH).

Early polarimetric radar experiments have shown that polarimetric variables, especially the differential reflectivity Z_{DR}, are quite useful to detect hail at S band (e.g. Bringi et al., 1984; Aydin et al., 1986). Over the years methods and techniques became more advanced and complemented each other, like different algorithms and improvements for hydrometeor classification (e.g. Vivekanandan et al., 1999; Ryzhkov et al., 2005a; Park et al., 2009; Ortega et al., 2016). Also, new useful measures or variables were introduced, such as empiric quantities like a "hail signal" (H_{DR}; Aydin et al., 1986) and intrinsic radar variables like the linear depolarization ratio (LDR; Zrnić and Ryzhkov, 1999).

Dual-wavelength approaches to detect hail yielded notable results even before polarimetric radars became more common (e.g. Eccles and Atlas, 1973). The difference in reflectivity factor in hail measured with different wavelengths is a good indicator for hail (see e.g. Figure 1 in Kaltenboeck and Ryzhkov, 2013). Specifically,

hail can be easily detected by comparing reflectivity factors of e.g. C-band and S-band radars, if they are observing the same hail-bearing event. However, co-located S- and C-band radar sites are rare, due to their cost.

Detection of hail and especially discrimination of hail size is a crucial task for warnings. Park et al. (2009) published a commonly used hydrometeor classification based on fuzzy logic. Each polarimetric radar variable used is fuzzificated into hydrometeor-class specific membership functions. These membership functions approximate the probability distribution for each hydrometeor class to be the dominant hydrometeor type in the radar volume. If no further restrictions are applied, the class with the highest aggregated value, i.e. the highest likelihood that this class is associated with the measured polarimetric variables, is then selected. Similar to a hydrometeor classification, Ryzhkov et al. (2013b) introduced a hail size discrimination algorithm (HSDA) using a fuzzy logic on horizontal reflectivity factor Z_h, differential reflectivity Z_{DR}, and co-polar correlation coefficient ρ_{hv}. Ortega et al. (2016) refined the original HSDA by modifying membership functions, adding Z_h-dependency to the membership functions and defining height-dependent weights for the polarimetric variables, among other modifications. The performance of the modified HSDA compared with ground truth was assessed using the probability of detection (POD), false-alarm ratio (FAR) and the so called critical success index (CSI) (Doswell et al., 1990; Schaefer, 1990). A search window of 4 km $\times$ 4 km was applied, as point matches scored POD below 0.2. Telephone surveys during the Severe Hazards Analysis and Verification Experiment (Ortega et al., 2009) provided the ground truth for 79 cases with 2142 hail reports. For 0.5° elevation scans, the algorithm outperformed the original HSDA and reached a POD of 0.594, a FAR of 0.136 and a CSI of 0.432, although reports of no-hail were discarded for scoring (Ortega et al., 2016). This HSDA became operational and is evaluated at S band only. It is expected that the principle of the HSDA might also work for other wavelengths with approved adjustment of the membership functions (Ryzhkov et al., 2013b).

Suitable nowcasting schemes are still largely unexplored except for the extrapolation of previous radar measurements into the future by exploiting previous storm cell tracks and storm intensity (e.g. Dixon and Wiener, 1993; Hering et al., 2004). These methodologies, however, lack representation of hail growth and advection processes and therefore can only nowcast already observed hail. Numerical weather prediction (NWP) models can simulate these processes, e.g. Adams-Selin and Ziegler (2016) applied a hail growth and melting model to a storm resolving NWP model. Numerical prediction of the near-storm environment can be used to forecast changes in the development of thunderstorms, too (e.g. James et al., 2018). Precursor signals for hail could enhance the performance of radar-based nowcasting schemes without requiring computational effort of a NWP. Formation of hail requires updrafts of convective storm cells (Kennedy et al., 2001). Knowledge of the location and strength of the updraft in a storm may improve the lead time for hailstorm warnings.

Ideas to base hail detection and prediction on vertical columns of enhanced differential reflectivity, so called Z_{DR}-columns, have been proposed (e.g. Picca et al., 2010; Kumjian et al., 2014; Snyder et al., 2015, ...). Picca et al. (2010) were among the first connecting Z_{DR}-column intensification with subsequent hail occurrence, and found time lags of about 20 min between increases in Z_{DR}-column height and horizontal reflectivity Z_H in super-cell storms. Simulations by Kumjian et al. (2014) resulted in peak Z_{DR}-column heights occurring between 12.5 and 15 min before peaks of maximal hail mass at the surface (see their Table 1). Ilotoviz et al. (2018) found highest correlations between maximum Z_{DR} above 0 °C and hail parameters, like mass and size, for a time lag of 15 min. These results are in line with the time required for large hail to grow (diameter $\geq$ 2.5 cm) (Ziegler et al., 1983; Miller et al., 1988, 1990; Kennedy et al., 2001). Simulations by Ziegler et al. (1983) indicate a growth time of around 10 min for hail $\leq$ 2 cm, while larger hail usually takes at least 15 min to 20 min to grow (Miller et al., 1990). Most of these advanced studies (e.g. Kumjian et al. (2014), Ilotoviz et al. (2018)) were carried out with spectral bin microphysical models. These models were compared with radar derived statistics for plausibility. However, actual radar observations were not primarily used to investigate the preceding Z_{DR}-column intensification prior to hail occurrence, except for single case studies like Picca et al. (2010).

The Circular Depolarization Ratio (CDR) is also discussed to be a good indicator or precursor for strong updrafts because of its relation to the shape of the hydrometeor with a lower dependency on the hydrometeor orientation (Ryzhkov et al., 2017). However, compared to K_{DP} and Z_{DR}, propagation effects impair CDR and have to be low in order for CDR to be usable (Ryzhkov et al., 2014; Matrosov, 2004). According to simulation results a change in maximal hail diameter from 8 mm to 50 mm increases CDR by up to 15 dB (Ryzhkov et al., 2014). CDR signals are stronger than Z_{DR}-columns or Linear Depolarization Ratio (LDR) signals. Moreover, CDR exhibits updraft signatures up to greater heights than Z_{DR}-columns (Ryzhkov et al., 2017, 17f). For hail nowcasting, the use of CDR could improve the capability of detecting large hail already during formation (below, in and even above the melting layer). However, CDR is still underutilized for several reasons: In the past, it was not possible to obtain CDR from radars operating in a simultaneous transmission / reception mode, which is a requirement for Z_{DR}. Matrosov (2004) published a method to estimate CDR even with simultaneous transmission / reception, when the phase difference between horizontal and vertical channels is 90° on transmission and −90° on reception. Furthermore, "correction of CDR for differential phase is a big challenge which is one of the reasons why CDR has never been used for operational meteorological applications" (Ryzhkov et al., 2014). Indeed, intrinsic CDR is influenced strongly by differential phase (see Figure 1 in Ryzhkov et al., 2014). However, Ryzhkov et al. (2014) provide an algorithm to estimate CDR without strong dependence on the differential phase, when the complex voltages of the returned signal are available, i.e. applicable in the signal processor. According to Ryzhkov et al.

(2017), CDR can be estimated from other polarimetric variables (Z_{DR}, LDR and the cross-correlation coefficient ρ_{hv}).

Another hail precursor are K_{DP}-columns, which are emphasized to be useful especially in high attenuated cases, because K_{DP} is dependent on the phase, and thus less affected by attenuation (Kumjian and Ryzhkov, 2008; van Lier-Walqui et al., 2016). In one of the first studies, Hubbert et al. (1998) associated K_{DP}-columns with the shedding of water from wet hail. Loney et al. (2002) approved this assumption using additional airborne, *in-situ* measurements. Similar to Z_{DR}-columns, K_{DP}-columns appear as "columnar regions of enhanced positive KDP in convective storms that frequently extend several kilometers above the freezing level" (Kumjian and Ryzhkov, 2008, p. 1950). K_{DP}-columns might be more pronounced than Z_{DR}-columns, however, Z_{DR}-columns often precede the K_{DP}-column signature since Z_{DR}-columns are proxies for updrafts and K_{DP}-columns are associated with strong precipitation originating from the updraft. Thus, less lead time improvement could be achieved compared to other hail precursors like Z_{DR}-columns. Moreover, all cases using K_{DP}-columns were so far investigated at S band. E.g. Kumjian and Ryzhkov (2008) also provide observations at C band, but no K_{DP}-columns were identified there. Apparently, clear-cut cases with K_{DP}-columns are difficult to find at C band.

Scattering simulations help to interpret radar observations and to test theories against observations. Hydrometeor classification and hail size discrimination algorithms like Park et al. (2009) and Ryzhkov et al. (2013b) require reliable parameters for their membership functions. Setting these up without simulations would require numerous cases with fully verified ground truth, precise timing and location, as well as airborne *in-situ* measurements. Therefore, scattering simulations provide a comfortable way to generate a comprehensive data base for polarimetric signatures of hail. For dry hail, simulations of a single layered spheroid (e.g. Leinonen, 2014) are sufficient. For melting particles, especially for large melting hail, however, simulations based on a double layered spheroid (e.g. spongy ice core with a water layer) are necessary for a more realistic representation (Ryzhkov et al., 2010). Scattering simulations advanced over the years, but the transmission matrix defined by Waterman (1971) is still the basis of current simulation codes. Schemes to compute scattering for layered, non-spherical particles and methods to cope with numerical instabilities using this approach are described in Mishchenko et al. (1996). This led to a FORTRAN code (Mishchenko, 2000), which is still used in modern scattering simulations (e.g. by Leinonen, 2014).

The main goal of this research is to develop a nowcasting suite capable of discriminating hail size at C band. Hail detection and size discrimination are investigated by adjusting the S band HSDA to C band, exploiting the higher sensitivity of this wavelength during hail. Additionally, precursors of hail like columnar regions of Z_{DR}, K_{DP} or CDR are investigated for their nowcasting capabilities using a polarimetric C-band radar network. Finally, hail occurrence reports from the European Severe Weather Database (ESWD) are used for improving algorithms and

evaluation.

To tackle these objectives, the thesis aims to answer the following research questions:

1. How accurately can the location and size of hail be determined from polarimetric C-band radar observations and what additional information from other sources is required?

2. What are the most robust precursors for large hail, how can they be exploited for nowcasting and which lead times can be achieved?

Following this introduction, the thesis is divided into four chapters and concludes with a final summary. Chapter 2 summarizes the available data and explains the data sources.

Chapter 3 highlights the state of art in attenuation correction for hail-bearing storms and introduces an algorithm capable of estimating attenuation in multi-cellular events. Necessary post-processing of radar data and noise reduction methods are discussed. Finally, the algorithm is evaluated on 16 events from 2013 to 2018 and checked for consistency between four overlapping C-band radars.

In chapter 4 the adjustments of S-band hail size dscrimination algorithm (HSDA) for usage at C band and further modifications are discussed. T-matrix scattering simulations are used to adjust parameters for the fuzzy-logic based HSDA. Further experiments to improve the HSDA utilizing unsupervised clustering, neural networks and deep learning techniques are pursued.

Chapter 5 investigates nowcasting capabilities of hail precursors. Two nowcasting schemes are developed to detect hail already during its growth and predicting the final hail size 10 min to 20 min prior to hitting the ground. The introduced nowcasting schemes are tested against a statistically based random prediction and evaluated using hail occurrence reports as ground truth.

Finally, chapter 6 summarizes the thesis and the proposed methods. A conclusion of assessed techniques and gained knowledge closes the thesis.

Chapter 2

Remote Sensing and Other Data Sources

Primary data sources of this study are polarimetric weather radars and ground reports of hail. The following subsections introduce each source.

2.1 Polarimetric C-band radar network

The German national meteorological service (*Deutscher Wetterdienst*, DWD) utilizes polarimetric dual-doppler weather radars, which operate with a wavelength of 5.344 cm (C band). The deployed radars simultaneously transmit and receive in horizontal and vertical polarization (Frech et al., 2017). The 5 min scan schedule includes a volume scan with ten elevations and a so called precipitation scan (Table 2.1). Within this scanning scheme a vertical scan, so called "bird-bath" scan, is included for calibration. Ten fixed elevations are scanned for the volumetric scans with a radial resolution of 1 km. The precipitation scan, however, follows roughly the surrounding orography and has a radial resolution of 0.25 km. Both scans have an azimuthal resolution of 1°. For more details on the scanning strategy see Helmert et al. (2014).

The DWD operates a radar network covering an area of more than 357 000 km^2 with 17 C-band radars. The coverage of this network and each individual radar is shown in Figure 2.1. Many radars overlap partially. There are several groups of four radars which overlap. The group with the largest overlap of four radars is composed of the radars Essen, Flechtdorf, Offenthal and Neuheilenbach. This overlap area can be used to check individual radar corrections for consistency, e.g. comparing attenuation correction results (see chapter 3, section 3.4).

2.1.1 Scattering theory

Particles, like hydrometeors, scatter the incident electromagnetic wave $\vec{E}_i$, and the different scattering between horizontal and vertical polarization allows the retrieval of polarimetric variables. The scattered electromagnetic wave $\vec{E}_s$ is calculated using

TABLE 2.1: Specification of DWD precipitation and volumetric scans.

type of scan	Elevation (°)	bin width (m)	number of range bins	maximum slant range (km)
precipitation	terrain following	250	600	150
volumetric 0	5.5	1000	180	180
volumetric 1	4.5	1000	180	180
volumetric 2	3.5	1000	180	180
volumetric 3	2.5	1000	180	180
volumetric 4	1.5	1000	180	180
volumetric 5	0.5	1000	180	180
volumetric 6	8.0	1000	124	124
volumetric 7	12.0	1000	60	60
volumetric 8	17.0	1000	60	60
volumetric 9	25.0	1000	60	60

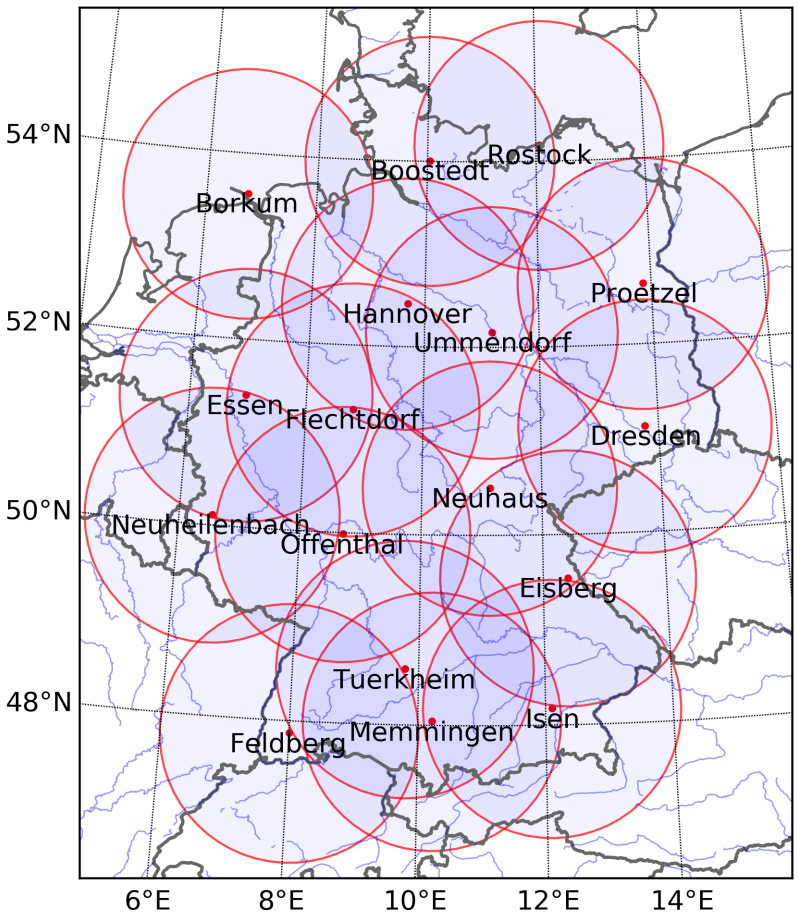

FIGURE 2.1: Stereographic projection of the area covered by the operational radar network of the German national meteorological service (DWD). Each polarimetric C-band radar has a range of 150 km, and their coverage is shown as red circles with a light-blue filling. The location of the radar site is denoted by a red dot and its station name underneath. Blue lines show rivers, while gray lines depict borders and coasts.

the complex scattering matrix $\bar{\bar{S}}$, which contains both magnitude and phase information (Zhang, 2016)

$$\vec{E}_s = \frac{e^{-jkr}}{r}\bar{\bar{S}}\vec{E}_i \,, \tag{2.1}$$

where r is the distance to the scattering particle, k the wavenumber of the background medium, and j the complex solution to the equation $j = \sqrt{-1}$ (Zhang, 2016). The incident and scattered wave consists of horizontal (H) and vertical (V) polarized components when polarimetric radars are used. Following Zhang (2016), equation 2.1 extends to

$$\begin{bmatrix} E_{s,H} \\ E_{s,V} \end{bmatrix} = \frac{e^{-jkr}}{r} \begin{bmatrix} S_{HH} & S_{HV} \\ S_{VH} & S_{VV} \end{bmatrix} \begin{bmatrix} E_{i,H} \\ E_{i,V} \end{bmatrix} \,, \tag{2.2}$$

with the co-polar (S_{HH} and S_{VV}) and the cross-polar (S_{HV} and S_{VH}) scattering amplitudes. The subscripts indicate which channel (H for horizontal and V for vertical polarization) transmits (first subscript) and which receives (second subscript).

Particles in the atmosphere typically have various sizes and tumble. Ensemble averages of scattering amplitudes over "all particles contributing to the signal" (Rinehart, 2004) are calculated by integrating the particle size distribution $N(D)$ over all diameters D (Zhang, 2016)

$$\langle \cdots \rangle = \int \cdots N(D)\, dD \,. \tag{2.3}$$

The mean differential scattering cross sections and the correlation function can be calculated respecting particle size distributions and orientations (Jung et al., 2010; Ryzhkov et al., 2010; Zhang, 2016)

$$\left\langle |S_{HH}|^2 \right\rangle = \int \left(M_{AA} |s_a|^2 + M_{BB} |s_b|^2 + 2M_{AB} \mathrm{Re}\left[s_a s_b^*\right] \right) N(D)\, dD \,, \tag{2.4}$$

$$\left\langle |S_{VV}|^2 \right\rangle = \int \left(M_{DD} |s_a|^2 + M_{CC} |s_b|^2 + 2M_{CD} \mathrm{Re}\left[s_a s_b^*\right] \right) N(D)\, dD \,, \tag{2.5}$$

$$\left\langle |S_{HV}|^2 \right\rangle = \left\langle |S_{VH}|^2 \right\rangle = \int M_{BC} |s_a - s_b|^2 N(D)\, dD \,, \tag{2.6}$$

$$\langle S_{HH}^* S_{VV} \rangle = \int \left(M_{AB} |s_a|^2 + M_{CC} |s_b|^2 + M_{AC} \left[s_a^* s_b\right] + M_{BD} \left[s_a s_b^*\right] \right) N(D)\, dD \,, \tag{2.7}$$

where s_a (and s_b respectively) denote the complex scattering amplitudes of an individual spheroidal particle along their minor (major) axes (Trömel et al., 2013) and M_i are angular moments (for $i = AA, BB, CC, DD, AB, CD, BC, AD, AC, BD$ respectively). The asterisk is the conjugate complex operator and $\mathrm{Re}(x)$ is the real part of a complex variable x. For simplicity, tumbling is limited to particle canting in the polarization plane and the particle orientation across all particles involved is assumed to be Gaussian distributed with a zero mean canting angle (Ryzhkov et al., 2010;

Zhang, 2016). Then the angular moments are

$$M_1 = M_{AA} = M_{CC} = M_{AC} = \frac{1}{8}\left(3 + 4e^{-2{\sigma_\psi}^2} + e^{-8{\sigma_\psi}^2}\right) , \tag{2.8}$$

$$M_2 = M_{BB} = M_{DD} = M_{BD} = \frac{1}{8}\left(3 - 4e^{-2{\sigma_\psi}^2} + e^{-8{\sigma_\psi}^2}\right) , \tag{2.9}$$

$$M_3 = M_{AB} = M_{CD} = M_{AD} = M_{BC} = \frac{1}{8}\left(1 - e^{-8{\sigma_\psi}^2}\right) , \tag{2.10}$$

where σ_ψ is the standard deviation of the canting angle (ψ) distribution. Equations 2.4, 2.5, 2.6 and 2.7 then simplify to

$$\left\langle |S_{HH}|^2 \right\rangle \approx \int \left(M_1 |s_a|^2 + M_2 |s_b|^2 + 2M_3 \mathrm{Re}\left[s_a s_b^*\right]\right) N(D)\, dD , \tag{2.11}$$

$$\left\langle |S_{VV}|^2 \right\rangle \approx \int \left(M_2 |s_a|^2 + M_1 |s_b|^2 + 2M_3 \mathrm{Re}\left[s_a s_b^*\right]\right) N(D)\, dD , \tag{2.12}$$

$$\left\langle |S_{HV}|^2 \right\rangle = \left\langle |S_{VH}|^2 \right\rangle \approx \int M_3 |s_a - s_b|^2 N(D)\, dD , \tag{2.13}$$

$$\langle S_{HH}^* S_{VV} \rangle \approx \int \left(M_3 \left[|s_a|^2 + |s_b|^2\right] + M_1 \left[s_a^* s_b\right] + M_2 \left[s_a s_b^*\right]\right) N(D)\, dD . \tag{2.14}$$

Typically, a measured radar volume consists of multiple particles. Therefore, propagation of the electromagnetic wave needs to be considered, too. The coherent electromagnetic wave after propagating to a position x can be described using the transmission matrix $\bar{\bar{T}}$ (Zhang, 2016)

$$\begin{bmatrix} E_h(x) \\ E_v(x) \end{bmatrix} = \underbrace{\begin{bmatrix} e^{-j\int_0^x K_h d\ell} & 0 \\ 0 & e^{-j\int_0^x K_v d\ell} \end{bmatrix}}_{\bar{\bar{T}}} \begin{bmatrix} E_h(0) \\ E_v(0) \end{bmatrix} , \tag{2.15}$$

where the effective propagation constants K_h and K_v are

$$K_h = k + \frac{2\pi}{k}\left\langle S_{HH}^{(0)} \right\rangle , \tag{2.16}$$

$$K_v = k + \frac{2\pi}{k}\left\langle S_{VV}^{(0)} \right\rangle , \tag{2.17}$$

with $S_{HH}^{(0)}$ and $S_{VV}^{(0)}$ being the forward-scattering amplitudes in horizontal and vertical polarization, respectively. Note that propagation depolarization effects are neglected. The received electromagnetic wave $\vec{E}_r$ can be expressed by the transmitted field $\vec{E}_t$ when the propagation is taken into account (Zhang, 2016)

$$\vec{E}_r = \tfrac{1}{r}\bar{\bar{T}}\bar{\bar{S}}\vec{E}_i , \tag{2.18}$$

$$\vec{E}_i = \bar{\bar{T}}\vec{E}_t , \tag{2.19}$$

so that

$$\begin{bmatrix} E_{r,H} \\ E_{r,V} \end{bmatrix} = \frac{1}{r} \underbrace{\begin{bmatrix} S_{HH} e^{-2j\int_0^r K_h d\ell} & S_{HV} e^{-j\int_0^r (K_h+K_v) d\ell} \\ S_{VH} e^{-j\int_0^r (K_h+K_v) d\ell} & S_{VV} e^{-2j\int_0^r K_v d\ell} \end{bmatrix}}_{\bar{\bar{S}}'} \begin{bmatrix} E_{t,H} \\ E_{t,V} \end{bmatrix} . \tag{2.20}$$

The matrix $\bar{\bar{S}}'$ includes propagation and scattering effects, and their co-polar components (the components on the main diagonal) can be used to calculate "propagation-included radar variables" (Zhang, 2016), i.e. attenuation corrected polarimetric moments.

2.1.2 Polarimetric variables

Polarimetric radars not only allow for measuring reflectivity factors, but due to measuring horizontal and vertical polarization in two channels separately, multiple polarimetric variables can be obtained. Here briefly the most important polarimetric variables used in this study are defined and explained. For a more thorough and complete explanation on their information content the reader is encouraged to read well-written books on this topic, such as Bringi and Chandrasekar (2001), Rinehart (2004), Doviak and Zrnic (2006), Zhang (2016), or Ryzhkov and Zrnic (2019).

Comparing the amplitude or intensity of both channels yields probably the most simple and maybe most used polarimetric variable. As raindrops with larger sizes become oblate, the difference between the returned signal strength of the two channels will increase, which is quantified by differential reflectivity Z_{DR} (Rinehart, 2004; Doviak and Zrnic, 2006; Zhang, 2016)

$$Z_{DR} = Z_h - Z_v = 10 \log_{10} \left(\frac{z_h}{z_v} \right) , \tag{2.21}$$

$$z_h = \frac{4\lambda^4}{\pi^4 |K_w|^2} \left\langle |S_{HH}|^2 \right\rangle , \tag{2.22}$$

$$z_v = \frac{4\lambda^4}{\pi^4 |K_w|^2} \left\langle |S_{VV}|^2 \right\rangle , \tag{2.23}$$

where Z_h and Z_v are the horizontal, respectively vertical, reflectivity factors in logarithmic scale and z_h and z_v are the horizontal respectively vertical reflectivity factors in linear scale. λ is the wavelength of the radar, $K_w = \frac{\epsilon_w/\epsilon_0 - 1}{\epsilon_w/\epsilon_0 + 2}$ is the dielectric constant factor for water, ϵ_w the complex dielectric constant of water and ϵ_0 the dielectric constant in free space (Zhang, 2016). Naturally, the dielectric constant for ice is different and $|K_w|^2$ is about 4 times smaller for ice particles than for pure liquid water particles (Doviak and Zrnic, 2006). The unit of z_h and z_v is $\mathrm{mm}^6/\mathrm{m}^3$ and for their logarithmic expressions, Z_h and Z_v, the unit is dBZ. Therefore, the unit of Z_{DR} is expressed in dB. Reflectivity factors can be compared between different radars, as these factors (see equations 2.21 - 2.23) are normalized by radar wavelength λ and water dielectric constant factor K_w and are only depend on hydrometeor physics

(Zhang, 2016). Values for Z_{DR} around 0 dB indicate spherical or tumbling, i.e. randomly orientated, particles e.g. dry hail, while positive values indicate oblate particles like large raindrops (Ryzhkov et al., 2013a). Negative values are sometimes observed, too, which can be caused by vertical orientated particles such as ice needles in an electric field, conical graupel or by resonance effects (Rinehart, 2004; Evaristo et al., 2013; Kumjian, 2013).

In severe, hail-bearing storms the returned signal can be strongly attenuated (Ryzhkov et al., 2013b). In contrast to strongly affected radar variables like Z_h and Z_{DR}, phase-derived variables are not constrained by attenuation, as long as no total signal extinction occurs. By measuring the phase difference between the two receiving channels, information about the particles in the observed volume can be obtained. The radar typically measures the total differential phase Φ_{DP}, i.e. the difference between the phase of the two received polarizations, horizontal and vertical. Φ_{DP} consists of the backscatter differential phase δ and the propagation differential phase ϕ_{DP} (Wang and Chandrasekar, 2009; Trömel et al., 2013; Zhang, 2016; Ryzhkov and Zrnic, 2019)

$$\Phi_{DP} = \delta + \phi_{DP} \,, \tag{2.24}$$

$$\delta = \arg\left(\langle S_{HH}^{*} S_{VV} \rangle\right) \,. \tag{2.25}$$

The propagation differential phase can be obtained by integrating the specific differential phase over the propagation path r (Zhang, 2016)

$$\phi_{DP} = 2 \int_0^r K_{DP}\left(\ell\right) d\ell \,. \tag{2.26}$$

K_{DP} is *specific* as in *per length unit*. Therefore, the unit of K_{DP} is $^\circ\,\mathrm{km}^{-1}$. Zhang (2016) defines K_{DP} as "the real part of the propagation constant difference", which is

$$K_{DP} = \frac{180}{\pi} \mathrm{Re}\left[K_h - K_v\right] \tag{2.27}$$

$$\approx \frac{180}{\pi} \int \mathrm{Re}\left[s_a^{(0)} - s_b^{(0)}\right] N\left(D\right) dD \frac{1}{2} \left(1 + e^{-2{\sigma_\psi}^2}\right) e^{-2{\sigma_\psi}^2} \,, \tag{2.28}$$

where $s_a^{(0)}$ (and $s_b^{(0)}$ respectively) is the forward-scattering amplitude along the minor (major) axis of an individual spheroidal particle. For radar operations, however, this is unpractical as forward-scattering amplitudes are not available for monostatic weather radars. According to Rinehart (2004) the specific differential phase K_{DP} between the radial ranges r_1 and r_2 can be calculated using

$$K_{DP} = \frac{\Phi_{DP}\left(r_2\right) - \Phi_{DP}\left(r_1\right)}{2\left(r_2 - r_1\right)} \,. \tag{2.29}$$

Note that equation 2.29 is only valid when backscatter differential phase δ is neglectable, so that $\Phi_{DP} \approx \phi_{DP}$. However, such scattering induced phase shifts are present in e.g. hail and melting snow (Trömel et al., 2013; Zhang, 2016). This needs

to be mitigated as well, before calculating K_{DP}. The hydrometeor type, or more specifically their refractive index, the temperature and the transmitted wavelength additionally affects the phase of each channel. By using a range-derivate of the phase difference, issues like attenuation, beam blockage or calibration errors can be ignored. Desired information like orientation, shape and size of the observed particles impact K_{DP} (Rinehart, 2004). The estimation of K_{DP} usually requires substantial signal post-processing, because Φ_{DP} can be very noisy (Kumjian et al., 2019).

Despite the aforementioned differences in signal strength and phase shifts between the two channels, weather echoes usually are quite coherent (Doviak and Zrnic, 2006). Non-meteorological echoes usually are not (Ryzhkov et al., 2005b). The correlation of the signal power between the horizontal and vertical channel can be expressed by the co-polar cross-correlation coefficient ρ_{hv}. Rinehart (2004) defines

$$\rho_{hv} = \frac{|\langle S_{VV} S_{HH}^{*} \rangle|}{\sqrt{\left\langle |S_{HH}|^2 \right\rangle} \sqrt{\left\langle |S_{VV}|^2 \right\rangle}} \,. \tag{2.30}$$

Values for ρ_{hv} can range from 1, for spherical targets, to 0. Meteorological echoes have values around 0.90, e.g. 0.97 for rain (Park et al., 2009), except for hail, for which ρ_{hv} can drop as low as 0.80 at S band (Ryzhkov et al., 2013b). Non-meteorological echoes, like ground clutter, typically have much lower values.

Depolarization, i.e. the loss of polarization of an emitted electromagnetic wave due to propagation or scattering, can be expressed by quantities such as the linear depolarization ratio (LDR). By transmitting in horizontal polarization, but retrieving in both channels, the ratio of the received power of the two channels is LDR (Rinehart, 2004; Zhang, 2016)

$$\mathrm{LDR} = 10 \log_{10} \left(\frac{\left\langle |S_{HV}|^2 \right\rangle}{\left\langle |S_{HH}|^2 \right\rangle} \right) \,. \tag{2.31}$$

In theory, LDR can reach values of 0 dB for one-dimensional targets, i.e. no depolarization, and can go towards $-\infty$ dB for spherical targets (Rinehart, 2004). LDR can be used to distinguish liquid and frozen particles (Rinehart, 2004), but depends strongly on the particles' orientation (Ryzhkov et al., 2017). However, LDR cannot be recorded by the DWD C-band radars without changing the scanning schedule and switching off vertical transmission.

Most operational weather radars are operated in a simultaneous transmission / reception mode. This mode enables to measure differential reflectivity Z_{DR}, cross-correlation coefficient ρ_{hv} and differential phase Φ_{DP}, but not to measure intrinsic circular depolarization ratio (CDR). However, methods to estimate CDR have been proposed (Matrosov, 2004; Ryzhkov et al., 2014, 2017), which can calculate a depolarization ratio (DR) estimate from complex voltages (Ryzhkov et al., 2014) or from

polarimetric variables (Ryzhkov et al., 2017). Complex voltages usually are not available for researchers for operational weather radars, as they are only stored in the signal processor, but Z_{DR}, ρ_{hv}, Φ_{DP} usually are. Linear depolarization value LDR is only available when vertical transmission can be turned off e.g. during an LDR sweep (Ryzhkov et al., 2014, 2017).

According to Ryzhkov et al. (2017) the circular depolarization ratio in linear scale C_{dr} can be expressed with

$$C_{dr} = \frac{1 + (Z_{dr})^{-1} - 2\rho_{hv}(Z_{dr})^{-1/2}\cos(\Phi_{DP}) + 4L_{dr}}{1 + (Z_{dr})^{-1} - 2\rho_{hv}(Z_{dr})^{-1/2}\cos(\Phi_{DP})} , \tag{2.32}$$

where

$$Z_{DR} = 10\log_{10}(Z_{dr}) , \tag{2.33}$$

$$\mathrm{LDR} = 10\log_{10}(L_{dr}) \text{ and} \tag{2.34}$$

$$\mathrm{CDR} = 10\log_{10}(C_{dr}) . \tag{2.35}$$

Even a small increase in Φ_{DP} can affect C_{dr} strongly. Thus, propagation effects as in heavy rain, reduce the usability of C_{dr}. Since hail is often accompanied by rain, this is an obstacle if C_{dr} is considered to be used for hail detection.

When $\Phi_{DP}^{(t)}$, the system differential phase upon transmission, is $\pm 90°$, depolarization ratio (DR) can be used as a proxy for CDR. In linear scale DR is defined by (Ryzhkov et al., 2017)

$$D_r = \frac{1 + (Z_{dr})^{-1} - 2\rho_{hv}(Z_{dr})^{-1/2} + 4L_{dr}\cos^2(\Phi_{DP}/2)}{1 + (Z_{dr})^{-1} - 2\rho_{hv}(Z_{dr})^{-1/2} + 4L_{dr}\sin^2(\Phi_{DP}/2)} , \tag{2.36}$$

$$\mathrm{DR} = 10\log_{10}(D_r) . \tag{2.37}$$

For $\Phi_{DP} = 0°$, i.e. no polarization-dependent propagation effects, C_{dr} and D_r are equal. Even for $\Phi_{DP}^{(t)} \neq \pm 90°$ and moderate Φ_{DP}, e.g. $10\,°\,\mathrm{km}^{-1}$ to $20\,°\,\mathrm{km}^{-1}$, the depolarization ratio was proven to be useful at S band (Ryzhkov et al., 2017). Like CDR, DR can range from $-\infty$ dB to 0 dB, where the former would be a spherical and the latter a very irregularly shaped particle, e.g. spiky hail stones (Rinehart, 2004).

Particles in the radar volume weaken the returned signal by absorption and scattering of the electromagnetic wave. The amount of signal weakening per radial range is called specific attenuation A_h. In this thesis, A_h always denotes the specific attenuation in the horizontal polarization. Integrating the scattering in a coherent

electric field yields (Zhang, 2016)

$$A_h = 10\log_{10}\left(e^{2\lambda \mathrm{Im}\left(\left\langle S_{HH}^{(0)}\right\rangle\right)}\right) = 20\lambda\log_{10}(e)\,\mathrm{Im}\left(\langle S_{HH,0}\rangle\right) \tag{2.38}$$

$$\approx 20\lambda\log_{10}(e)\int\left[\mathrm{Im}\left(s_a^{(0)}\right) - \frac{1}{4}\left(1-e^{-4\sigma_\psi{}^2}\right)\mathrm{Im}\left(s_b^{(0)} - s_a^{(0)}\right)\right]N(D)\,dD\,, \tag{2.39}$$

where $\mathrm{Im}(x)$ is the imaginary part of a complex variable x. A_h can range from $0\,\mathrm{dB\,km^{-1}}$, i.e. no attenuation, to $+\infty\,\mathrm{dB\,km^{-1}}$. However, total signal extinction can occur even with small A_h, depending on the intrinsic signal strength and the amount of attenuating particles.

Specific attenuation A_h cannot be directly measured by the radars used, because monostatic weather radar designs can only receive backward-scattered signals. Forward-scattering is not observed and therefore A_h is not measured. Nevertheless, other means of estimating the specific attenuation exist. Bringi et al. (1990) suggest a linear attenuation correction, where the decrease in reflectivity through attenuation ΔZ_h is related to the propagation phase ϕ_{DP} along the propagation path between 0 and r

$$\Delta Z_h = \alpha\cdot\phi_{DP} = \alpha\cdot 2\int_0^r K_{DP}(\ell)\,d\ell\,, \tag{2.40}$$

where α is an attenuation coefficient, ranging from values close to $0\,\mathrm{dB/^\circ}$ to $1\,\mathrm{dB/^\circ}$, with a median value of $0.08\,\mathrm{dB/^\circ}$ for rain at C band, and dependent on temperature (Bringi et al., 2001; Ryzhkov et al., 2013b). If the two-way path-integrated attenuation ($\mathrm{PIA} = 2\int_0^r A_h(\ell)\,d\ell$, Zhang, 2016) is equal to ΔZ_h, a relation between specific attenuation A_h and K_{DP} is obtained

$$2\int_0^r A_h(\ell)\,d\ell = \mathrm{PIA} = \alpha\cdot 2\int_0^r K_{DP}(\ell)\,d\ell\,, \tag{2.41}$$

$$\Rightarrow \qquad A_h = \alpha\cdot K_{DP}\,, \tag{2.42}$$

assuming α is constant. The correlation (equation 2.42) is no surprise as attenuation, as well as propagation phase, are an effect of forward-scattering (Zhang, 2016). A more sophisticated way to estimate A_h and α is explained in chapter 3.

2.2 Hail Ground Reports

The European Severe Weather Database (ESWD, `https://www.eswd.eu`) provides reports of hail larger than 2 cm by citizen scientists and trained storm spotters (Dotzek et al., 2009). The reports include geographic location, date and time of occurrence. Also, a time range for each hail occurrence is provided to take into account possible delay in reporting. Additional, optional entries in the report can be maximum hail diameter, damage reports and weight of hail, among others. In cases of large accumulations of small hail, a thickness of the hail layer on the ground is added as well. Several quality levels allow for filtering of the reports. These levels range from

"as received", i.e. no checks done, over "plausibility checked", to "report confirmed by reliable source" and "event fully verified", the highest level (Dotzek et al., 2009). In this study, only reports with "plausibility checked" or higher quality are used. These hail reports are considered as point observations in space and time. I.e., hail occurrence can not be excluded, when no hail has been reported.

More than 2000 reports of hail diameters $\geq$ 2 cm have been issued throughout Europe per year since 2012. 7 % of these contain maximum hail diameters of at least 5 cm. 14.1 cm was the largest reported hail stone in Germany and the second-largest in Europe. The largest hail with a diameter of 15 cm occurred in Sânandrei in Romania (Púčik et al., 2019).

2.3 Atmospheric Soundings

Radio soundings provide *in-situ* measured vertical profiles of temperature, humidity, pressure and wind. Soundings are launched several times a day from measurement sites and are usually operated by national meteorological services. In Germany, soundings are launched up to four times a day at 14 stations operated by the DWD[1]. The University of Wyoming Department of Atmospheric Sciences kindly provide a service to retrieve sounding data from stations all over the world on their website (http://weather.uwyo.edu/upperair/sounding.html). Here soundings in Germany are used to determine a spatially interpolated height of the 0 °C isotherm.

[1]Source: https://www.dwd.de/DE/service/lexikon/Functions/glossar.html?nn=103346&lv2=102134&lv3=102172, last accessed on 11.02.2020 11:26 UTC

Chapter 3

Attenuation Correction in Hail-Bearing Storms at C Band

Hail may cause anomalously high attenuation, impedes accurate nowcasting and warnings, and hampers quantitative precipitation estimation (Trömel et al., 2014). Compared to S band, attenuation at C band can be quite severe and requires correction (Ryzhkov et al., 2013a).

This chapter reviews existing methodologies for correcting anomalously high attenuation, including their evaluation using four overlapping C-band radars. To apply the theoretical methods to actual weather radar measurements, algorithms to improve signal quality and noise reduction are introduced. Afterwards, scores for assessing the usability of the attenuation correction are explained and the evaluation is conducted. Lastly, a summary of the chapter is given, which concludes and closes this chapter.

3.1 State of the Art

Compared to a simple attenuation correction (see e.g. equation 2.42), which requires a constant attenuation coefficient α, the so called ZPHI method, introduced by Testud et al. (2000), allows attenuation correction in stratiform and convective precipitation. Furthermore, the ZPHI method can estimate contamination of increased backscatter differential phase δ, which may affect Φ_{DP} at C and X band (Testud et al., 2000; Trömel et al., 2013). The ZPHI method comprises in its application for ground-based weather radars the total differential phase shift Φ_{DP} along a considered range interval as an external constraint to estimate specific attenuation for each radar bin.

Ryzhkov et al. (2013b) developed an algorithm, based on the ZPHI method, to correct reflectivity factors for anomalous attenuation caused by hail at S band. Ryzhkov et al. (2013b) separate sections of precipitation along each azimuthal ray into segments of rain, hail and rain behind hail. Segments with hail are called hot spots. Different parameters are applied in hot spots than in segments without hail. E.g. the attenuation coefficient α is expected to be higher in hail than in rain.

Gu et al. (2011) introduced a modified hot spot approach, which allows for determining an appropriate α iteratively, using the radials outside the hot spot as a

constraint. An optimal α is achieved when the integration of the attenuation profile of radials outside of the hot spot equals the estimation of the simple attenuation correction (see e.g. equation 2.42).

With the mentioned segmentation, attenuation, especially in the shadow of the hail-core, can be corrected for events with small hail as well as for events with large hail. Also, the estimated attenuation can indicate whether the hail assumption was correct or not. E.g. there is probably no hail when the attenuation in the assumed hail-core is not significantly higher than it would be in rain.

3.2 Theory

A radial profile of specific attenuation A_h can be obtained by the ZPHI method as expression of the attenuated reflectivity factor in linear units z_a at each range bin r (Testud et al., 2000; Ryzhkov et al., 2013b):

$$A_h(r) = \frac{[z_a(r)]^b}{I(r_0, r_m) + \left[10^{0.1b\alpha\Delta\Phi_{DP}(r_0,r_m)} - 1\right] I(r, r_m)} \cdot \left[10^{0.1b\alpha\Delta\Phi_{DP}(r_0,r_m)} - 1\right] , \quad (3.1)$$

where

$$I(r, r_m) = 0.46b \int_r^{r_m} [z_a(s)]^b \, ds \quad \text{and} \quad (3.2)$$

$$\Delta\Phi_{DP}(r_0, r_m) = \Phi_{DP}(r_m) - \Phi_{DP}(r_0) \ . \quad (3.3)$$

The parameter b is taken from the empirical relation between specific attenuation A_h and reflectivity factor Z_h ($A_h = aZ_h^b$, e.g. see Table 1 in Ryzhkov et al., 2013b).

To apply attenuation correction for hail, each radar sweep is scanned for hot spots. An easy approach to do this can be a reflectivity factor threshold (e.g. 45 dBZ). For each hot spot, the affected rays are segmented using three range intervals with the following assumptions (compare Ryzhkov et al., 2013b):

- Interval (r_0, r_1) is in front of the hot spot and therefore without hail.
- Interval (r_1, r_2) is the hot spot and possibly contains hail.
- Interval (r_2, r_m) is behind the hot spot and without hail again, but possibly highly attenuated.

The value for attenuation coefficient α differs for hail and rain and therefore differs between the segments, too. This has to be considered in the calculation of specific attenuation, which means equation 3.1 needs modification. A first, simple step to regard these differences is to split up α into a "background" α_0 and a $\Delta\alpha$ (Gu et al., 2011), so that

$$\alpha = \alpha_0 + \Delta\alpha \ . \quad (3.4)$$

α_0 is set to a climatological value (0.06 dB/° (Gu et al., 2011)), so that it is valid for rain-only range bins, while $\Delta\alpha$ is adjusted to fit to the dominant hydrometeor type,

e.g. hail. Modifying equation 3.1 by taking equation 3.4 into account yields

$$A_h(r, \Delta\alpha) = \frac{[z_a(r)]^b}{I(r_0, r_m) + [10^{0.1bC} - 1]\, I(r, r_m)} \cdot \left[10^{0.1bC} - 1\right] , \tag{3.5}$$

where

$$C = \alpha_0 \Delta\Phi_{DP}(r_0, r_m) + \Delta\alpha \Delta\Phi_{DP}(r_1, r_2) . \tag{3.6}$$

Following Gu et al. (2011), $\Delta\alpha$ is determined by an iterative process. The values at the range gates in the intervals (r_0, r_1) and (r_2, r_m), i.e. "outside of hot spots (OHS)", serve as a constraint, so that

$$\int_{OHS} A_h(s, \Delta\alpha)\, ds \stackrel{!}{=} \frac{\alpha}{2} \cdot [\Delta\Phi_{DP}(r_0, r_m) - \Delta\Phi_{DP}(r_1, r_2)] \tag{3.7}$$

is fulfilled (Gu et al., 2011).

Equation 3.7 is iteratively optimized, i.e. applying equation 3.5 with increasing $\Delta\alpha$, until an optimal $\Delta\alpha$ is found. Then, the intrinsic reflectivity factor in decibels Z_h is calculated with

$$Z_h(r) = 10 \log_{10}[z_a(r)] + 2 \int_{r_0}^{r} A_h(s, \Delta\alpha)\, ds . \tag{3.8}$$

3.3 Signal Enhancing and Noise Filtering

Radar data and especially polarimetric radar data requires preprocessing and noise filtering to enable reliable retrievals. Techniques and procedures applied are outlined in this section.

3.3.1 Φ_{DP} unfolding

The value range of differential phase Φ_{DP} is measured from $-180°$ to $180°$. Thus, values measured can be ambiguous if they exceed the dynamic measurement range. To unfold Φ_{DP} the following scheme is used:

$$\Phi_{DP,\text{unfolded}} = \begin{cases} \Phi_{DP} - \Phi_{DP,\text{sys}}, & \text{if } \Phi_{DP} > \Phi_{DP,\text{sys}} - 180°. \\ \Phi_{DP} - \Phi_{DP,\text{sys}} + 360°, & \text{otherwise.} \end{cases} \tag{3.9}$$

The system differential phase $\Phi_{DP,\text{sys}}$ is dependent on the radar and external factors and may change on the time scales of hours to days. Therefore, $\Phi_{DP,\text{sys}}$ has to be determined for each sweep before Φ_{DP} can be unfolded.

One way to estimate $\Phi_{DP,\text{sys}}$ is to observe Φ_{DP} in light rain conditions, thus Φ_{DP} should be $0°$ due to almost spherical scatterers. The median value of all Φ_{DP} measurements are taken, which reach a certain cross-polar correlation coefficient ρ_{hv} threshold. In theory, only the first bins should be taken to keep the contamination of propagation effects on the $\Phi_{DP,\text{sys}}$ estimation low. However, in practice only few

bins fulfill the requirements, especially in convective events. Therefore, no limitation is applied on the position of the bins used here.

For each ray, continuous sections with ρ_{hv} over 0.95 are selected, if they consist of at least 20 range bins. If at least 30 of these sections are found in one sweep, a $\Phi_{DP,\mathrm{sys}}$ is estimated by taking the median of Φ_{DP} in these bins. For some sweeps, these conditions do not hold. A previously estimated $\Phi_{DP,\mathrm{sys}}$ is then used as significant changes in $\Phi_{DP,\mathrm{sys}}$ are not expected to occur within minutes.

3.3.2 Noise filtering in Φ_{DP}

For correcting attenuation, only the increase in total difference phase shift Φ_{DP} in each segment is relevant. However, both noise and backscatter differential phase δ can have a non-negligible impact on Φ_{DP}. Especially in severe hail events resonance effects may cause negative slopes in Φ_{DP}. This can not only reduce the effectiveness of the attenuation correction, but can also hinder the correction completely. Therefore, noise and artifacts like spikes are dismissed and replaced by linearly interpolated values.

Spikes due to noise contamination are detected by calculating the differences in Φ_{DP} between two bins, where the latter bin has the index r, so that

$$\Delta\Phi_{DP}(r) = \Phi_{DP}(r) - \Phi_{DP}(r-1) \ . \tag{3.10}$$

If $\Delta\Phi_{DP} \geq 66°$, the affected bin is replaced by a linearly interpolated value of the surrounding bins. This noise filter is applied iteratively until no so defined spikes are detected or a limit of iterations is exceeded. The threshold of 66° as well as a limit of three iterations maximum has been determined empirically. If the whole ray is too noisy, all range bins are set to 0°.

To further filter for artifacts, like smaller spikes and fluctuations, and possibly δ contamination, a median filter is applied. Unlike e.g. a running-mean, this filter effectively cancels out smaller spikes, without modifying non-spiking data.

$$\Phi_{DP,filtered}(r) = \mathrm{median}\left[\Phi_{DP}(r), \cdots, \Phi_{DP}(r+w_s)\right] \ , \tag{3.11}$$

where w_s is the window size of the filter and is set to 5 range bins.

An example of how these techniques affect Φ_{DP} is shown in Figure 3.1a. The data after the very basic unfolding (light green curve) is still way too noisy to be used for a proper attenuation correction. Without spike filtering (i.e. without applying equation 3.11), there are still problematic spikes visible (blue curve). Although quite some fluctuations remain, applying all mentioned filters allows for a proper attenuation correction using ρ_{hv} (see Figure 3.1b) and hot spot identification in the following section 3.3.3 (see Figure 3.1c).

3.3.3 Hot spot identification

To utilize the attenuation correction described in section 3.2, areas with precipitation and hot spots have to be identified. The conditions are based on criteria described by Gu et al. (2011) and Ryzhkov et al. (2007). A propagation path through precipitation (from here "valid area"), containing all three segments, is identified if the following conditions hold:

1. reflectivity factor $Z_h \geq 10\,\text{dBZ}$ for all range bins
2. cross-polarisation coefficient $\rho_{hv} \geq 0.5$ for all range bins
3. the radial length of the "valid area" in question has to be at least 2 km.

A hot spot (range interval (r_1, r_2)) is identified if the following conditions hold:

1. The hot spot in question has to be inside a valid area.
2. reflectivity factor $Z_h \geq 45\,\text{dBZ}$ for all range bins
3. cross-polarisation coefficient $\rho_{hv} \geq 0.7$ for all range bins
4. the radial length of the hot spot in question has to be at least 2 km
5. differential reflectivity $Z_{DR} \geq 3\,\text{dB}$ in at least one range bin.

Due to strong hail precipitation, ρ_{hv} may drop to quite low values in a single range bin. To avoid dismissing or wrongly limiting sections, a modification to the original method by Gu et al. (2011) is done as follows. If two valid areas and/or hot spots only have one or two range bins between them, they may be eligible for merging. However, if ρ_{hv} is below 0.5, the areas are not merged, as other polarimetric moments like Φ_{DP} might be too noisy. Even beyond this threshold Φ_{DP} might be noise affected and is linearly interpolated to fill this gap if the difference between the last valid range bin and the next valid range exceeds 10°.

Multiple convective cells may appear in the same ray behind each other, the algorithm is then applied for each hot spot consecutively. Specific attenuation A_h is calculated for each hot spot separately. However, calculating the intrinsic reflectivity factor requires taking all hot spots into account, as each hot spot does affect other hot spots behind it. I.e. equation 3.8 is still used, but A_h, respectively $\Delta\alpha$, changes throughout the ray.

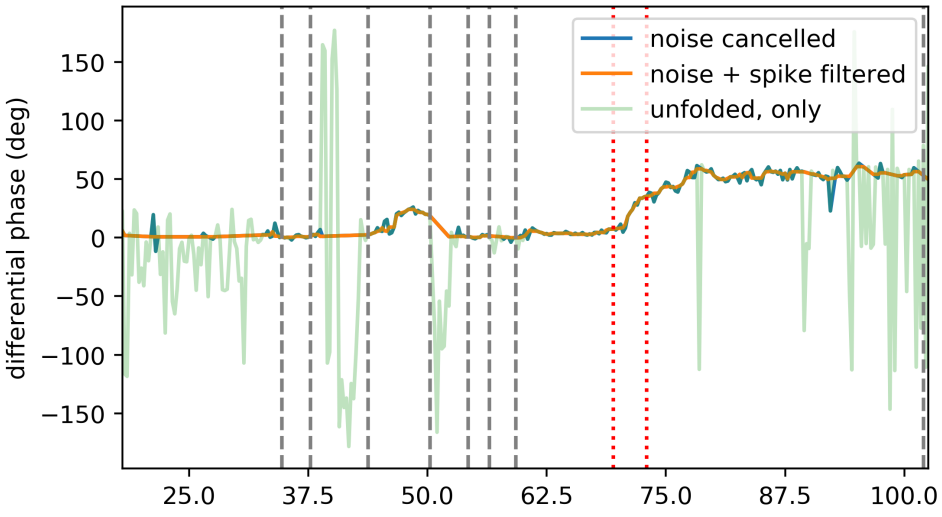

(A) Φ_{DP}

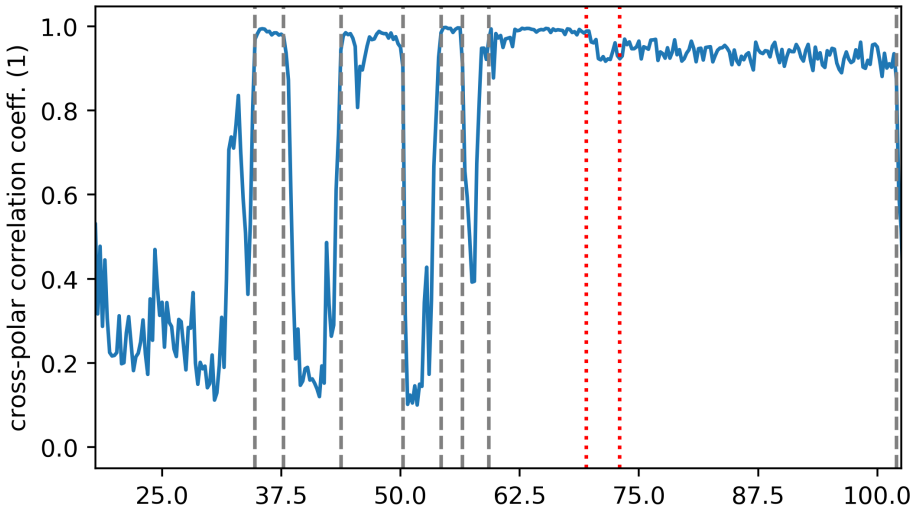

(B) ρ_{hv}

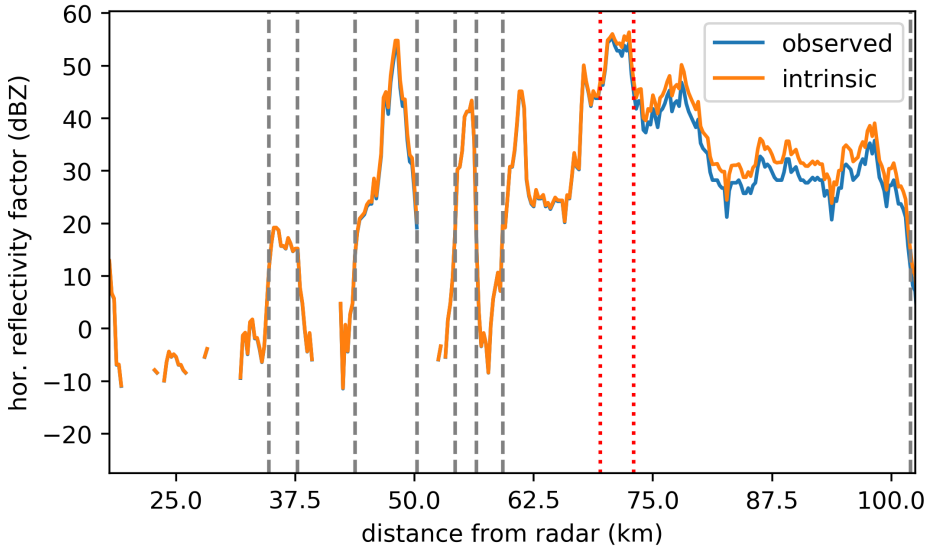

(C) Z_h

FIGURE 3.1: Radial profiles of A) differential phase Φ_{DP} with and without filtering and noise cancellation measures, B) cross-polar correlation coefficient ρ_{hv} and C) hor. reflectivity factor Z_h before and after attenuation correction. The vertical, dashed, gray lines depict sections of precipitation; the vertical, red, dotted lines indicate hot spots. The data was measured on 28.08.2016 13:30 UTC by C-band radar Flechtdorf. The azimuthal angle is 245°.

3.4 Evaluation

Specific attenuation A_h cannot be directly measured by radar. Therefore, it is difficult to obtain a "truth" to compare with. However, radar data of four overlapping C-band radars can be used to test the attenuation correction for consistency. Ideally, if the attenuation was the only factor tampering with the measurement, then all radars should show the same intrinsic reflectivity factor after correcting for attenuation. This is true if the attenuation correction is working perfectly.

3.4.1 Evaluation strategy

All radar data is assigned to a regular Cartesian grid using the so called "Nearest Neighbor" technique. The grid is centered on the overlapping area and has a resolution of 250 m, which is also the radial resolution of the radars. To give an example, Figure 3.2 shows Plane Position Indicator (PPI) plots of four overlapping C-band radars (Essen, Flechtdorf, Neuheilenbach and Offenthal) on the grid, while a hail bearing convective cell is moving through the observed area. As all four radars can observe the same cell from different perspectives, the impact of attenuation is nicely illustrated. Especially in Figure 3.2b a shadow is visible behind stronger reflectivity, which is not represented in the measurements of the other radars. This is a clear indication for hail at C band. A reliable attenuation correction is expected to remove this shadow.

Every radar involved in the comparison can be affected by attenuation or artifacts from e.g. clutter. Ideally not every radar is affected to the same extent or by the same source. Therefore, a mean value of each measurement of all available radars serves as "truth" to compare with.

As reflectivity is used, the mean value $\bar{Z}(i,j)$ is

$$\bar{Z}(i,j) = 10\log_{10}\left[\frac{1}{N_{\text{radars}}}\sum_{n}^{N_{\text{radars}}} 10^{0.1Z_n(i,j)}\right], \tag{3.12}$$

where N_{radars} is the number of radars, Z_n the horizontal reflectivity factor of a specific radar n, and i, j are coordinates of the Cartesian grid. The mean is calculated in linear scale to avoid problems with physical units and to be less affected by clutter and artifacts as stronger signals are more pronounced.

In order to quantify how much the radars differ from each other, the root mean square error (RMSE) is calculated. In this calculation, the mean value $\bar{Z}$ serves as ideal measurement to which all other measurements should converge.

$$\text{RMSE}(i,j) = \sqrt{\frac{1}{N_{\text{radars}}}\sum_{n}^{N_{\text{radars}}}\left[\bar{Z}(i,j) - Z_n(i,j)\right]^2}. \tag{3.13}$$

The RMSE is calculated before and after attenuation correction. The difference of both RMSE values can then show if the attenuation correction improved the signal.

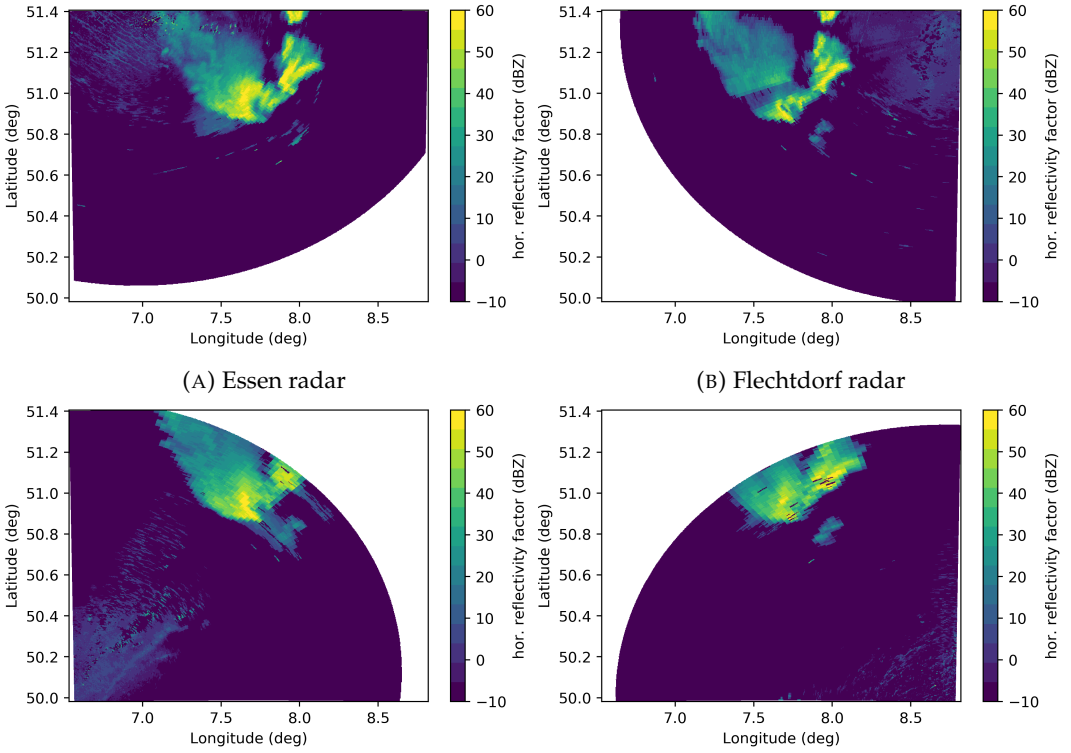

(A) Essen radar

(B) Flechtdorf radar

(C) Neuheilenbach radar

(D) Offenthal radar

FIGURE 3.2: PPI of horizontal reflectivity factor Z_h of four overlapping C-band radars on a Cartesian grid during a hail-bearing storm. All radars observe the same convective cell. Measurements are from 05.07.2015 16:30 UTC. The resolution of the grid is 250 m.

For further evaluation and comparing the array of RMSE values is masked. The masking is done by checking at each grid point if all radars exceed 0 dBZ:

$$\mathrm{RMSE}_{\mathrm{masked}}(i,j) = \begin{cases} \mathrm{RMSE}(i,j), & \text{if } \min\left[Z_n(i,j)\right] > 0\,\mathrm{dBZ},\ \forall n \in N_{\mathrm{radars}} \\ \textit{not a number}, & \text{otherwise}. \end{cases} \tag{3.14}$$

Values which are *not a number* are ignored in further calculations. The masking is done to filter for artifacts, especially on the edge of precipitation areas. E.g. this can be caused by the time lag between radars. But also other artifacts, that usually only appear in single radars, can be filtered.

Figure 3.3 displays mean and $\mathrm{RMSE}_{\mathrm{masked}}$ before and after attenuation correction for the same measurements as in Figure 3.2. The aforementioned shadow is very prominent in the $\mathrm{RMSE}_{\mathrm{masked}}$ of the uncorrected Z_h (Figure 3.3c) with values ≥ 20 dB. After attenuation correction this shadow vanishes, both in mean and $\mathrm{RMSE}_{\mathrm{masked}}$ (see Figure 3.3b and 3.3d), and the error reduces to magnitudes equal to non-attenuated areas.

To analyze the quality of the attenuation correction for all time steps of a single event, the variation of RMSE along time can be tracked with a spatial mean. The spatial mean ξ of radar RMSE (see equation 3.14) is calculated for each time step t,

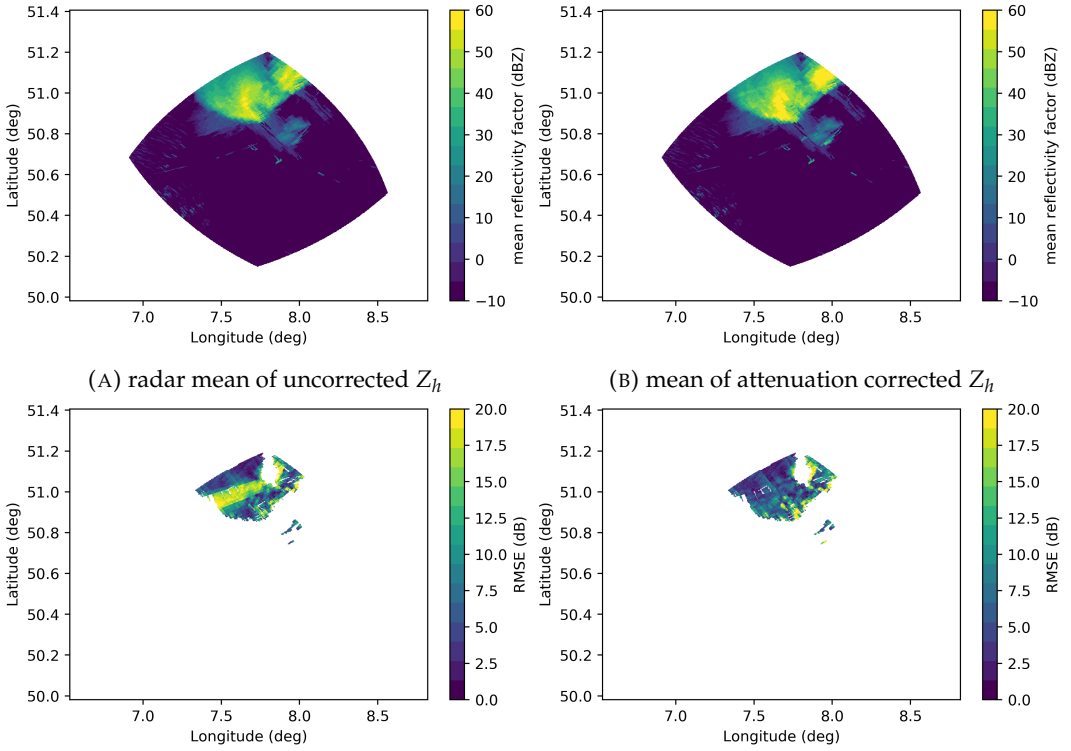

(A) radar mean of uncorrected Z_h

(B) mean of attenuation corrected Z_h

(C) radar $\mathrm{RMSE}_{\mathrm{masked}}$ of uncorrected Z_h

(D) $\mathrm{RMSE}_{\mathrm{masked}}$ of attenuation corrected Z_h

FIGURE 3.3: Mean and RMSE (see equations 3.12, 3.13 and 3.14) of horizontal reflectivity factor Z_h before and after attenuation correction as PPIs. Measurement from 05.07.2015 16:30 UTC.

so that

$$\xi(t) = \frac{1}{M_{\mathrm{area}}} \sum_{i,j}^{M_{\mathrm{area}}} \mathrm{RMSE}_{\mathrm{masked}}(i,j) \ , \tag{3.15}$$

where M_{area} is the number of grid cells in the overlapping area. ξ is calculated before and after attenuation correction.

For the same event as shown in Figure 3.2 and 3.3, $\xi(t)$ is shown as time series in Figure 3.4. As attenuation is not the only source causing different measurements between radars, the values vary throughout the event, even though hail might not be present. However, during presence of hail in the overlapping area (15:45 to 17:05 UTC and 17:20 to 17:50 UTC) the spatial mean of the RMSE is lower for the attenuation corrected data than for the uncorrected one. During other time steps, where no hail bearing cell is inside the overlapping area, the values are mostly equal. Figure 3.5 shows the relative error reduction η_{rel}

$$\eta_{\mathrm{rel}}(t) = \frac{\xi_{\mathrm{uncorrected}}(t) - \xi_{\mathrm{corrected}}(t)}{\xi_{\mathrm{uncorrected}}(t)} \ , \tag{3.16}$$

where $\xi_{\mathrm{uncorrected}}$ and $\xi_{\mathrm{corrected}}$ are the spatial means of radar RMSE (see equation 3.15) before and after attenuation correction.

While enormous error reduction is achieved during aforementioned times, the

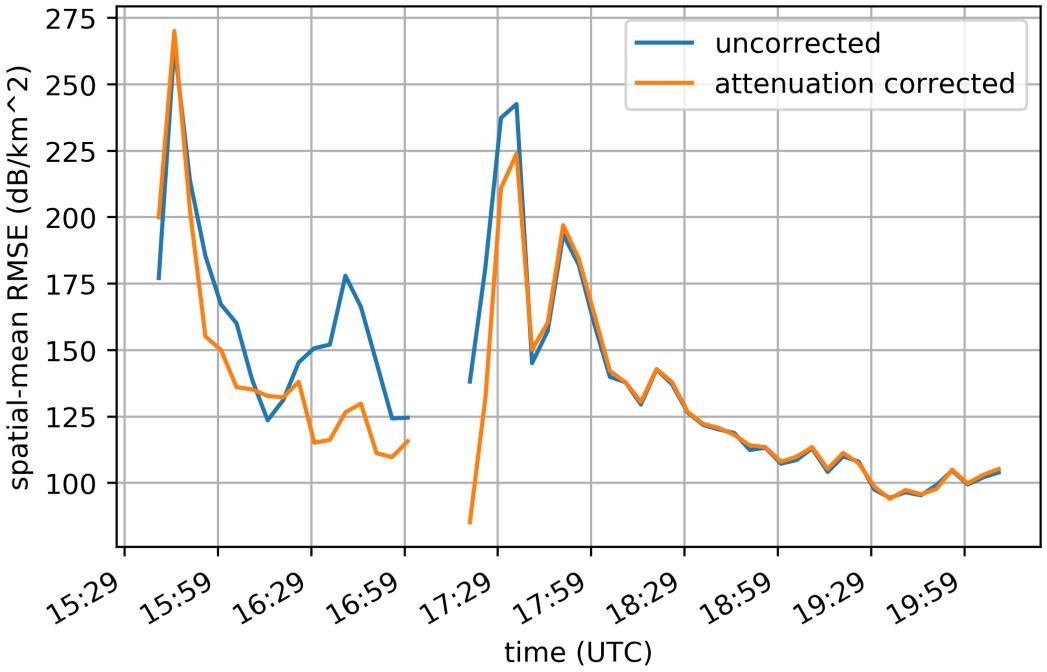

FIGURE 3.4: Time series of the spatial mean of radar RMSE (see equation 3.15) before (blue line) and after attenuation correction (orange line) for a hail bearing event on 05.07.2015. The unit of the spatial mean is dB km^{-2}. The area of each bin in the Cartesian grid is $(250\,\mathrm{m})^2$.

attenuation correction shows a negative impact on the signal later during the event. However, this impact tends to be quite low ($\leq 1\,\%$).

3.4.2 Results

For a more profound evaluation of the attenuation correction 16 severe hail events from 2013 until 2018 taking place in the overlapping area are considered. The mean error reduction per time frame $\bar{\eta}$ and sum of error reduction $\Sigma\eta$

$$\bar{\eta} = \frac{1}{T}\sum_t^T \left[\xi_{\text{uncorrected}}(t) - \xi_{\text{corrected}}(t)\right] \quad \text{and} \tag{3.17}$$

$$\Sigma\eta = \sum_t^T \left[\xi_{\text{uncorrected}}(t)\right] - \sum_t^T \left[\xi_{\text{corrected}}(t)\right] \quad , \tag{3.18}$$

where $\xi_{\text{uncorrected}}$ and $\xi_{\text{corrected}}$ are the spatial means of radar RMSE (see equation 3.15) before and after attenuation correction, are considered in this statistical analysis.

For the majority of these events, positive values are achieved (Table 3.1). I.e. attenuation correction improves individual radar measurements to align more with the measurement of other radars. During some events, e.g. 2014-06-09, the attenuation correction actually worsens the results. However, according magnitudes are small compared to other events with pronounced improvements, e.g. 2013-06-20. On average, i.e. concatenating all time steps of all events together and calculating the statistics, the mean error reduction per frame is around $+0.5\,\mathrm{dB\,min^{-1}\,km^{-2}}$.

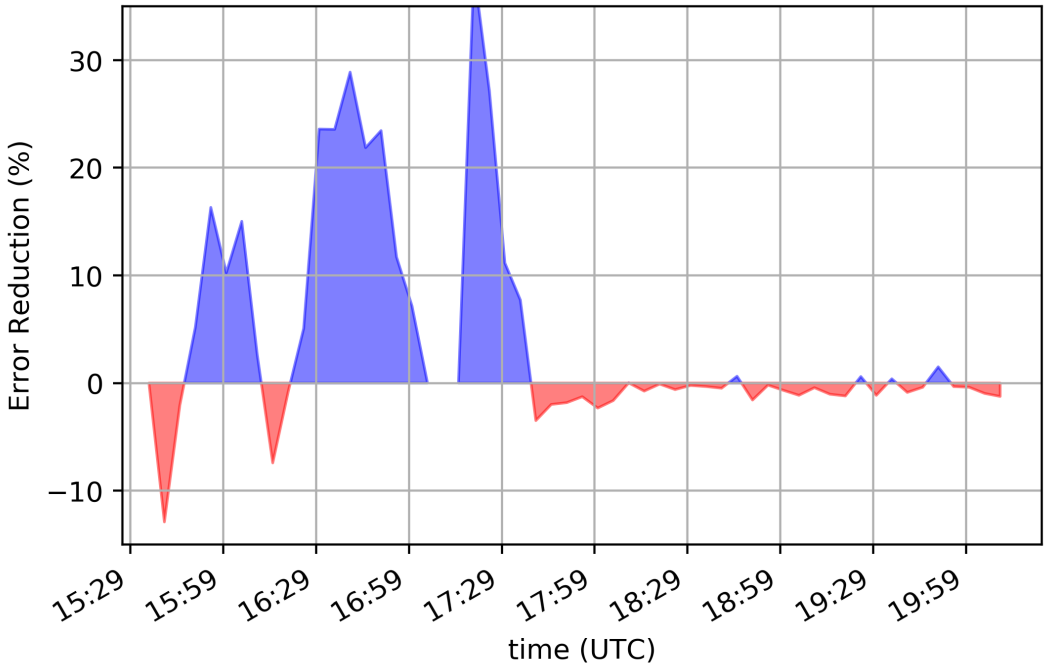

FIGURE 3.5: Time series of reduction of $\xi(t)$ in % due to attenuation correction compared to no correction for a hail bearing event on 05.07.2015. Blue areas mark time steps in which the attenuation correction improved the signal towards the mean of all radars (see equation 3.12), while red areas mark degradation.

Note that the superposition of different factors and the use of logarithmic values may sometimes complicate the interpretation and value of the results. Both $\bar{\eta}$ and $\Sigma\eta$ use RMSE (equation 3.13), which is calculated in dB. Otherwise, attenuation effects would be superimposed by other error sources. E.g. if attenuation reduced the reflectivity from 45 dBZ to 40 dBZ, this would be a reduction in linear scale from 31 623 mm^6/m^3 to 10 000 mm^6/m^3. However, a deviation of the hot spot position due to time delay between radar scans, e.g. from 51 dBZ to 50 dBZ, would be a reduction in linear scale from 125 893 mm^6/m^3 to 100 000 mm^6/m^3 - a whole order of magnitude higher. Therefore, this latter scenario, mispositioned hot spots, would be more emphasized than attenuation effects.

In the following more effects are discussed, which also affect the deviations between radars and therefore impact the statistics. However, they cannot be addressed by an attenuation correction algorithm.

Timing: Not all radars measure the same parts of the overlapping area at the same time. As 5 min pass before a radar scans the same area again, cells might have moved in between. Therefore, for each scan the position of a specific hot spot can be different for each radar. This can lead to deviations between individual radar measurements and the average picture of all four radar measurements. Effects at the edges of precipitating areas are partially mitigated by equation 3.14. However, positions inside the precipitation areas are still affected.

TABLE 3.1: Evaluation statistics for each severe hail event. Four overlapping C-band radars from the DWD radar network were used to do the comparison. A positive error reduction per frame indicates an improvement compared to no correction. The third column shows the total sum of error reduction over all time steps for each events. The last row shows the values for all events being concatenated.

event date (yyyy-mm-dd)	mean error reduction per frame ($dB\,min^{-1}\,km^{-2}$)	sum of error reduction ($dB\,km^{-2}$)
2013-05-16	-0.0698	-8.725
2013-06-20	+1.522	+639.3
2014-06-09	-0.4696	-61.05
2014-06-10	+0.032	+5.928
2014-07-24	+0.3622	+94.18
2015-07-05	+1.548	+402.4
2016-05-27	+0.7786	+186.9
2016-06-05	+0.151	+62.69
2016-06-24	+1.356	+257.6
2016-08-27	-0.0501	-9.017
2016-08-28	+0.3817	+61.07
2017-06-22	+1.494	+403.3
2017-08-01	+1.738	+217.2
2018-04-22	-0.2256	-57.52
2018-05-22	+0.2676	+21.41
2018-05-27	+0.5039	+183.9
all events together	+0.5719	+2512.42

Spatial resolution: A hail bearing cell might be closer to one radar than to another. The Cartesian grid has an equal resolution in zonal and meridional direction. However, radar measurements in polar coordinates, with increasing beam width with increasing distance from the radar, serve as input. As a result the information of far more radar bins are available for a single Cartesian grid closer to the radar than at far distance from the radar. This causes a "checkerboard" pattern on the edge of the radar ranges, which is visible in Figure 3.3a in the North of the overlapping area (e.g. 51.5 °N, 7.8 °E) and again after comparison in the RMSE in Figure 3.3c & 3.3d and therefore affects the evaluation.

Ground clutter: Even though all radars observe a common area, not all radars are affected by the same ground clutter to the same extent. This depends on the location and height of the radar above ground, the elevation of the scan used and the location of the clutter source. E.g. in Figure 3.2b at 51.0 °N, 7.5 °E three black stripes are visible inside the attenuated shadow. Since the pattern remains in the RMSE (Figure 3.3d) it biases the evaluation results despite reliable attenuation correction.

Dynamic clutter: The overlapping area is in the vicinity of a major European airport (Frankfurt international airport). Unlike ground clutter, dynamic and therefore moving clutter, like e.g. from airplanes or other airborne vehicles, is not identified by standard routines (Hubbert et al., 2009; Frech, 2014). When airborne vehicles move close to or into the precipitation area, e.g. a landing airplane, they can strongly affect polarimetric variables, similar to wind turbines (Kong et al., 2013; Frech and

Seltmann, 2017; Seltmann and Böhme, 2017). Particularly for event 2014-06-09 this seems to be the case. Overcorrections were most likely caused by false echoes, which in turn were caused by moving objects at the edge of the overlapping area.

Total signal extinction: During severe storms with giant hail or high concentrations of hail, total signal extinction can occur with no means to restore the data.

Calibration errors: Calibration of e.g. differential reflectivity Z_{DR} is addressed by so called bird-bath scans, i.e. the radar dish is pointing vertically, in each 5 min scan schedule for the DWD radar network (Helmert et al., 2014). By contrast, absolute calibration cannot be done in similar frequency for horizontal reflectivity Z_h. However, the DWD uses nearby micro rain radars (MRR) to estimate the bias between radar and MRR and thereby calibrates Z_h of the radar. Albeit this well elaborated method reduces the residual bias to less than 1 dB, not all radars in the network benefit from this as not all radar sites have a MRR in their vicinity yet (Frech et al., 2017). Therefore, miscalibration between radars might affect the deviations between some radars, too.

3.5 Summary and Conclusion

Techniques for correction of attenuation introduced by Testud et al. (2000), Gu et al. (2011) and Ryzhkov et al. (2013b) were extended for attenuation correction for C band during precipitation of hail. ZPHI and hot spot method, ray segmentation and iterative attenuation parameter adjustment proved to be effective. Combining these techniques, extending for multiple hot spots in single rays and adapting them for hail and C band formed the attenuation correction proposed here.

Application of the attenuation correction requires knowledge about the existence and location of so called hot spots. Criteria for identifying these hot spots, based on thresholds of polarimetric moments and spatial extent, were defined. Furthermore, to enhance the signal and improve the robustness of the algorithm, techniques for Φ_{DP} spike and noise filtering were introduced.

The introduced attenuation correction was tested with four overlapping C-band radars of the DWD radar network. Overall 16 events from 2013 to 2018 were used to evaluate and check for consistency of the attenuation correction. During the majority of the events, the attenuation correction proved to mitigate attenuation effects.

A detailed quantification of the performance, i.e. a comparison of overlapping radar measurements where attenuation is the only difference was impossible. This is due to several other effects, like clutter, unequal bin filling, time gap between radar measurements, ..., which hindered the comparison. Nevertheless, the impact of attenuation could be shown and the effectiveness of the attenuation correction proven.

Chapter 4

A Hail Size Discrimination Algorithm at C Band

In this chapter a modification of the Hail Size Discrimination Algorithm (HSDA) following the principle of Ortega et al. (2016), but adjusted for C band, is attempted. For this purpose, hail is simulated using a T-matrix scattering simulation to obtain ranges of polarimetric variables for different hail size classes.

First, the fuzzy logic, the HSDA and the T-matrix approach for scattering simulations are explained. Second, the HSDA modification approach and particle simulation results are presented. Third, unsupervised learning methods are attempted and discussed. Lastly, the chapter closes with discussions and recommendations for future work.

4.1 Fuzzy Logic and Hail Size Discrimination

4.1.1 Fuzzy logic hydrometeor classification

Fuzzy logic, introduced by Zadeh (1965), is a technique to extend the Boolean logic, so that there is not only "true" (1) or "false" (0) as truth value, but any real number between 0 and 1 (partial truth, Novák et al., 1999).

In meteorology, fuzzy logic schemes are applied to identify dominant hydrometeors in a volume observed by a polarimetric radar (e.g. Dolan and Rutledge, 2009; Park et al., 2009; Thompson et al., 2014, among others). Instead of using strict intervals for certain hydrometeor classes, such as large hail has to have a reflectivity factor strictly between 50 and 70 dBZ, the polarimetric data is fuzzificated. I.e. a membership function, whose input is a polarimetric measurement, yields a value between 0 and 1, which classifies how likely a certain hydrometeor is present.

Dolan and Rutledge (2009) constructed a fuzzy logic hydrometeor identification using one-dimensional beta functions as membership functions for each hydrometeor class and polarimetric variable. They conducted scattering simulations to obtain value ranges of polarimetric variables for liquid and frozen hydrometeors at S and X band. The simulation results are used to determine the parameters of the beta function, i.e. spread width, "midpoint" and slope (see equation 14 in Dolan and Rutledge, 2009). For each hydrometeor a total score is calculated by adding up the

individual, weighted membership function result of each variable. The hydrometeor with the highest score is assumed to be the dominant hydrometeor within the observed volume (Dolan and Rutledge, 2009). Their algorithm, however, excluded hail and mixed-phase categories.

Similar to Dolan and Rutledge (2009), Thompson et al. (2014) use scattering simulations and membership beta functions to obtain a hydrometeor classification for winter precipitation (wet snow, aggregates, plates, dendrites, small ice crystals, rain, and freezing rain) at X, C and S band. Hydrometeor classes above the melting layer are discerned without the need for external temperature information, using polarimetric data only and utilizing a melting layer detection algorithm. This allows for revealing important microphysical features in winter storms, like dendritic and plate crystal growth zones, snowflake aggregation, finescale melting layer fluctuations and melting layer descent (Thompson et al., 2014). Below the melting layer, freezing rain is discerned from the rain class by temperature information from soundings. Although graupel is possible during winter precipitation, a graupel category or hail classes were not included in Thompson et al. (2014).

Park et al. (2009) introduced a fuzzy logic scheme which uses trapezoidal membership functions to discriminate between 10 hydrometeor classes, including a mixture of rain and hail. The range of polarimetric variables, and thus the shape of the trapezoidal membership functions, is based on educated guesses and observations, using "typical values" for each hydrometeor class (Park et al., 2009). Their hydrometeor classes are intended to be suitable for cold and warm seasons. The algorithm features a confidence vector, individual weighting for each pair of hydrometeor class and polarimetric variable, reflectivity-dependent membership functions, consideration of melting layer height for easier separation between liquid and frozen particles, and a vertical continuity check. The confidence vector uses a Gaussian function to estimate the effects of nonuniform beam filling, attenuation, statistical error, partial beam blockage and noise on the classification.

The membership functions used in the following are trapezoidal and are defined by four values (x_1, x_2, x_3, x_4, see Figure 4.1) only, and do not require complex distributions for determining probabilities. Between x_1 and x_2 the probability increases from 0 to 1, is 1 between x_2 and x_3 and declines from 1 to 0 between x_3 and x_4. This simple function keeps the computational effort low and the algorithm easy to comprehend.

For each hydrometeor class i the probability is aggregated into an "aggregation value" G_i (Park et al., 2009)

$$G_i = \frac{\sum_j W_{i,j} Q_j P_i(V_j)}{\sum_j W_{i,j} Q_j} \quad , \tag{4.1}$$

where $P_i(V_j)$ is the membership function, as explained above, for the polarimetric measured variable j with value V_j. To reflect the varying relevance between different polarimetric variables on detection of hydrometeor classes, a weighting function

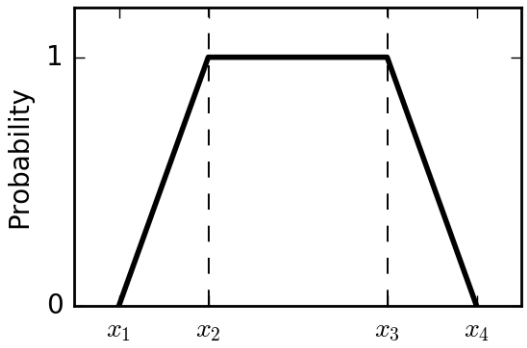

FIGURE 4.1: Trapezoidal membership function as described in the text.

$W_{i,j}$ is used. Also, Park et al. (2009) introduce a confidence vector Q_j to take the quality of the measurements into account. Depending on the algorithm, different polarimetric variables and restrictions are used. E.g. Park et al. (2009) utilize horizontal reflectivity factor Z_h, differential reflectivity Z_{DR}, correlation coefficient ρ_{hv}, the specific differential phase Φ_{DP} (in logarithmic scale) and spatial fluctuations of Z_h and Φ_{DP}. Finally, the hydrometeor class with the highest aggregation value is chosen.

4.1.2 Hail size discrimination algorithm at S band

Ryzhkov et al. (2013b) and Ortega et al. (2016) introduce a hail size discrimination algorithm (HSDA), which is based on the concept of the fuzzy logic hydrometeor classification algorithm (HCA; Park et al., 2009). In areas where the HCA identifies a rain / hail mixture, the HSDA further discriminates between the three hail size classes, small (diameter $D < 2.5\,\text{cm}$), large ($2.5\,\text{cm} \leq D < 5\,\text{cm}$) and giant hail ($D \geq 5\,\text{cm}$). "These [three] classes were chosen on the basis of current [National Weather Service] thresholds for severe-hail criteria" (Ortega et al., 2016, p. 830). Trapezoidal membership functions are used for the polarimetric variables horizontal reflectivity factor Z_h, differential reflectivity Z_{DR}, and co-polar correlation coefficient ρ_{hv} to distinguish hail sizes.

Similar to Park et al. (2009), Ortega et al. (2016) use the relative height with respect to the melting layer as an additional constraint to distinguish between hydrometeor types. The HSDA discerns six height intervals, which are dependent on the wet-bulb temperature. For each height interval, different parameters for the trapezoidal membership functions are used (as shown e.g. in Table 2 in Ortega et al., 2016).

The result of the fuzzy logic hydrometeor classification and hail size discrimination is dependent on the restrictions being made, but even more on the parameters set for the membership functions. Therefore, these parameters have to be chosen carefully, e.g. by utilizing scattering simulations, and require a good evaluation.

4.2 T-Matrix Scattering Simulations

Scattering of electromagnetic waves by nonspherical particles is not a trivial task to calculate. The transmission matrix $\bar{\bar{T}}$ or T-matrix, originally introduced by Waterman (1971), allows for precise scattering simulation without the need of a Rayleigh approximation (Ryzhkov et al., 2010). As shown in equation 2.15, the T-matrix is independent of the incident and scattered wave. As long as the shape, size and refractive index of the particle do not change, the T-matrix only needs to be calculated once. Therefore, any particle orientation can be calculated without the necessity to recalculate the whole scattering processes (Mishchenko et al., 1996, p. 537). Mishchenko et al. (1996) describe this method as "especially attractive mathematically and efficient and powerful numerically" (p. 535). Because of this efficiency, the T-matrix approach is used in many meteorological scattering simulations. For nonspherical single layered spheroids a FORTRAN code (Mishchenko, 2000) as well as a python module (Leinonen, 2014) is available to the public. With this, e.g. dry hail can be simulated for various sizes.

Although Ryzhkov et al. (2010) mention that smaller, melting hail can be simulated with a single layered spheroid, as long as the mass water fraction is equal and the hail is not too large, they strongly recommend to use double layered spheroids for water coated hail. Especially large hail with low mass water fraction would produce a much larger error if no double layered spheroid is used (Figure 3 & 4 in Ryzhkov et al., 2010). Here, the more complex approach for double layered spheroids following Ryzhkov et al. (2010) and Ryzhkov et al. (2013a) is used.

4.2.1 Dual-layered scattering simulations

A T-matrix simulation for dual-layer spheroids is used to estimate scattering characteristics of melting hail. The inner layer consists of solid ice, coated with a layer of water. Refractive indices of ice and water are calculated based on equations from Cole and Cole (1941) and Zhang (2016). Single-layer scattering simulations typically require an effective medium approximation to estimate dielectric constants for particles like melting hail, which are mixtures of water and ice. Although different approaches exist, all come with their specific advantages and disadvantages (Zeng et al., 2016). Using dual-layer scattering simulation eliminates the problem of calculating dielectric constants with mixed media, like melting hail, when only pure ice and water, i.e. without air-inclusions, are used for each layer. However, the formulas used by Zhang (2016) are based on square-fitted experiment data and thus may introduce other uncertainties. The dielectric constants used align with Ryzhkov et al. (2010).

The results of this dual-layered simulation code are consistent with another dual-layer T-matrix study of wet hail (Depue et al., 2007), as shown in Figure 4.2. For both differential reflectivity and linear depolarization ratio the curves exhibit similar shapes compared to Depue et al. (2007). There are some differences though,

e.g. the values of Z_{DR} are overall a bit lower (by $\sim$ 0.2 dB) and LDR has a much lower minimum at 30 mm ($\sim$ 3 dB lower) in this simulation. Also, in the simulations shown here the outer diameter of the water coated particles is 0.5 mm bigger than the inner diameter. However, a 0.5 mm thick water coat is described in Depue et al. (2007), i.e. the equivolume diameter of the outer water spheroid and the inner ice spheroid should differ by 1 mm. This led to slightly different results, though. Therefore, only a water coat of 0.25 mm, i.e. the outer diameter is 0.5 mm bigger than the inner diameter, is shown in the simulations. Since the exact refractive indices and temperatures used in Depue et al. (2007) are unknown, it is reasonable to assume that the differences in the shown curves might be due to an unknown difference in the refractive indices.

Figure 4.3 shows the simulated polarimetric variables at C band using the dual-layer T-matrix code for wet hail with the set of parameters shown in Table 4.1. Reflectivity factor, differential reflectivity, cross-correlation coefficient, and linear depolarization ratio indicate strong resonance effects for hail diameters of 19 mm and less pronounced effects for diameters of 88 mm. At these resonance diameters, values of multiple simulated polarimetric variables reach both minima and maxima. Among all polarimetric variables, only specific attenuation A_h exhibits monotonic increase for hail diameters exceeding 15 mm. This makes specific attenuation A_h a very promising parameter for hail size discrimination at C band. Other variables show extreme fluctuations and therefore their use for hail size discrimination might be ambiguous if used exclusively.

TABLE 4.1: Parameters for a dual-layered hail scattering simulation.

	axis ratio	icecore density	thickness of water coat	simulation steps	Std. dev. canting angle	temperature	radar wavelength
	(1)	($g\,cm^{-3}$)	(mm)	(mm)	(°)	(°C)	(mm)
Wet hail	0.75	0.93	0.10	0.10	40	0.0	53

4.2.2 Dual-layer vs. single-layer

To further test the plausibility of the dual-layered T-matrix code, it is compared with the evaluated single-layer T-matrix code from Leinonen (2014), i.e. the Python implementation of the code from Mishchenko and Travis (1998). Both T-matrix simulations are performed for dry hail with diameters of less than 30 mm. For the dual-layer simulation, the outer and inner layer are set up with equal parameters to mimic scattering behavior of a single-layered particle. The results of the single-layer T-matrix simulation, together with the dual-layer T-matrix simulation with double precision and quadruple precision, are shown in Figure 4.4. Generally the

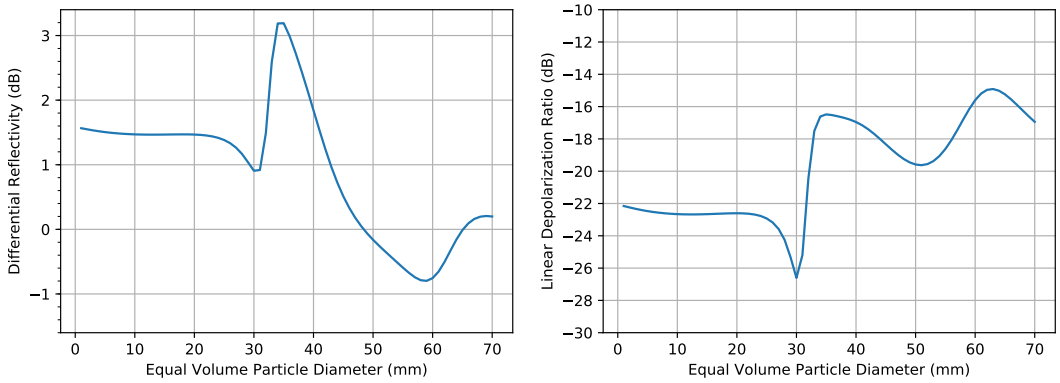

FIGURE 4.2: T-matrix scattering simulation of differential reflectivity (left panel) and linear depolarization ratio (right panel) against equal volume particle diameter for a particle with a solid ice core and a water coat of 0.5 mm total thickness. Simulation parameters are chosen accordingly to Depue et al. (2007) to compare with their wet hail simulation (see their Figure 2, dashed line "W25").

results differ from Figure 4.3 as dry hail has different scattering properties, and resonance effects differ between dry and wet hail. Although equal simulation parameters are used for both single- and dual-layered simulations, and most lines align in terms of their shape, the simulations exhibit differences of up to e.g. 0.2 dB for Z_{DR}, $\sim 1\,\mathrm{dB\,km^{-1}}$ for A_h and ~ 8 dBZ for Z_h. Other polarimetric variables like e.g. ρ_{hv} show diverse resonance effects with peak-like behavior for dual-layered simulations but asymptotic behavior for single-layered simulations between 22 mm to 26 mm. Also, LDR and Z_{DR} demonstrate such pronounced differences. Additionally, the dual-layer T-matrix simulation shows less spurious fluctuations. Nevertheless, the differences between single- and dual-layered simulations are mostly minor compared to their magnitude. With the confidence achieved based on the intercomparison for dry hail, the dual-layer code is used for the ensuing development of the HSDA, where melting hail has to be taken into account.

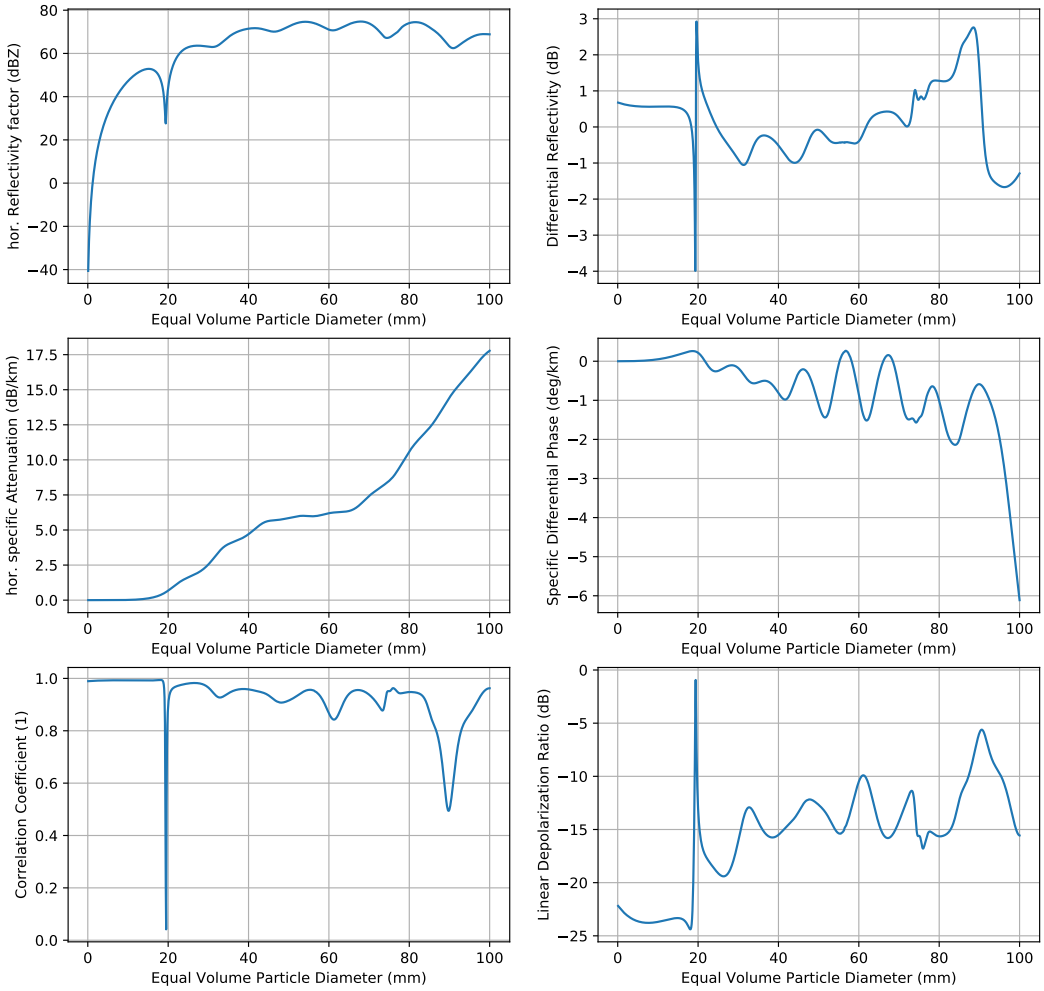

FIGURE 4.3: T-matrix scattering simulation of Z_h (upper left panel), Z_{DR} (upper right panel), A_h (middle left panel), K_{DP} (middle right panel), ρ_{hv} (lower left panel) and LDR (lower right panel) against equal volume particle diameter for wet hail. The simulation parameters are given in Table 4.1.

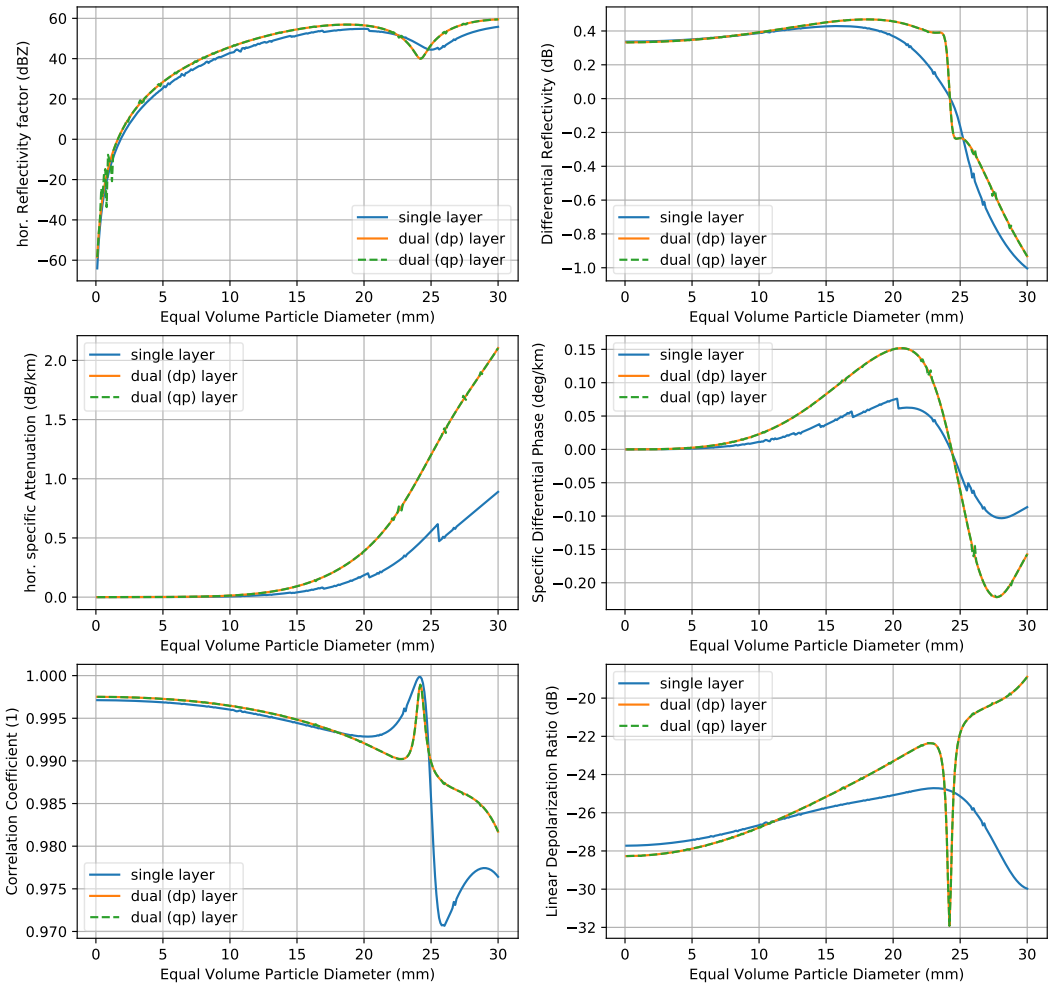

FIGURE 4.4: T-matrix scattering simulation with single-layered (blue solid line) and dual-layered particles, the latter calculated in double (dp; solid orange line) and quadruple precision (qp; dashed green line). Shown are the polarimetric variables Z_h (upper left panel), Z_{DR} (upper right panel), A_h (middle left panel), K_{DP} (middle right panel), ρ_{hv} (lower left panel) and LDR (lower right panel) against equal volume particle diameter. The particles are composed of solid ice at 0 °C, have an axis-ratio of 0.75 and the standard deviation of the canting-angle distribution is 40°.

4.3 A New Hail Size Discrimination Algorithm For C Band

Before a hail size discrimination can be applied, hail needs to be detected first, regardless of size. E.g. the S-band HSDA (Ortega et al., 2016) can only discriminate hail which is already detected by a hydrometeor classification algorithm (Ryzhkov et al., 2013b). Therefore, hail detection at C band is investigated first to allow a similar approach to be followed.

In order to assess the applicability of the HSDA developed for S band by Ortega et al. (2016) to C-band radar measurements, C- and S-band measurements are required for the same hail-bearing storm. For this purpose two quasi-collocated radar sites in Alabama, KEOX[1] (S band) and EEC[2] (C band), are used. The sites are approximately 40 km apart from each other.

A two-layer T-matrix scattering model is used to obtain scattering amplitudes of dry and wet hail. The code for the model used here is the same as in Ryzhkov et al. (2013a). Temperature dependent dielectric constants are calculated following Cole and Cole (1941) and Zhang (2016).

The shape of the hydrometeors also impacts the scattering characteristics and relies on already published models and assumptions. The axis-ratio γ for rain droplets with diameter D (in mm) is calculated following Ryzhkov et al. (2010)

$$\gamma = 0.9951 + 0.02510 \cdot D - 0.03644 \cdot D^2 + 0.005303 \cdot D^3 - 0.0002492 \cdot D^4 \,. \tag{4.2}$$

For dry, small hail/graupel with diameter D the axis-ratio γ is estimated following Ryzhkov et al. (2010)

$$\gamma = \begin{cases} 1 - 0.02 \cdot D & \text{if } D < 10\,\text{mm}\,, \\ 0.8 & \text{if } D \geq 10\,\text{mm}\,. \end{cases} \tag{4.3}$$

Tumbling of hydrometeors is considered with a "two-dimensional axissymmetric gaussian distribution of orientations" (Ryzhkov et al., 2010). By providing a standard deviation of the canting angle, angular moments can be calculated. The polarimetric variables are then calculated using the scattering amplitudes obtained by the T-matrix and the angular moments as described in Ryzhkov et al. (2010).

4.3.1 Performance of the unmodified algorithm

Park et al. (2009) presented a hydrometeor classification algorithm (HCA). It is used operationally and was extended to discriminate between small, large and giant hail (see Ortega et al. (2016)). As the HSDA is based on the HCA and requires HCA's hail detection in order to discriminate hail, the applicability of the HCA at C band is investigated first.

[1] KEOX is not an abbreviation, but the four letter location identifier of the International Civil Aviation Organization (ICAO) of the radar site.

[2] EEC stands for the manufacturer Enterprise Electronics Corporation on whose ground the radar is located, too.

Figure 4.5 shows the application of the HCA to two quasi-colocated S- and C-band radars (provided by courtesy of Pengfei Zheng (NSSL)). Application of the S-band measurement (see Figure 4.5a) reveals widespread rain with some cells bearing heavy rain and hail. Further away only snow is detected as the melting layer is passed. The classification seems to be quite plausible for this example. For the same date and time the close-by C-band radar captured the same storm. However, results of the HCA at C band are different (Figure 4.5b). First of all, the C-band radar suffers from strong attenuation at locations where hail was detected with S-band data. This is not a shortcoming of the applied algorithm as this problem is related to wavelength properties. However, for a successful hydrometeor classification and hail discrimination at C band, attenuation is highly recommended being monitored and included in the algorithm (as pointed out in section 4.2.1 and Schmidt et al. (2017)).

Secondly, most of the area is classified as big drops instead of rain and almost no hail was detected. A possible reason for the failure of the published HCA at C band is that reflectivity and differential reflectivity for hail at C band is generally lower than at S band (see e.g. Figure 8 and 15 in Ryzhkov et al. (2013a)). Clearly, proper adjustments to the algorithms have to be elaborated before hail size can be discriminated or hail detected at C band at all.

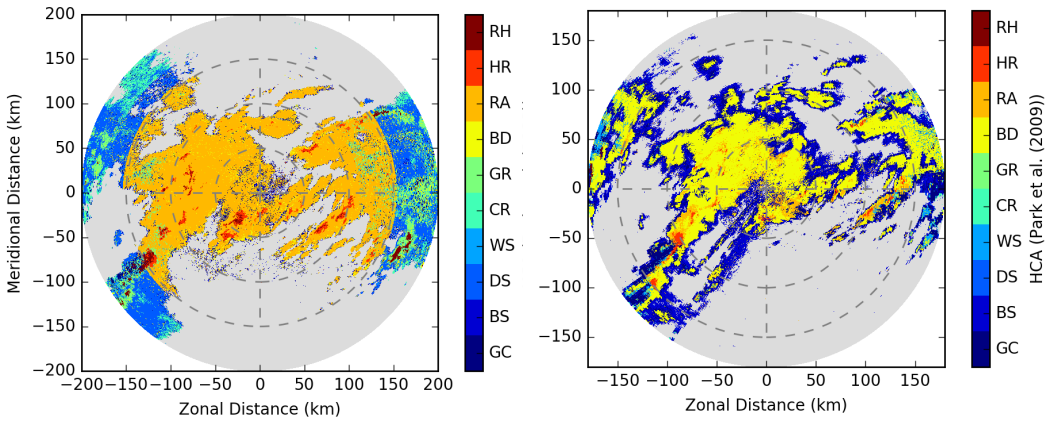

(A) S band (KEOX) (B) C band (EEC)

FIGURE 4.5: The hydrometeor classification algorithm (HCA) as in Park et al. (2009) for two quasi-colocated radar sites, a) KEOX and b) EEC, in Alabama, USA, measured on January 21, 2017 16:43 UTC. The ordinate shows the meridional and the abscissa the zonal distance from the radar site in km. The gray color marks areas without classifiable echoes inside the radar range. The different hydrometeor classes are indicated by color. Here RH is an abbreviation for rain and hail mixture, HR for heavy rain, RA for rain, BD for big drops, GR for graupel, CR for ice crystals, WS for wet snow, DS for dry snow, BS for biological scatter and GC for ground clutter (compare with Park et al. (2009)).

4.3.2 Simulated hydrometeors

To obtain useful parameters for the fuzzy logic, a broad variety of hydrometeors need to be simulated. The following simulations only include rain and hail particles,

since only spheroids can be simulated and the distinction between rain and hail is most crucial.

To simulate all possible rain drops which could appear in the radar volume, a variety of different settings has to be considered in the simulations. The following specifications of simulation parameters should cope with all probable kinds of rain drops to some extent:

- Using the dual-layer code for raindrops. Both the inner and outer layer consist of liquid water.
- Dielectric constants are calculated for 30 °C, 20 °C, 10 °C and 0 °C.
- Drop diameters from 0.1 mm and up to 50 mm are used with a step size of 0.1 mm.
- Tumbling: Canting angle distributions have standard deviations of 7°, 10°, 20° or 45°.
- Axis-ratio of droplets depends on drop diameter and follows equation 4.2.

In addition to rain, big drops are added with their own category. The specifications are set equal to rain drops, except for the drop diameters, which range from 50 mm up to 60 mm.

For hail - in general - other specifications are important. Not only can hail be dry and wet, but also appears in various combinations of size, shape and density. Later on three size categories for hail will be used: small hail ($D < 2.5$ cm), large hail ($2.5\,\text{cm} \leq D < 5\,\text{cm}$) or giant hail ($D \geq 5$ cm). Therefore, the simulation results will be split into these three groups as well. The following specifications for hail will be considered in the simulations:

- The medium of the inner layer is solid ice, while the outer is either solid ice (dry hail) or liquid water (wet hail).
- If the outer medium is liquid, the water coat will be simulated to be 0.5 mm thick. I.e. the outer diameter is 1 mm thicker than the diameter of the inner medium.
- Dielectric constants are calculated at 20 °C, 0 °C and −10 °C for each medium, i.e. various combinations of different temperatures are possible for the mixed-phase hydrometeors.
- Particle diameters from 1 mm up to 24 mm (small hail), 25 mm up to 49 mm (large hail) and 50 mm up to 100 mm (giant hail), each with 1 mm step-size, are used.
- Tumbling: Canting angle distributions have standard deviations of 7°, 10°, 20° or 45°.

- Axis-ratio for small hail follows equation 4.3. For large and giant hail it will be set to 0.5, 0.6, 0.7, 0.8, 0.85, 0.9, 0.95 and 1.0. I.e. 8 different axis-ratios are simulated for each hail diameter $\geq 25\,\text{mm}$.

For each hydrometeor type the simulation results are presented as colored histograms in Figures 4.7 (small, wet hail), 4.8 (small, dry hail), 4.9 (large, wet hail), 4.10 (large, dry hail), 4.11 (giant, wet hail), 4.12 (giant, dry hail), 4.13 (rain) and 4.14 (big drops) along with their trapezoidal membership functions, which were obtained by using the 5, 25, 75 and 95 percentiles of the simulated polarimetric values. The histograms for small hail (Figure 4.7 & 4.8) and liquid particles (Figure 4.13 & 4.14) are shown for different standard deviations of the canting angle distribution. Their axis-ratios are set by the function shown in equation 4.3 for small hail and equation 4.2 for rain. The results for large and giant hail did not demonstrate a dependency on the canting angle distributions. Accordingly, the histograms for large and giant hail (Figure 4.9 & 4.10 and Figure 4.11 & 4.12) are separated by axis-ratios, for which a dependency is visible.

Dry, small hail (Figure 4.8) exhibits much smaller Z_{DR} (up to 1.5 dB) than wet, small hail (Figure 4.7). ρ_{hv} shows a broader distribution for wet, small hail compared to dry, small hail, where the values seem to be monodisperse. A similar behavior is observed for A_h and DR, where the distributions of wet, small hail are almost uniform. This is in contrast to dry, small hail, where more values are close to 0. Vice versa, the Z_h values are distributed equally for small, dry hail between 40 dBZ and $\sim$ 64 dBZ, but bimodal for wet, small hail. Here the values mainly are concentrated well above 65 dBZ and do not exceed 80 dBZ. A secondary, smaller peak is present at 40 dBZ. K_{DP} is mostly positive and up to $5\,^\circ\,\text{km}^{-1}$ for dry, small hail, whereas wet, small hail shows equally positive and negative values between $-20\,^\circ\,\text{km}^{-1}$ to $15\,^\circ\,\text{km}^{-1}$, with most values around $0\,^\circ\,\text{km}^{-1}$.

Hail diameters exceeding a specific diameter, dependent on the wavelength and whether the particle is water coated or not, tend to have negative K_{DP} due to strong resonance effects (e.g. see Figure 4.3 or Ryzhkov et al. (2013a), Figure 8e&f). Nevertheless, K_{DP} of $-20\,^\circ\,\text{km}^{-1}$ seems to be quite extreme for small hail. Such values only occur for rare resonance sizes at low standard deviations of the canting angle distribution, and with water coats of 0.5 mm e.g. as shown in Figure 4.6. Here K_{DP} already drops below $-20\,^\circ\,\text{km}^{-1}$ at a diameter of 9 mm (Figure 4.6b). A less spurious and more gradual decrease of K_{DP} with hail size is only visible for thinner water coats (Figure 4.6a).

For small hail, the different canting angle distributions mostly affect Z_{DR}, K_{DP}, but not so much other polarimetric variables. This is expected as Z_{DR} is reduced for tumbling particles and K_{DP} is dependent on the particle orientation, as indicated in section 2.1.2.

Large, wet hail (Figure 4.9) and giant, wet hail (Figure 4.11) mostly exhibit similar distributions, albeit with different magnitudes. E.g. Z_{DR} is centered around 0 dB with values between -6 dB to 6 dB and -11 dB to 11 dB for large and giant wet

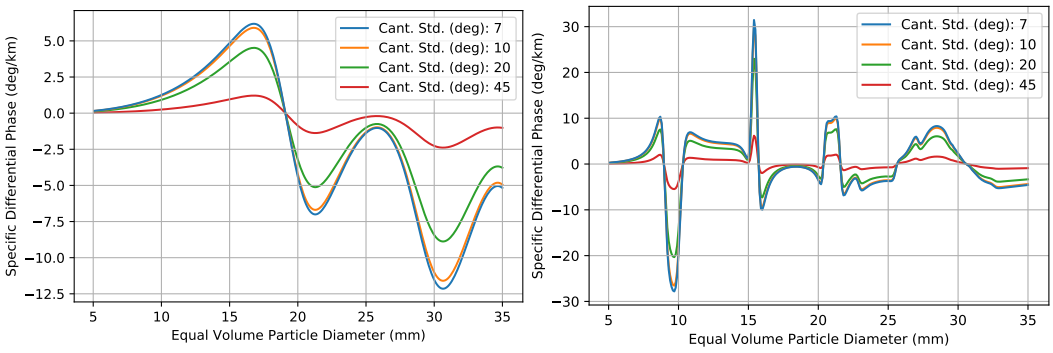

(A) water coat is 0.1 mm thick

(B) water coat is 0.5 mm thick

FIGURE 4.6: T-matrix scattering simulation of K_{DP} for wet hail with a) 0.1 mm thick water coat and b) 0.5 mm thick water coat for canting angle distributions with standard deviations of 7°, 10°, 20° and 45°. Other simulation parameters are given in Table 4.1.

hail respectively. Similarly, K_{DP} is centered around $-3\,\mathrm{dB\,km^{-1}}$ for large, wet hail and reach values between $-286\,\mathrm{dB\,km^{-1}}$ to $73\,\mathrm{dB\,km^{-1}}$, while the center for giant, wet hail is around $-16\,\mathrm{dB\,km^{-1}}$ and ranges from $-20\,\mathrm{dB\,km^{-1}}$ to $20\,\mathrm{dB\,km^{-1}}$. Almost identical distributions exist for DR, where two modes are visible, one centered around -20 dB and a smaller one between -80 dB to -60 dB. Here, a strong dependency on the axis-ratio is visible, going from almost 0 dB for an axis-ratio of 0.5 to -80 dB for an axis-ratio of 0.999. This is expected, as DR is highly dependent on the particle shape. Also, ρ_{hv} shows very similar distributions between the two size categories. Most values peak close to 1 and strongly decrease until 0.65 for large and 0.6 for giant wet hail. Both large and giant wet hail exhibit two modes in Z_h with their primary mode centered around 80 dBZ. A secondary mode is visible around 70 dBZ for large and around 95 dBZ for giant wet hail. The latter is primarily generated by very oblate particles with axis-ratios of 0.6 and 0.5, which even exceed 100 dBZ.

The distributions of large, dry hail (Figure 4.10) and giant, dry hail (Figure 4.12) show more pronounced differences compared to their wet counterparts. E.g. Z_{DR} is centered around -0.7 dB and ranging from -6 dB to 7 dB for giant dry hail, while large dry hail is much more broadly distributed with a maximum at -0.25 dB and decaying from 1 dB to -12 dB. Nevertheless, ρ_{hv} and DR show identical distributions between large and giant dry hail. DR exhibits, similar to the wet hail, a strong dependency on the axis ratio. Large, dry hail demonstrates only negative K_{DP} from $-80\,^\circ\,\mathrm{km^{-1}}$ to $0\,^\circ\,\mathrm{km^{-1}}$, where values between $-80\,^\circ\,\mathrm{km^{-1}}$ to $-40\,^\circ\,\mathrm{km^{-1}}$ are only observed for very oblate particles with axis-ratios of 0.6 and 0.5. Giant, dry hail extends to positive values of K_{DP} ranging from $-200\,^\circ\,\mathrm{km^{-1}}$ to $55\,^\circ\,\mathrm{km^{-1}}$. The particles causing positive K_{DP} have an axis-ratio of 0.8 and above. A_h does not demonstrate a dependency on axis-ratio for large and giant dry hail. The distribution is mostly uniform between $14\,\mathrm{dB\,km^{-1}}$ to $78\,\mathrm{dB\,km^{-1}}$ for large, dry hail and between $56\,\mathrm{dB\,km^{-1}}$ and $200\,\mathrm{dB\,km^{-1}}$ with a peak at $75\,\mathrm{dB\,km^{-1}}$ for giant, dry hail. A tendency towards higher Z_h values for more spherical axis-ratios is visible for both large and giant dry hail, albeit a bit less for the former size. The distribution is centered around 82 dBZ

for giant and around 71 dBZ for large dry hail.

Simulated rain drops (Figure 4.13) and big drops (Figure 4.14) differ in all shown distributions despite the fact that both are liquid. E.g. big drops do range from 20 dBZ to 65 dBZ in Z_h, but most values are centered around 50 dBZ. Rain drops have their maximum at 27 dBZ, but values are distributed with decreasing likeliness down to −28 dBZ. Almost all values of ρ_{hv} for rain drops concentrate at 1, except for a few resonance cases, while values for big drops seem to be equally spread between 0.5 and 0.95. Similarly, K_{DP} values for rain drops are positive only and are mostly concentrated close to $0\,^\circ\,\mathrm{km}^{-1}$. K_{DP} for big drops spreads almost equally between $-1.75\,^\circ\,\mathrm{km}^{-1}$ to $1.6\,^\circ\,\mathrm{km}^{-1}$, except for a slight drop around $-0.5\,^\circ\,\mathrm{km}^{-1}$ and a peak at $0\,^\circ\,\mathrm{km}^{-1}$. As expected, A_h is very low ($\ll 0.1\,\mathrm{dB\,km}^{-1}$) for rain drops. Big drops show low values, but also have a secondary maximum reaching values of up to $0.41\,\mathrm{dB\,km}^{-1}$.

Also, canting angle distributions show stronger dependency for big drops than for rain drops. This is well visible in e.g. the histogram for DR, where big drops with values between −10 dB to −5 dB are mostly dominated by particles with wider canting angle distributions, while values closer to 0 dB are mainly produced by particles with narrow canting angle distributions. Rain drops cover DR ranges from −80 dB to −1 dB, but do not show a similar dependency on the canting angle distribution. Similarly, Z_{DR} for big drops ranges from −12 dB to 27 dB, with clear domains for each of the four simulated canting angle distributions. Rain drops exhibit positive values mainly between 0 dB to 3 dB, except for a few resonance cases. A weak dependency on the canting angle distribution is visible in the sense that particles with a canting angle standard deviation of 45° only appear close to 0 dB.

The derived trapezoidal membership functions are also shown in Figure 4.15 to facilitate the comparison between different hydrometeor types. Here Z_h indicates good capabilities to distinguish between various hail sizes and between rain and hail. However, size categories for wet hail overlap more and big drops overlap with small hail, too. Surprisingly, Z_{DR} seems to be less helpful. For wet hail all size categories overlap. Distinction between rain and hail appears to be difficult with Z_{DR} at C band, although this polarimetric variable is very valuable at S band (Anderson et al., 2011; Ryzhkov et al., 2013a). Trapezoidal membership functions for ρ_{hv} do not contribute to size discrimination capabilities at all. However, rain drops and big drops differ largely here. Most promising for hail size discrimination is A_h, for which all membership functions are clearly distinguishable. Still, the values calculated for A_h are highly doubtable to be observed at such magnitudes. The same is true for K_{DP}, where membership functions mostly included large, negative values. Typically, Φ_{DP} filtering and smoothing (see e.g. section 3.3) would filter these negative bumps out, if they ever appear in such magnitude. DR does not exhibit strong size discrimination capabilities, but is anticipated to be able to clearly distinguish spiky hail stones from smaller raindrops (Ryzhkov et al., 2017). While the first three polarimetric variables, Z_h, Z_{DR} and ρ_{hv} are available, the latter three, A_h, K_{DP} and

DR have to be estimated and/or derived after signal post-processing. This might limit the quality and therefore the possible contribution to the latter algorithm. It can be concluded that a very good combination of these variables and membership functions has to be chosen to allow for proper hail size discrimination.

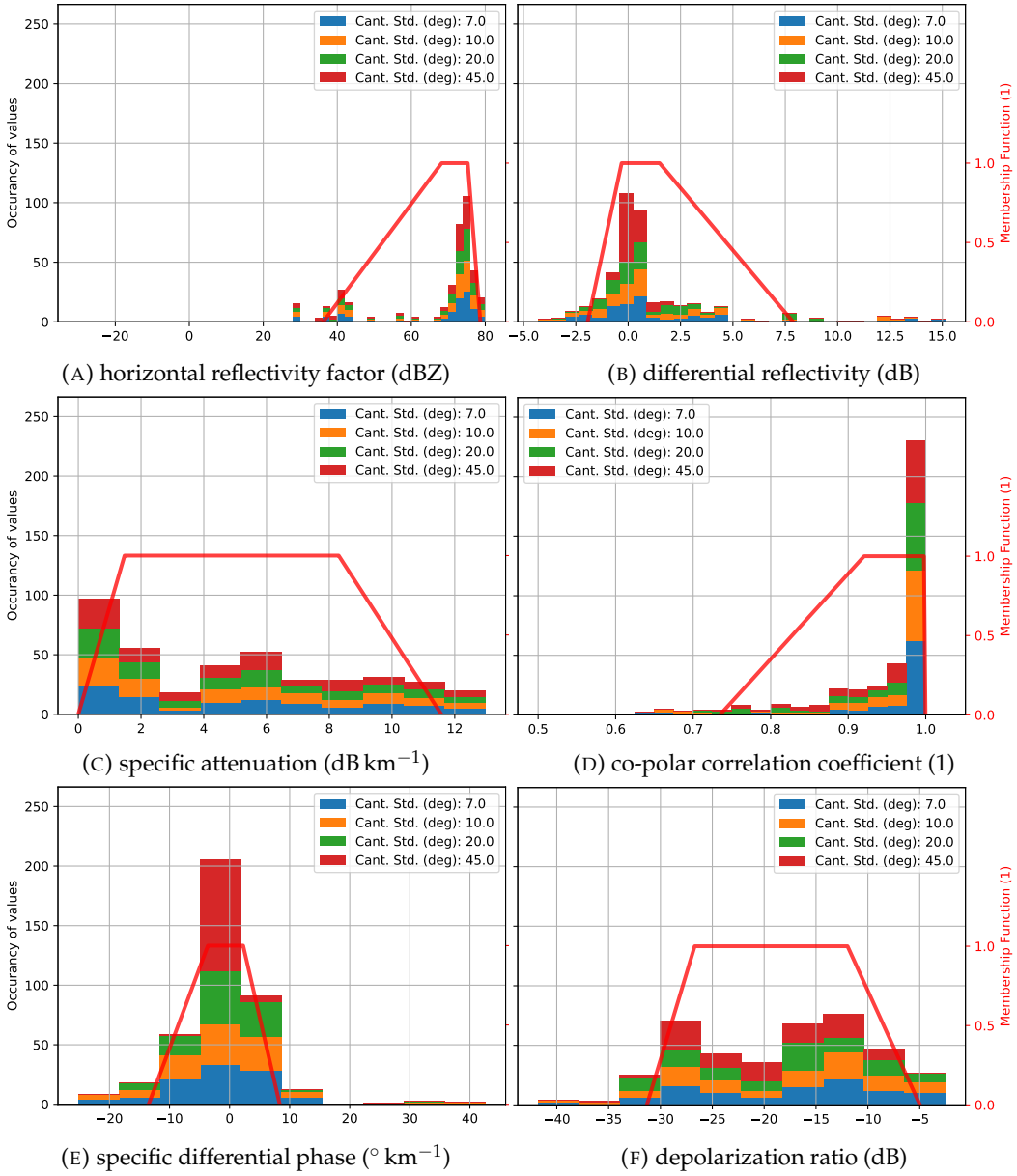

(A) horizontal reflectivity factor (dBZ)

(B) differential reflectivity (dB)

(C) specific attenuation (dB km^{-1})

(D) co-polar correlation coefficient (1)

(E) specific differential phase (° km^{-1})

(F) depolarization ratio (dB)

FIGURE 4.7: Probability of occurrence of a) Z_h, b) Z_{DR}, c) A_h, d) ρ_{hv}, e) K_{DP} and f) DR (see equation 2.36) values in T-matrix scattering simulation for small, wet hail shown as histogram for different canting angle standard deviations. The histograms consist of 30 bins. See text for simulation specifications. Trapezoidal membership function in red is obtained by using 5, 25, 75 and 95 percentiles of simulated values as parameters for the trapezoid.

4.3.3 Adjusted hail size discrimination algorithm and results

An adjusted hail size discrimination algorithm similar to Ortega et al. (2016) can be obtained using the membership functions resulting from the scattering simulations

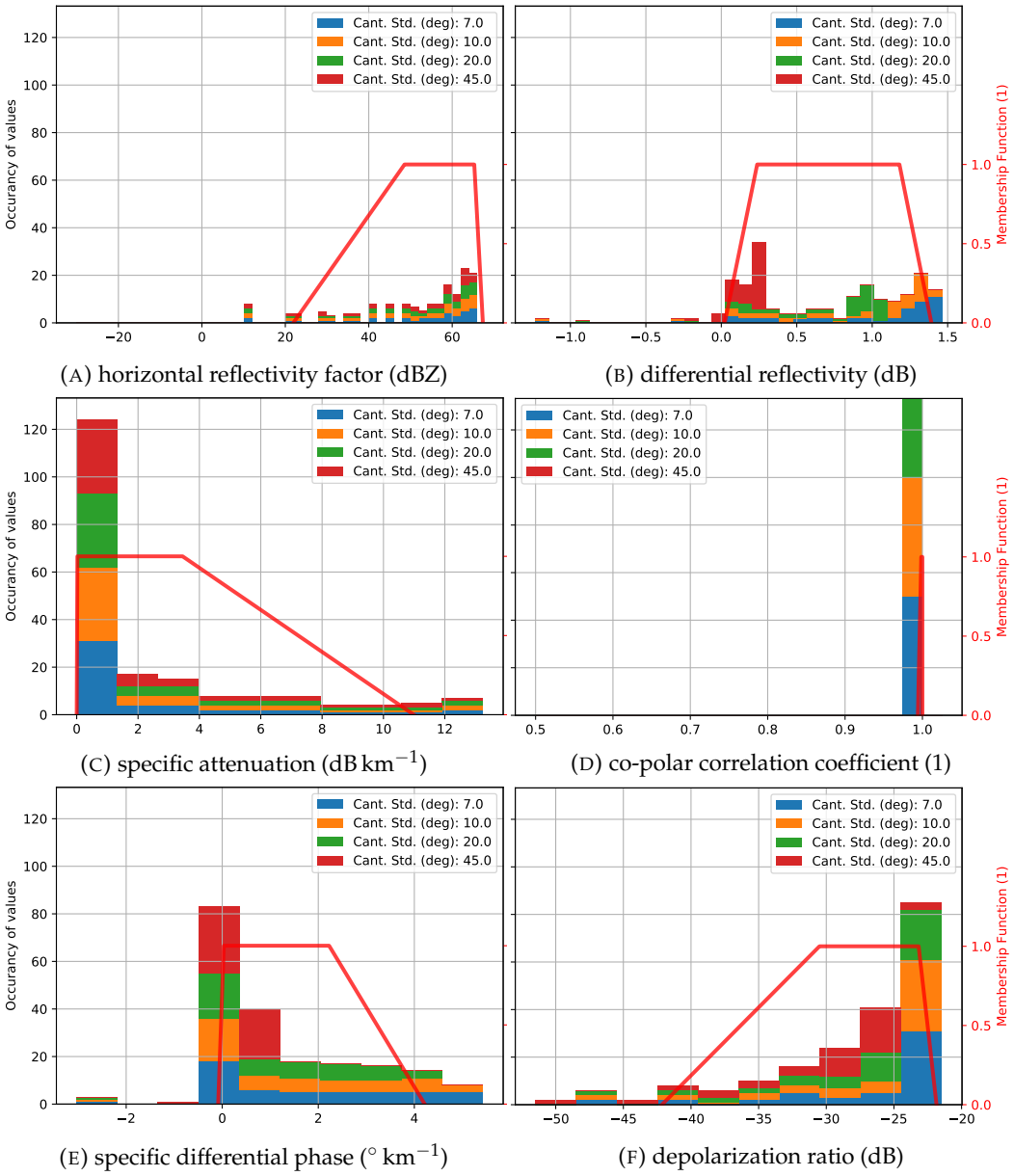

(A) horizontal reflectivity factor (dBZ)

(B) differential reflectivity (dB)

(C) specific attenuation (dB km^{-1})

(D) co-polar correlation coefficient (1)

(E) specific differential phase (° km^{-1})

(F) depolarization ratio (dB)

FIGURE 4.8: Same as Figure 4.7, but for small, dry hail.

(see Figure 4.15). As pointed out before, the weighting can influence the final results largely. In the following the performance of this HSDA using the same variables (Z_h, Z_{DR} and ρ_{hv}) and weighting (1, 0.3 and 0.6) as in Ortega et al. (2016) (see their Table 1, first row) is illustrated using an example case.

Radar Essen monitored a severe thunderstorm with multiple, hail-bearing cells on 23.06.2016. These storms destroyed roofs, chimneys, windows and cars with a damage sum of several million euros in the Netherlands and North Rhine-Westphalia with hail exceeding 7 cm in diameter[3]. Figure 4.16 shows PPIs of polarimetric variables Z_h, Z_{DR}, K_{DP}, ρ_{hv} and A_h (using the algorithm described in chapter 3) for this event at 20:00 UTC. In the PPI of the reflectivity factor (Figure 4.16a) and especially

[3]Sources: https://www.ed.nl/default/miljoenenschade-in-zuidoost~a744b3e7/ and https://www.weerwoord.be/m/2203962, last accessed on 16.12.2019, 16:22 UTC

in Z_{DR} (Figure 4.16b), effects of strong attenuation are visible for multiple, distinct cells, e.g. at 270° azimuth angle and at about $\sim$ 80 km range, at 300° azimuth angle and at about $\sim$ 50 km range, at 230° azimuth angle and at about $\sim$ 130 km range, at 15° azimuth angle and at about $\sim$ 100 km range, and at 30° azimuth angle and at about $\sim$ 125 km range. These attenuation effects emerge as shadows behind the hail core e.g. with negative Z_{DR} falling below -4 dB and total signal extinction (at 310° azimuth and 95 km). Within these cells specific differential phase is around 5 ° km^{-1} to 9 ° km^{-1} and specific attenuation exceeds 2 dB km^{-1}. Co-polar correlation coefficient ρ_{hv} drops below 0.9 in the hail cores and below 0.5 in the shadows.

Figure 4.17 shows the hail size discrimination applied to the example case introduced using Z_h, Z_{DR} and ρ_{hv} and the membership functions from the scattering simulation results (see Figure 4.15). The weighting (1, 0.3 and 0.6) is the same as in Ortega et al. (2016) for heights 3 km above the melting layer (see their Table 1, first row). Even though the radar beam here is below the melting layer for the whole range, this weighting vector yielded the best result from all weightings in Ortega et al. (2016). Clearly, most precipitation in the PPI is classified to be big drops and small, wet hail. Also, some streaks of large, dry hail are visible. Mostly the edges of the precipitation areas are identified as rain. Only single pixels, scattered across 265° to 280° azimuth, show giant, wet hail. So far neither K_{DP} nor A_h were used, albeit the latter variable proved to have the best hail size discrimination capabilities. To include two more variables a new weighting vector has to be chosen. All possible weighting vectors with weights $W_{i,j} = \frac{n_{i,j}}{10}$, $\forall n_{i,j} \in \mathbb{Z}$, $0 \leq n_{i,j} \leq 10$ have been attempted for all hydrometeor classes i and polarimetric moments j, however none of these 1771561 weighting vectors yielded comparable or more realistic results.

Fixed weights for all radar measurements certainly do not reflect physical conditions correctly. E.g. Park et al. (2009) define a criterion for which frozen particles are only allowed in heights where the wet-bulb temperature is below 0 °C. Also, Ortega et al. (2016) split the radar beam into six temperature-based height layers and apply different weighting vectors for each.

In the following, the weights are adjusted for each point by checking how unique the membership function is for each variable, instead of setting fixed weights for polarimetric variables. I.e. the confidence vector Q_j in equation 4.1, which was always set to 1, is replaced by an overlap penalty vector O_j, so that

$$G_i = \frac{\sum_j W_{i,j} P_i(V_j) O_j}{\sum_j W_{i,j} O_j} \quad , \tag{4.4}$$

where

$$O_j = \frac{1}{\max\left[1, \sum_i P_i\left(V_j\right)\right]} \, . \tag{4.5}$$

O_j adjusts the weighting of each polarimetric value V_j at each point of measurement by the amount of overlapping membership functions between hydrometeor classes. I.e. the penalty increases if the probability is high for multiple hydrometeor classes

(e.g. see Figure 4.15c, assume measured $\rho_{hv} = 1.0$). No penalty is applied, i.e. O_j is 1, if the jth variable only contributes to a single hydrometeor class. Else, a polarimetric variable is taken into account less the more hydrometeor classes have a high membership function output, and therefore, the less this polarimetric variable can contribute to distinguish between classes. Although there might still be reasons to use fixed weights additionally, the weighting vector $W_{i,j}$ is obsolete for the following, and is therefore set to 1.

The result of the adjusted aggregation with overlap penalty is depicted in Figure 4.18. Here much more dry, small hail is classified instead of wet, small hail. Also, this is mostly in the cores of the cells. Nevertheless, the 0 °C isotherm is at 4480 km above ground level at this time and the radar beam does not reach this altitude at this elevation (0.8°). Therefore, hail is expected to be melting and not to be dry. The area between 265° to 280° azimuth angle appears noisy again, but to a lesser extent than before. Also, a hot spot with giant, wet hail is detected at −40 km zonal distance and 40 km meridional distance. Behind this hot spot attenuation effects and signal extinction were visible in Figure 4.16b.

To evaluate the different classification outputs, hail reports of the European Severe Weather Database (ESWD) are used. However, as these reports are only point observations it remains difficult to evaluate whole areas. In the simulations it became apparent that specific attenuation scales linearly with hail diameter for hail larger than 15 mm diameter. However, in simulations the particle concentration can be controlled, in observations of nature the particle concentration is difficult to estimate.

To mitigate the impact of particle number concentration, the attenuation coefficient α, defined as the ratio between A_h and K_{DP} (see Bringi et al. (1990), Table 1 or Ryzhkov et al. (2013b), equation 1), is used instead of specific attenuation A_h. Both A_h and K_{DP} depend on particle concentration (Zrnić and Ryzhkov, 1999; Rinehart, 2004) and therefore, attenuation coefficient α can serve as concentration-independent proxy for hail diameter. According to Ryzhkov et al. (2013b) the upper limit of expected α range increases with hail size, i.e. giant hail can still have low values of e.g. 0.3 dB/°, but small hail cannot reach e.g. 0.7 dB/° (see their Figure 9c).

Reported maximum hail diameters and swaths of α between 18:20 and 20:20 UTC are shown in Figure 4.19. Almost all hail reports coincide with positive values of α, except for three reports of giant hail between −50 km to −25 km zonal distance and −40 km to −20 km meridional distance, which have been missed. In the vicinity of the radar Essen, most reported diameters are above 5 cm, i.e. giant hail, and high values of α appear, which correlates well with the ranges for α given by Ryzhkov et al. (2013b). Therefore, it is reasonable to assume that areas with positive α values are areas in which hail is likely to be found on the ground.

Radar data from co-located S- and C-band radars in Alabama are used to compare the modified fuzzy logic with the original hydrometeor classification algorithm. Once again the output of the fuzzy logic using the weighting as in Ortega et al. (2016)

is depicted in Figure 4.20, which is much more realistic than the unmodified HCA applied at C band (see Figure 4.5b), but still shows differences compared to the S-band HCA output (see Figure 4.5a). E.g. a large area beyond 100 km zonal distance shows noisy giant, wet hail at edges of stronger precipitation, while the S-band output shows mostly rain and only very few graupel and crystal identified pixels. Also, the largest area with hail at S band (-125 km zonal distance and -80 km meridional distance) does not show up at C band. Many more areas of large, dry hail appear closer to the radar in the modified C-band output.

Better results can be achieved with modified C-band fuzzy logic using A_h and K_{DP} and the overlap penalty applied (Figure 4.21). A larger area is identified as rain and big drops. Also, the largest area with hail at S band (-125 km zonal distance and -80 km meridional distance) does show up with giant, wet hail surrounded by smaller, dry hail at C band. This seems plausible as ground reports in the vicinity indicate hail around 5 cm in diameter[4]. However, there is a lot of noise throughout the whole radar range with single pixels indicating arbitrary categories, especially at edges of strong precipitation. Between areas of big drops and rain, smaller areas of small, wet hail are visible. Although no hail is reported in most of these areas, a plausible assumption is that hail was aloft, but melted completely while falling. However, this assumption might not be valid in all cases, as e.g. not all of these areas show hail at S band.

[4]Source: https://www.ncdc.noaa.gov/stormevents/listevents.jsp?eventType=%28C%29+Hail&beginDate_mm=01&beginDate_dd=22&beginDate_yyyy=2017&endDate_mm=01&endDate_dd=22&endDate_yyyy=2017&county=ALL&hailfilter=0.00&tornfilter=0&windfilter=000&sort=DT&submitbutton=Search&statefips=1%2CALABAMA, last accessed on 17.12.2019 08:23 UTC

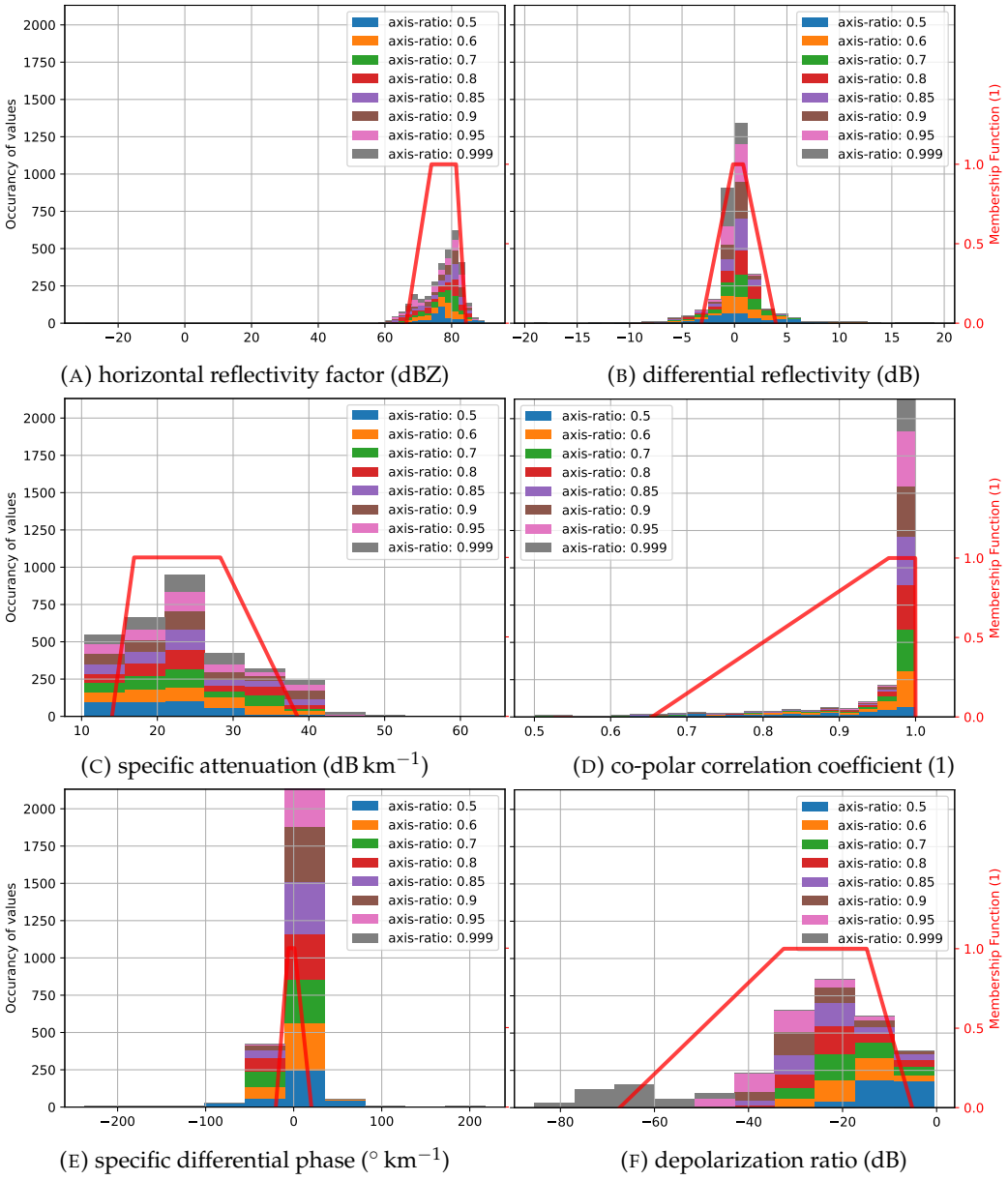

(A) horizontal reflectivity factor (dBZ)

(B) differential reflectivity (dB)

(C) specific attenuation (dB km^{-1})

(D) co-polar correlation coefficient (1)

(E) specific differential phase (° km^{-1})

(F) depolarization ratio (dB)

FIGURE 4.9: Same as Figure 4.7, but for large, wet hail and axis-ratios instead of canting angle standard deviations.

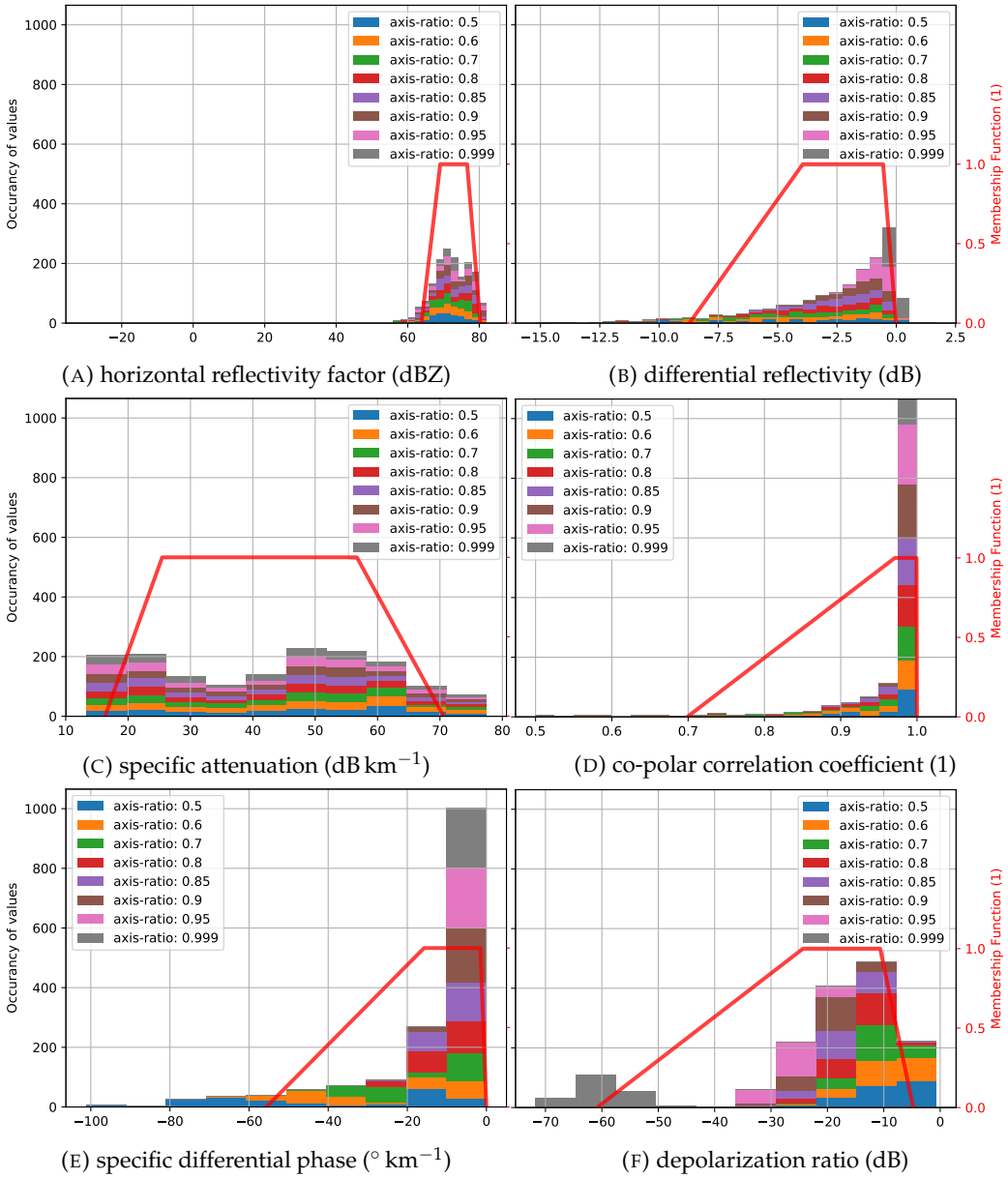

(A) horizontal reflectivity factor (dBZ)

(B) differential reflectivity (dB)

(C) specific attenuation (dB km^{-1})

(D) co-polar correlation coefficient (1)

(E) specific differential phase (° km^{-1})

(F) depolarization ratio (dB)

FIGURE 4.10: Same as Figure 4.9, but for large, dry hail.

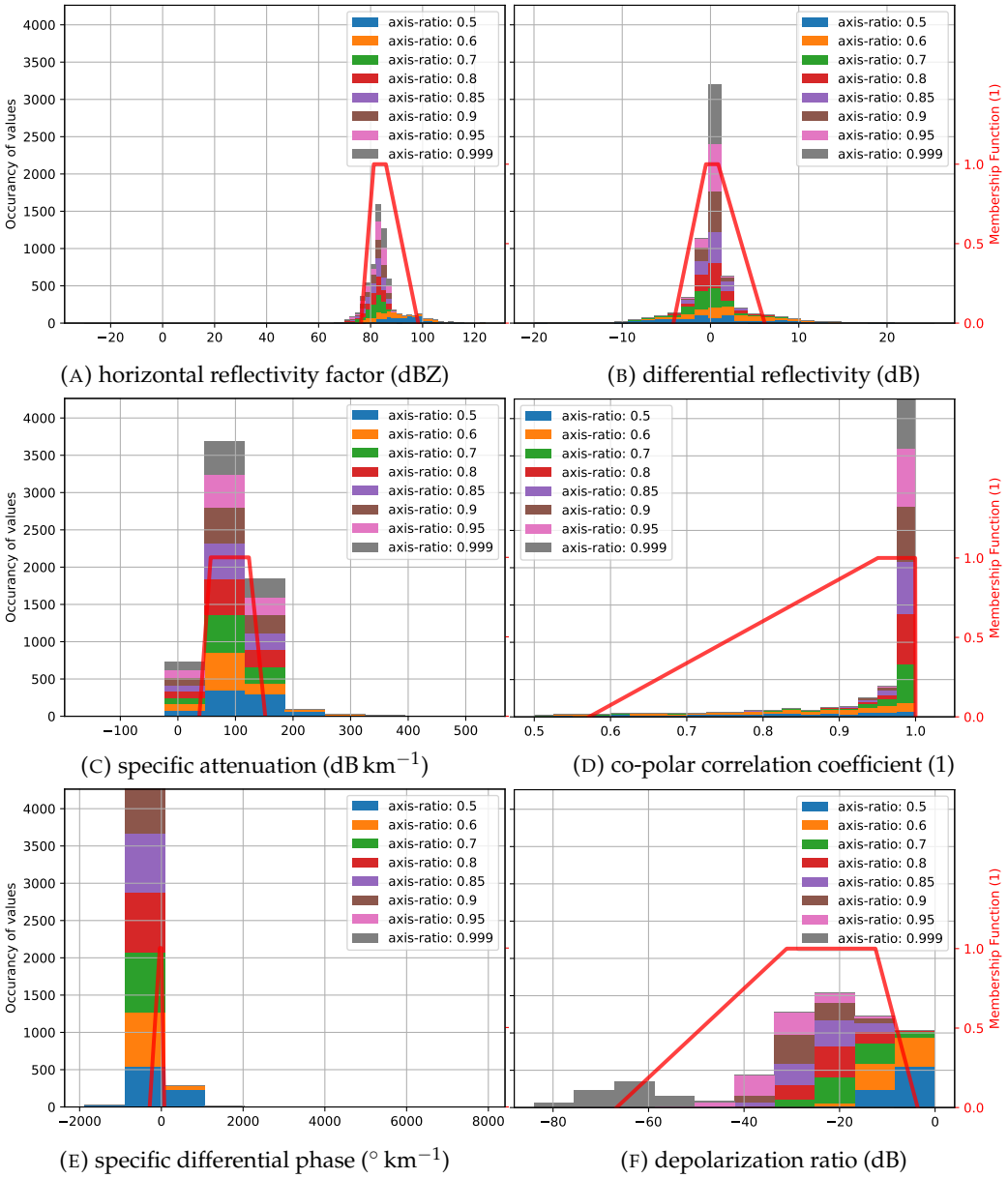

(A) horizontal reflectivity factor (dBZ)

(B) differential reflectivity (dB)

(C) specific attenuation (dB km^{-1})

(D) co-polar correlation coefficient (1)

(E) specific differential phase (° km^{-1})

(F) depolarization ratio (dB)

FIGURE 4.11: Same as Figure 4.9, but for giant, wet hail.

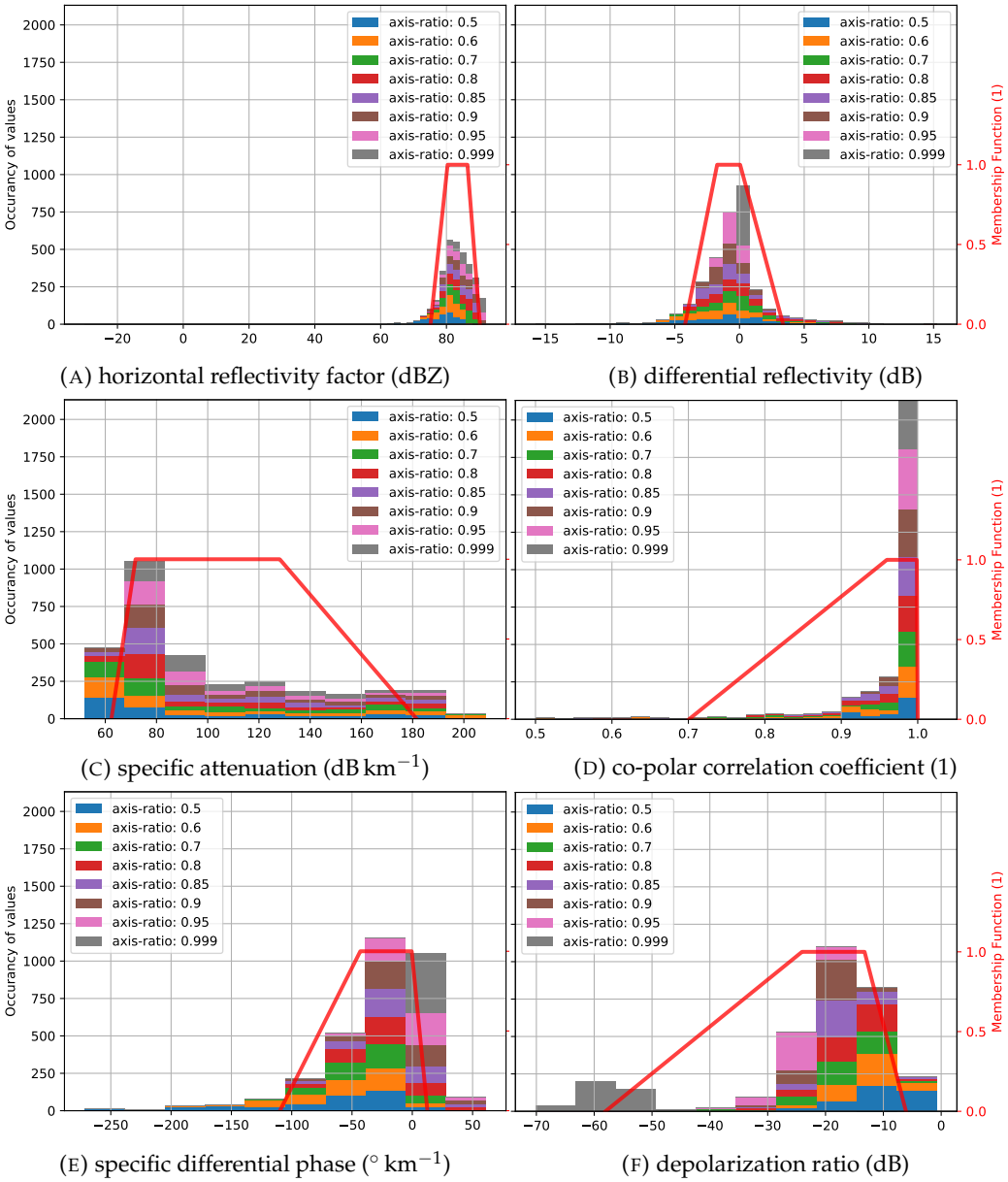

(A) horizontal reflectivity factor (dBZ)

(B) differential reflectivity (dB)

(C) specific attenuation (dB km^{-1})

(D) co-polar correlation coefficient (1)

(E) specific differential phase (° km^{-1})

(F) depolarization ratio (dB)

FIGURE 4.12: Same as Figure 4.9, but for giant, dry hail.

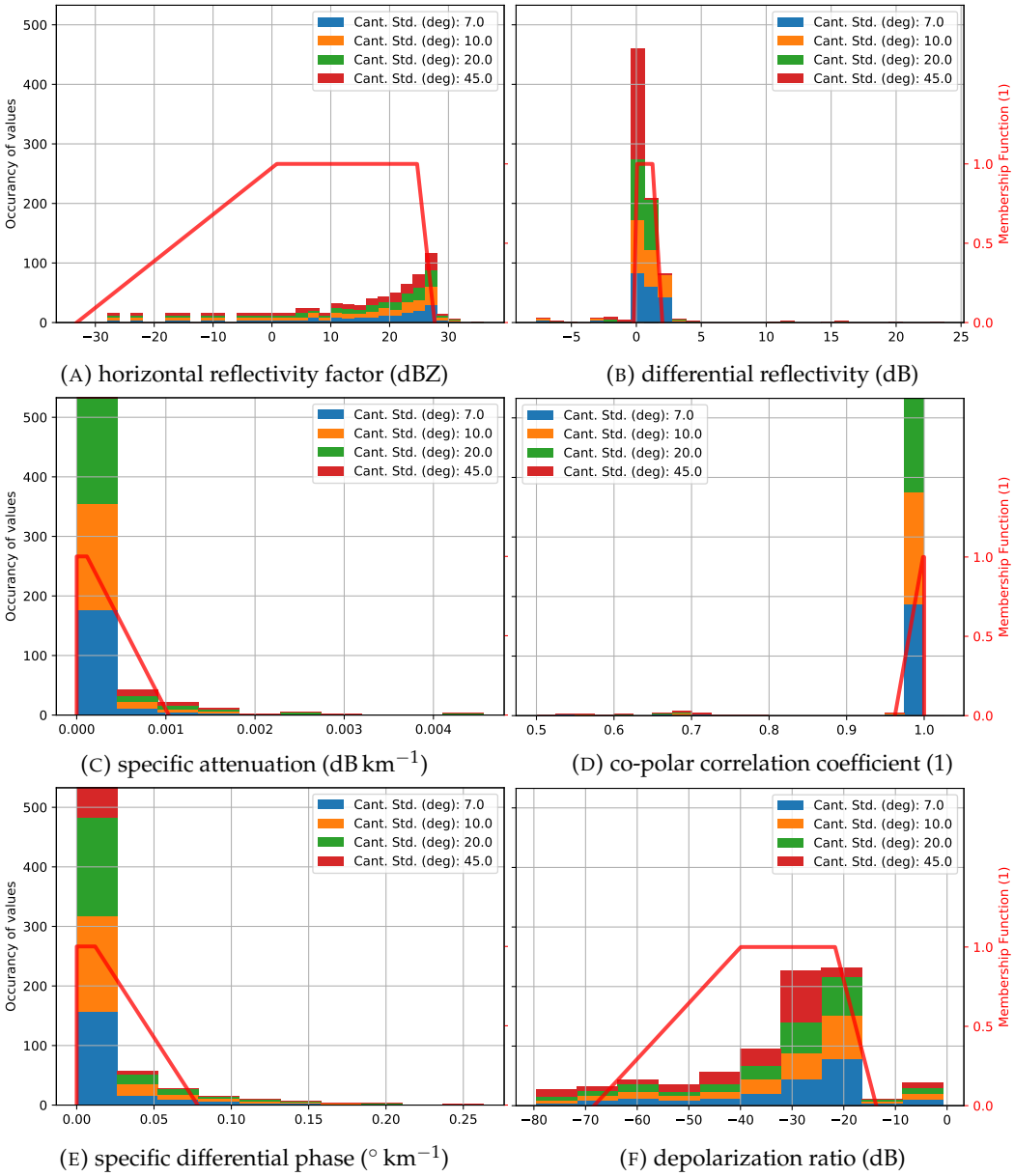

(A) horizontal reflectivity factor (dBZ)

(B) differential reflectivity (dB)

(C) specific attenuation (dB km^{-1})

(D) co-polar correlation coefficient (1)

(E) specific differential phase (° km^{-1})

(F) depolarization ratio (dB)

FIGURE 4.13: Same as Figure 4.7, but for rain.

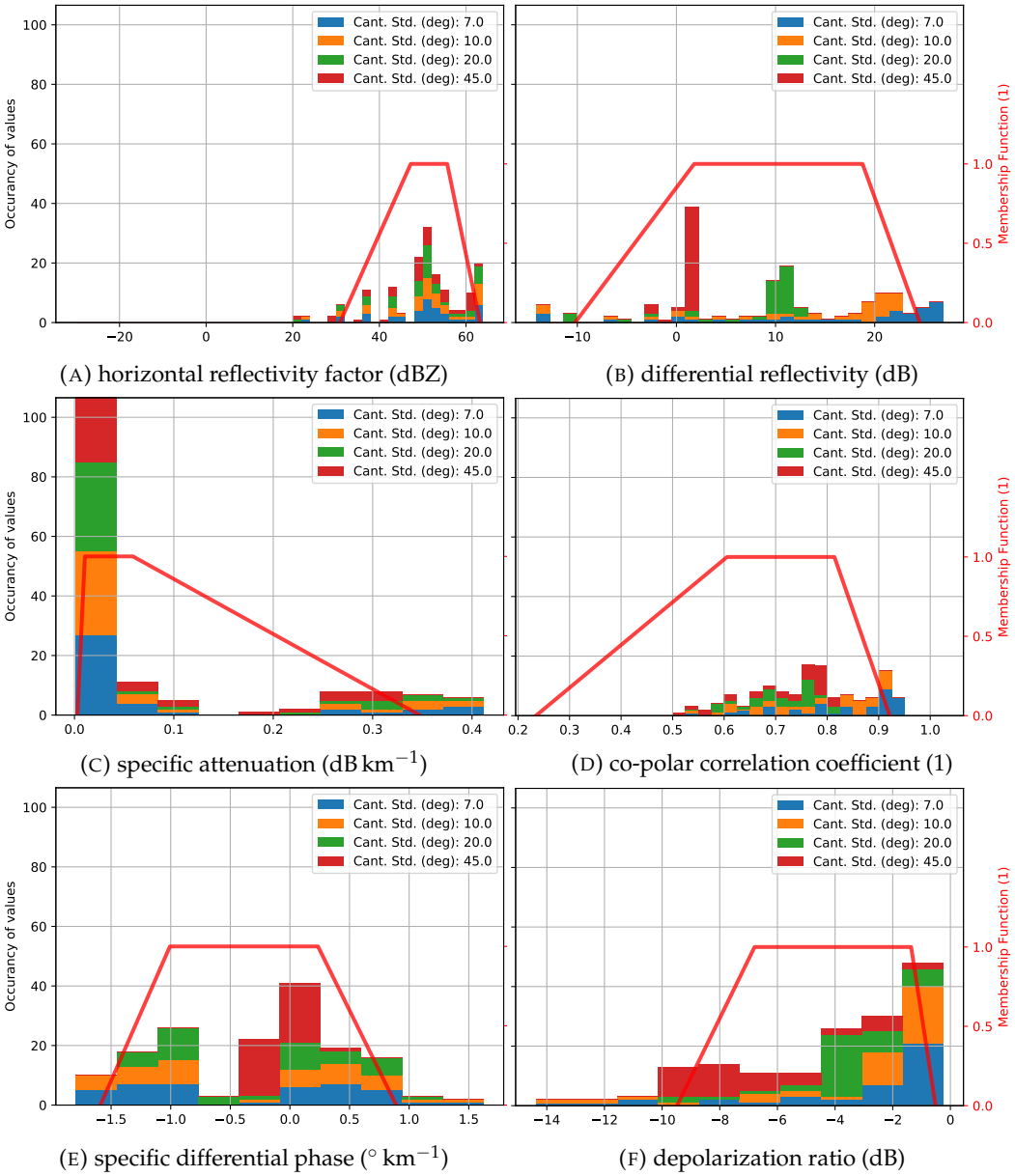

(A) horizontal reflectivity factor (dBZ)

(B) differential reflectivity (dB)

(C) specific attenuation (dB km^{-1})

(D) co-polar correlation coefficient (1)

(E) specific differential phase (° km^{-1})

(F) depolarization ratio (dB)

FIGURE 4.14: Same as Figure 4.7, but for big drops.

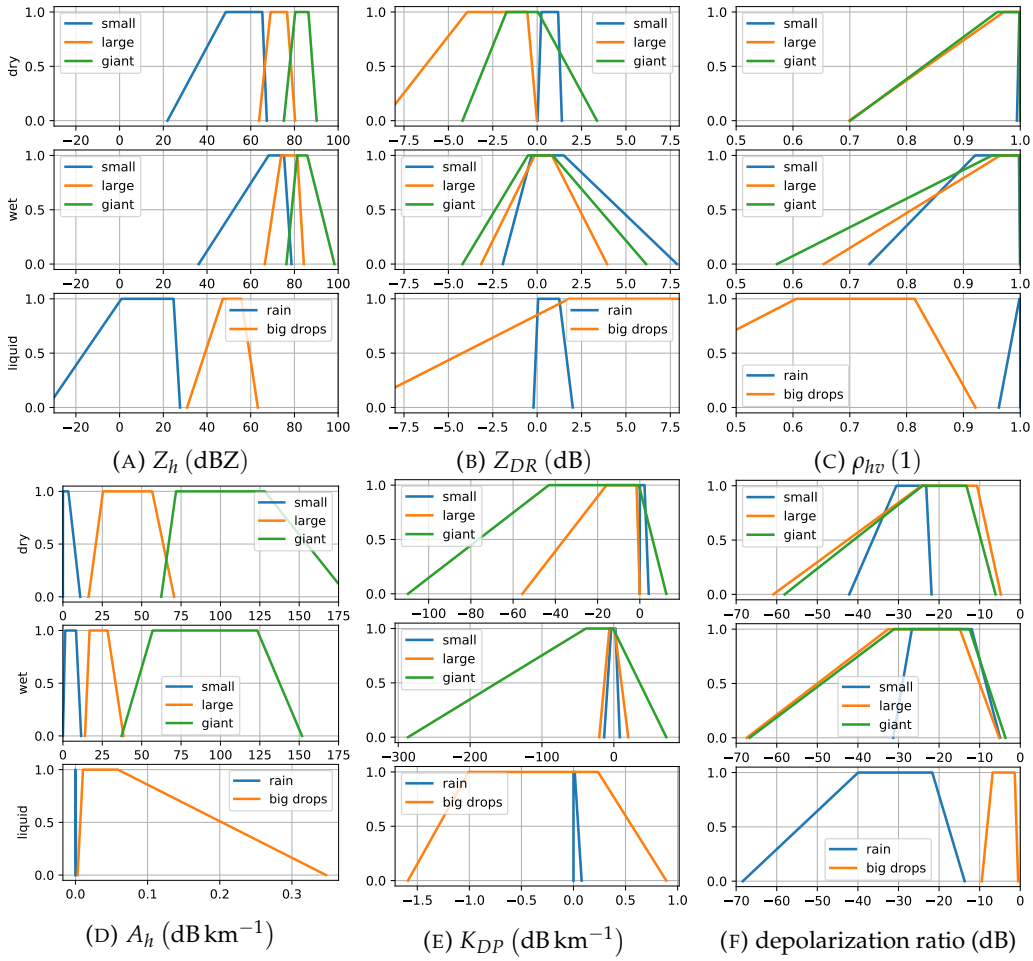

(A) Z_h (dBZ) (B) Z_{DR} (dB) (C) ρ_{hv} (1)

(D) A_h $(\mathrm{dB\,km^{-1}})$ (E) K_{DP} $(\mathrm{dB\,km^{-1}})$ (F) depolarization ratio (dB)

FIGURE 4.15: Membership functions for polarimetric variables for small, large and giant hail (dry and wet) and liquid precipitation (rain and big drops) as obtained from the simulations by using 5, 25, 75 and 95 percentiles as parameters for the trapezoid. Please note the different plotting ranges for A_h and K_{DP} between hail and liquid precipitation categories.

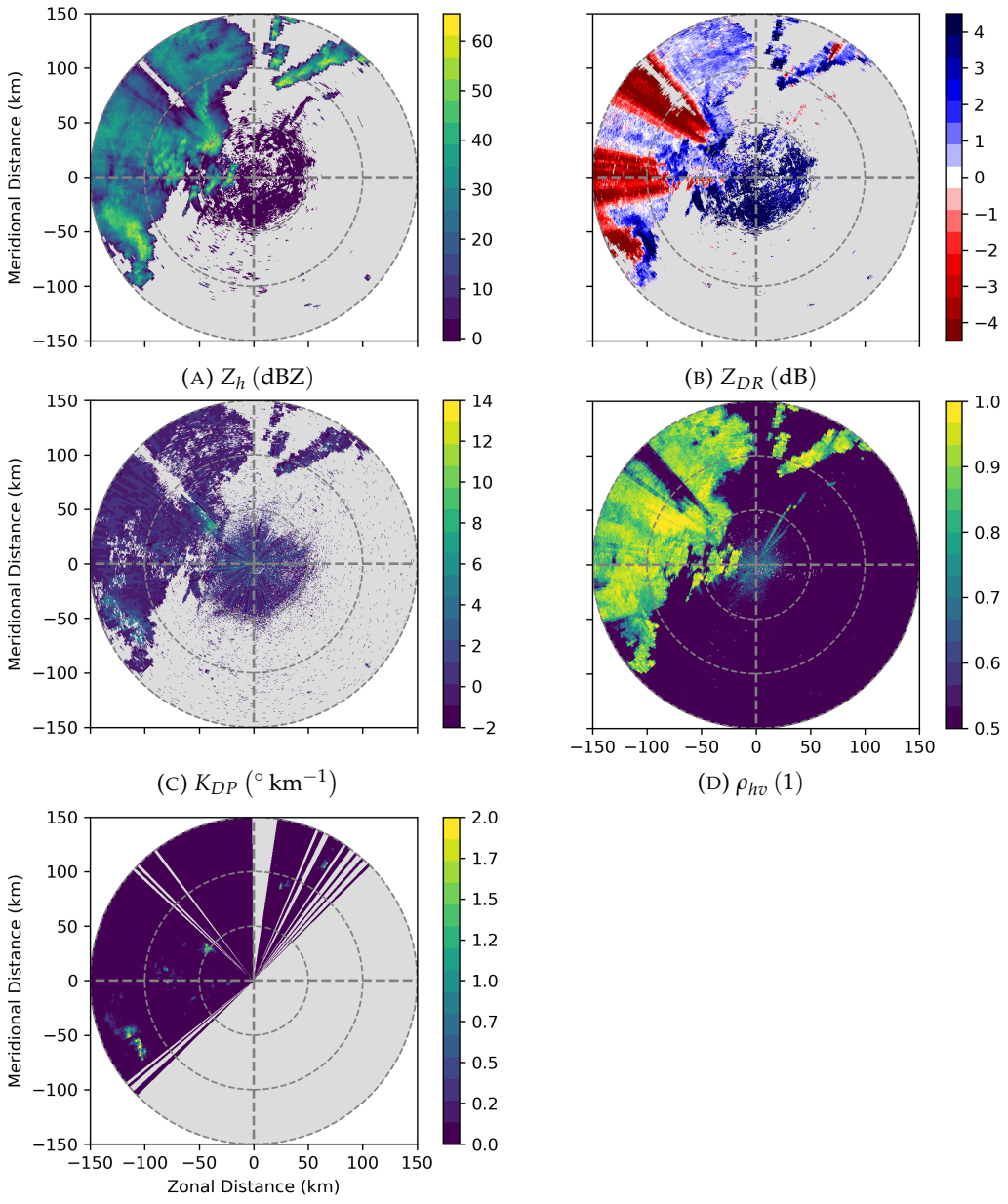

(A) Z_h (dBZ)

(B) Z_{DR} (dB)

(C) K_{DP} $(^\circ\,\mathrm{km}^{-1})$

(D) ρ_{hv} (1)

(E) A_h $(\mathrm{dB\,km}^{-1})$

FIGURE 4.16: PPIs of polarimetric variables horizontal reflectivity factor Z_h, differential reflectivity Z_{DR}, specific differential phase K_{DP}, co-polar correlation coefficient ρ_{hv} and specific attenuation A_h for a severe thunderstorm monitored by radar Essen on 23.06.2016 20:00 UTC.

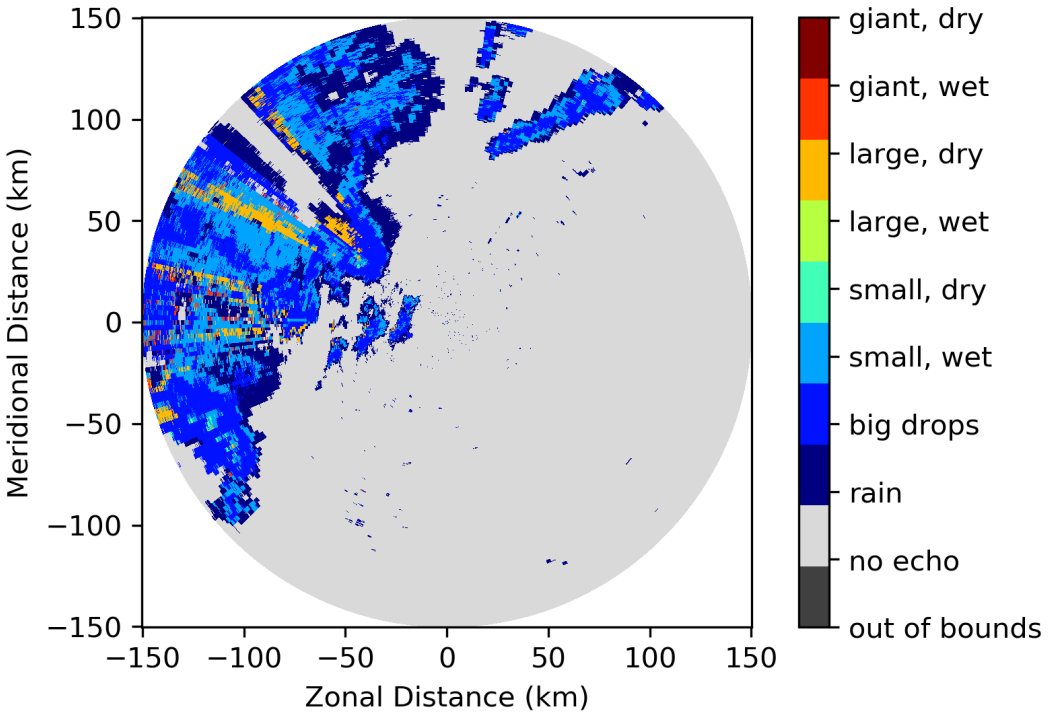

FIGURE 4.17: PPI of the adjusted fuzzy logic output using Z_h, Z_{DR} and ρ_{hv} as in Figure 4.16 with the same weighting as in Ortega et al. (2016).

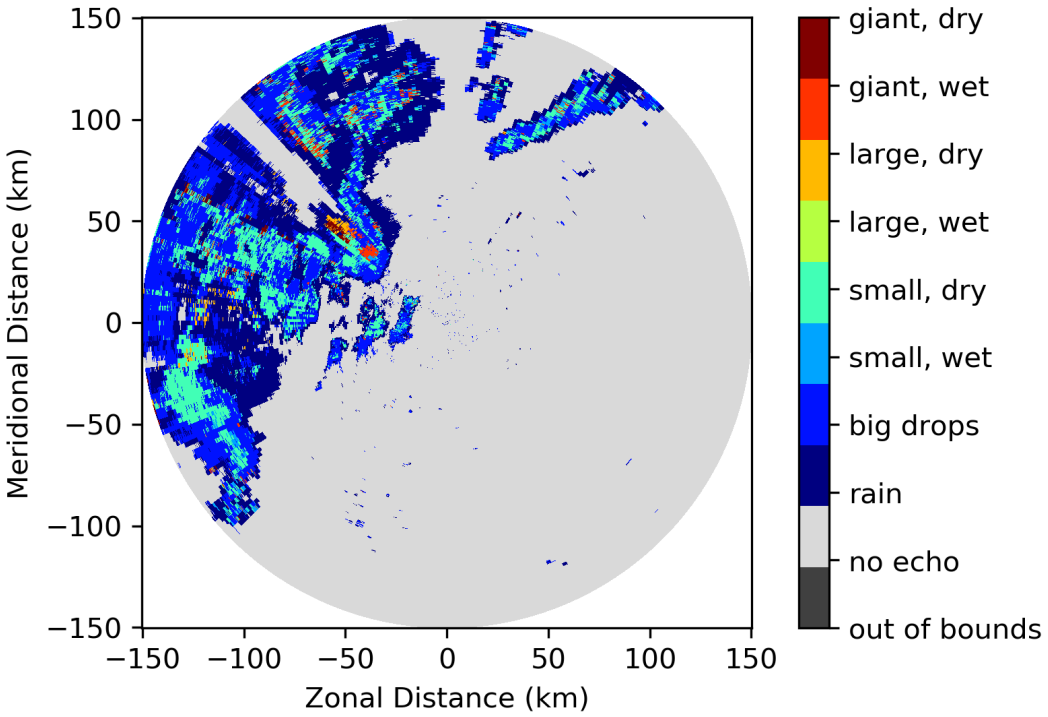

FIGURE 4.18: Like Figure 4.17, but with Z_h, Z_{DR}, ρ_{hv}, A_h and K_{DP}, weighting set to 1 and overlap penalty as is equation 4.4.

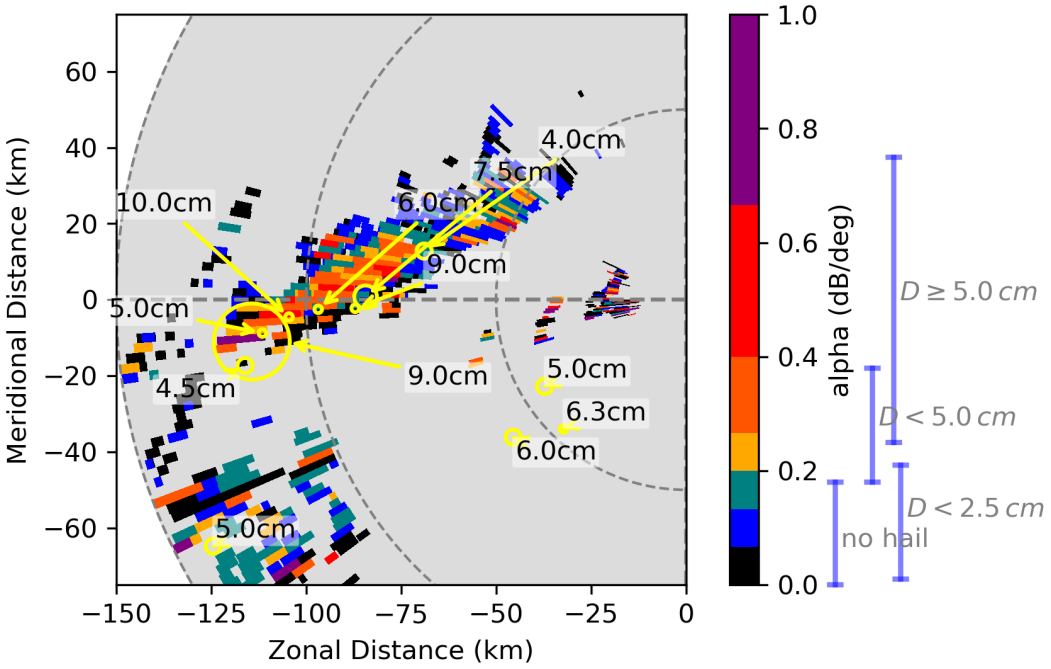

FIGURE 4.19: PPI of maximum attenuation coefficient α (colored area) and ESWD reports of maximum hail diameter on the ground (labels, yellow rings and arrows) occurring between 18:20 and 20:20 UTC on 23.06.2016 in vicinity of radar Essen. The yellow rings indicate the location uncertainty of the hail reports. Towards each ring, an arrow points with the maximum diameter written in the label attached. Next to the colorbar, the value range of α for three size categories according to Ryzhkov et al. (2013b) is given.

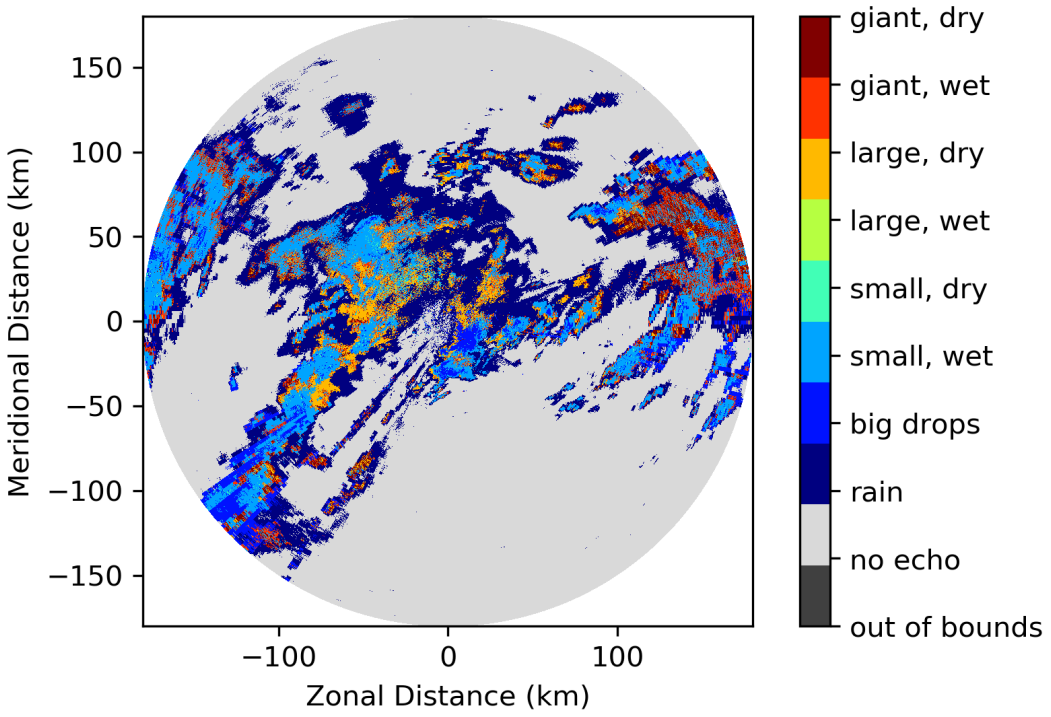

FIGURE 4.20: Like Figure 4.17, but for Alabama radar EEC on 22.01.2017 16:42 UTC.

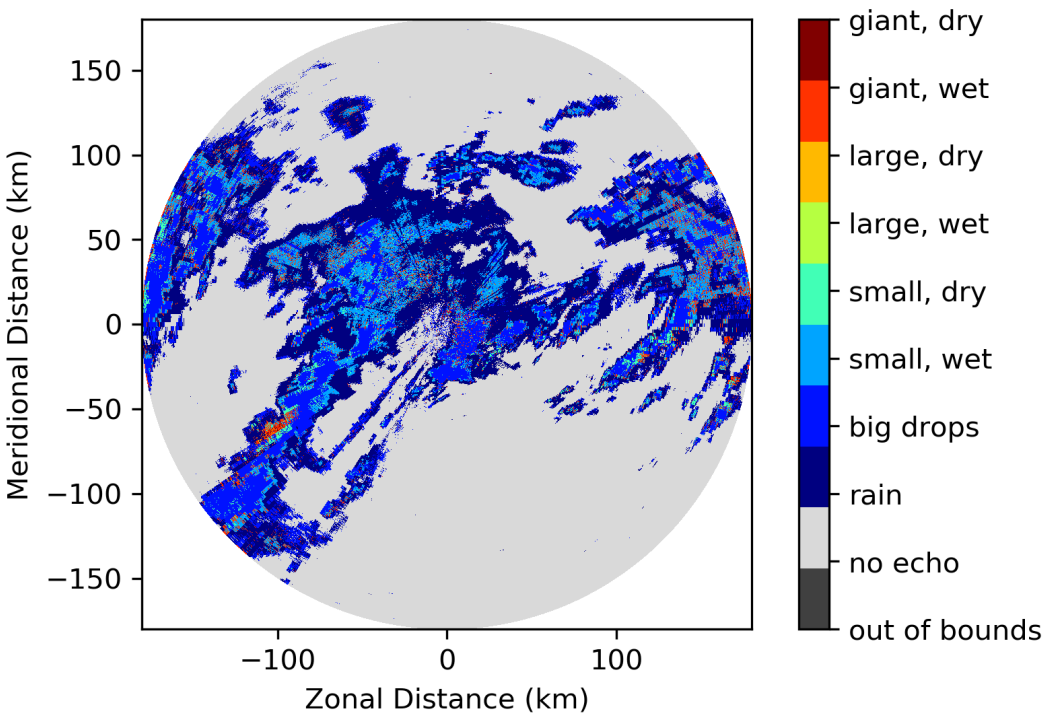

FIGURE 4.21: Like Figure 4.18, but for Alabama radar EEC on 22.01.017 16:42 UTC.

4.4 Unsupervised Clustering

Several attempts have been performed to modify the HSDA by Ortega et al. (2016) for application at C band, including the exchange of the membership functions, the use of other polarimetric variables and also weighting functions. Nevertheless, the results remain very sensitive to tiny changes in different polarimetric variables, e.g. Z_{DR} or ρ_{hv}. However, the hail size classes have not been modified, yet. Therefore, methods to find optimal classes, which allow robust hail size discrimination at C band, are elaborated in the following.

First the number of hail size classes were increased to have a finer size resolution for each, so that noise-induced class mismatch does not cause a difference of e.g. 2.5 cm (e.g. large to giant), but only e.g. 0.5 cm. Much finer classes were thought to make the error much smaller. These classes were calculated simulating polarimetric variables for each mm between 0.5 mm to 100 mm, as in section 4.3.2. The results were condensed into hydrometeor classes with 10 mm bin range. Although much more classes are available, overlapping of membership function increased and the application of the finer hydrometeor classes primarily yielded classes with the least overlap, which were not necessarily correct.

Instead of assigning a predefined hydrometeor class to each radar bin, the classes should be determined by similarity of polarimetric signatures. Grazioli et al. (2015) and Besic et al. (2016) suggest clustering of radar observations by data similarity and then in a second step compare the distributions of polarimetric moments for each cluster with scattering simulations. Therefore, the hydrometeor classes do not need to be defined beforehand, as "they are learned by the data" (Grazioli et al., 2015). This approach is assumed to reduce the sensitivity to tiny changes in polarimetric variables.

The difference between strictly setting classes and using similarity of signatures is illustrated in the two schematics in Figure 4.22. Some fictional measurement points are very close to each other, but are classified in different categories, if these are strictly applied (Figure 4.22a). Therefore, noise can cause the categories to change very quickly. The categories are more robust when they are selected by similarity of signals (Figure 4.22b).

To obtain unsupervised hydrometeor classes the hierarchical cluster merging approach is applied (Grazioli et al., 2015). Hereby, each data point starts with its own cluster and is merged with the most similar one, following a specific merging rule, until an "optimal" number of clusters n_c is reached. This number is selected using the "SD validity index" (Halkidi et al., 2002). This index attempts to maintain the least scattering between data points within a cluster, while having the highest distance between distinct clusters. The SD index is a weighted sum of the latter two

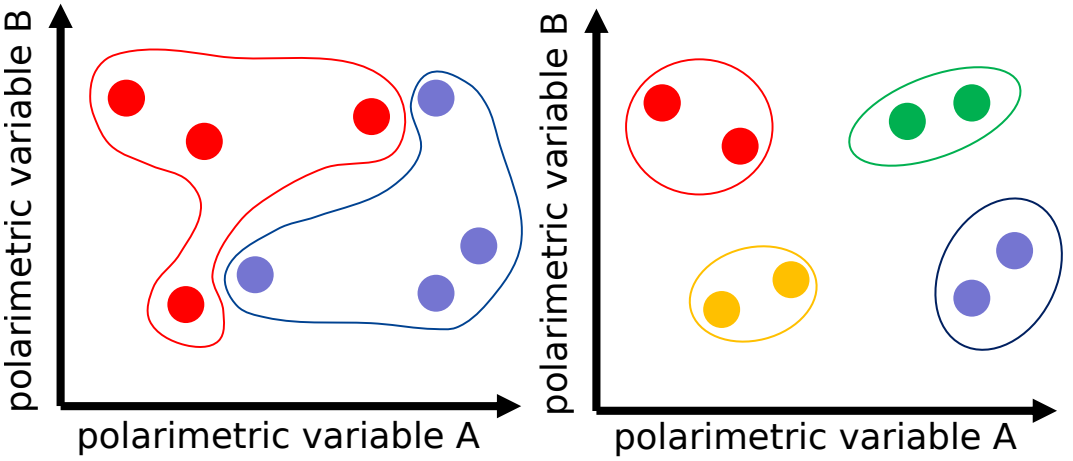

(A) Strict categories (B) Categories based on similarity

FIGURE 4.22: Schematics of two categorization approaches, where a) categories are strictly set and, where b) categories are selected by similarity of polarimetric variables. Different colors represent different categories. Each represents a fictional measurement of two polarimetric moments.

properties with

$$SD\left(n_c\right) = a \cdot Scatt\left(n_c\right) + Dist\left(\left(n_c\right)\right) , \tag{4.6}$$

$$Scatt\left(n_c\right) = \frac{1}{n_c} \sum_{L=1}^{n_c} \frac{\left\|\sigma\left(C_L\right)\right\|_2}{\left\|\sigma_{Data}\right\|_2} , \tag{4.7}$$

$$Dist\left(n_c\right) = \frac{D_{max}}{D_{min}} \sum_{L=1}^{n_c} \left(\sum_{M=1 \neq L}^{n_c} \left\|\overline{x}_{C_M} - \overline{x}_{C_L}\right\|_2 \right)^{-1} , \tag{4.8}$$

$$a = Dist\left(n_{Data}\right) , \tag{4.9}$$

(Halkidi et al., 2002; Grazioli et al., 2015) where n_{Data} is the number of data points, i.e. the maximal number of clusters, D_{max} (D_{min}) the maximum (minimum) distance between two clusters possible, $\sigma\left(C_L\right)$ the variance of the data in the Lth cluster C_L, $\sigma\left(C_{Data}\right)$ the variance of all data, $\overline{x}_{C_L}$ the weighted centroid of cluster C_L (see equation 4.11 below for calculation), and $\left\|\bullet\right\|_p$ the p-norm with $p = 2$, also known as euclidean norm, (Königsberger, 2013)

$$\left\|\boldsymbol{x}\right\|_p = \left(\sum_{i=1} \left|x_i\right|^p \right)^{1/p} . \tag{4.10}$$

Besides the p-norm, other metrices are also possible (see e.g. Grazioli et al., 2015).

Grazioli et al. (2015) introduce two merging rules, a weighted centroid distance WC and a weighted pairwise average distance WPA. The latter merging rule defines the distance between two clusters based on all points in both clusters. The former compares the weighted mass centers of the two clusters, where this center is the average position of all subclusters $C_K \subset C_L$ weighted by the number of data points

in each C_K, so that

$$\overline{\boldsymbol{x}}_{C_L} = \frac{1}{n_L} \sum_{C_K \subset C_L} n_K \left(\frac{1}{n_K} \sum_{\boldsymbol{x} \in C_K} \boldsymbol{x} \right) = \frac{1}{n_L} \sum_{\boldsymbol{x} \in C_K \subset C_L} \boldsymbol{x} \,, \tag{4.11}$$

(Grazioli et al., 2015) where $\boldsymbol{x}$ is an N-dimensional vector and N the number of (polarimetric) variables involved. For the following WPA is used as merging rule, the euclidean norm ($p = 2$) as metric and 8 variables from the scattering simulations (Z_h, Z_{DR}, A_h, K_{DP}, ρ_{hv}, the particle's outer temperature and its diameter) are used to obtain 8 unsupervised hydrometeor classes. Although the particle diameter is not available for radar measurements, it is used here to assist clustering. For each pair of unsupervised hydrometeor class and simulation variable a separate membership function exists. The membership functions are independent of each other. Therefore, the classification with radar measurements can be done without knowledge of the particle diameter.

The unsupervised clustering technique yielded 8 new hydrometeor categories, of which some contain scattering simulations of particles, which would have been different hydrometeor classes before. E.g. simulations of small, wet hail and big drops often populate the same categories. Although the classification is not that straightforward anymore, the result depicted in Figure 4.23 does not look random at all. On the contrary, cells and areas of stronger precipitation are set off from weaker precipitation (categories C and F, respectively). Attenuated areas are highlighted by category E, while hail suspected areas contain categories D and A. Nevertheless, the usability is certainly questionable as hail discrimination capabilities and warning categories have to be learned to interpret from fuzzy logic output. Therefore, it might be more efficient to decide directly upon the different polarimetric moments whether hail is present or not.

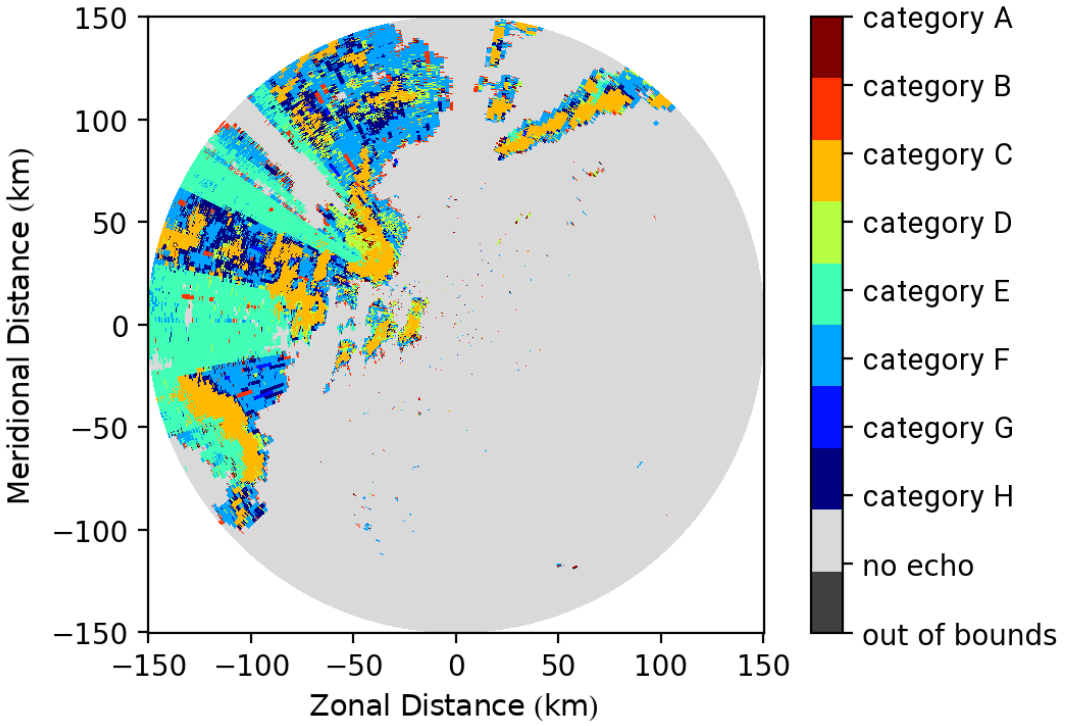

FIGURE 4.23: Like Figure 4.18, but using the membership functions of the unsupervised clustering approach. The different categories encompass particle types and are clustered by similarity of polarimetric signals.

4.5 Discussion and Recommendations

Methods to adjust a fuzzy logic based hail size discrimination algorithm (HSDA) have been investigated and applied. T-matrix scattering simulations have been used to obtain polarimetric variable distributions for hail of various sizes. The simulation of dual-layered particles showed plausible and consistent results compared with other published simulations and a single-layered simulation of dry hail. An adjusted hail size discrimination algorithm was obtained with membership functions calculated from scattering simulations. However, all further attempts to improve the adjusted algorithm, besides conceptualizing a dynamic weighting technique based on overlapping membership functions, did not fulfill the expectations for a usable tool to detect hail and discriminate its size. In the following a discussion of the approaches undertaken to obtain a HSDA at C band and a non-exhaustive list of suggestions for further improvements are given.

Particle scattering simulations and membership functions were only done at C band. However, repeating the simulations at S band for a comparison and consistency check with Ortega et al. (2016) would be interesting. Moreover, the simulation results were taken as they are and used to build the membership functions. However, some preprocessing and masking seems to be appropriate, e.g. removing negative α values.

One attempt made to improve the simulation results is to use the results in logarithmic scale, e.g. for K_{DP} and relations like $10\log_{10}(1-\rho_{hv})$, as most differences

did not show up in linear scale. However, these attempts did not improve the later hail size discrimination.

Park et al. (2009) and Ortega et al. (2016) partially used two-dimensional membership functions with a dependency on Z_h. In the framework of this thesis, such an approach has not been pursued, as membership functions were directly derived from scattering simulations. The simulation results were investigated for dependencies between two polarimetric variables, e.g. Z_h, K_{DP}, and hail diameter, but none were found. Furthermore, since uncertainties may remain after correction of anomalously high attenuation at C band, two-dimensional membership functions including Z_h have been avoided.

Simulated rain drops had standard deviations of their canting angle distribution up to 40°, which might not be realistic for rain at all. E.g. Ryzhkov et al. (2010) assume 10°. This large effect of turbulence on the rain drops might be possible, but rare. On the other hand, big drops with lower standard deviations (e.g. 7°) of their canting angle distribution exceeded 25 dB in Z_{DR}, which is also unexpected.

The scattering simulations were conducted with single particles only, which has a non-negligible effect on number concentration dependent polarimetric variables. E.g. K_{DP} for rain-drops was too low to be observed in measurements. With proper drop size distributions more realistic values could have been obtained. E.g. Ryzhkov et al. (2010) use the Hebrew University of Jerusalem cloud model to obtain drop size distributions for rain, ice crystals and hail, with maximum diameters of up to 6.8 cm for hail.

A strong effect of the water coat thickness on K_{DP} was shown (see Figure 4.6). Thinner water coats seemed to cause less fluctuation. Therefore, further investigation on scattering results with different water coats could improve results.

Although it is assumed that hail is more solid with increasing size (Prodi, 1970; Ryzhkov et al., 2013a), density variations might enhance simulation results. No density variations were included in the final particle simulations. Thus, more realistic polarimetric signatures might be retrievable if the simulation included these features.

Besides hail, no smaller frozen particles, e.g. ice and snow, have been properly considered in the simulations. Thus, if applied to height levels above the melting layer, the modified HSDA probably shows unreliable results. Within this thesis, analyses have been mostly restricted to summer cases and measurements below the melting layer.

Dielectric constants for the scattering simulation have been calculated following Cole and Cole (1941) and Zhang (2016). However, these formulas are not recommended for ice as the so called Kramers-Kronig-relations (see e.g. Lucarini et al., 2005) are not fulfilled (Blahak, 2016). Therefore, dielectric constants for future scattering simulations of ice should be done using a model, which fulfills the Kramers-Kronig-relations, such as Warren (1984).

Circular depolarization ratio CDR and its proxy depolarization ratio DR (Ryzhkov et al., 2017) are discussed to be effective at hail detection. First of all, LDR was not available, therefore no DR could be calculated. Second, during all cases K_{DP} was enhanced and made CDR or DR less usable (Matrosov, 2004; Ryzhkov et al., 2014). Lastly, the simulation results presented here do not indicate an increased capability of DR in discriminating hail, except for estimating the axis-ratio.

Weighting the polarimetric variables by the amount of overlapping membership functions definitely improved the results of the adjusted fuzzy logic. Pronounced areas with hail seem to be plausible in comparison with ground reports, attenuation and S-band data classification. Nevertheless, the output is still noisy and might benefit from smoothing. As the output closer to the radar appears to be more noisy, smoothing alone might not be enough to make the fuzzy logic output more robust and reliable.

The attenuation coefficient α was endorsed to be a proxy for hail size. This seems to be plausible in comparison with hail reports and scattering simulations. Therefore, the output of the adjusted HSDA was filtered by $\alpha \geq 0.1\,\mathrm{dB}/^{\circ}$ to reduce falsely classified hail due to noise. Even though an improved hail detection and distinction from areas with only big drops and rain was achieved, the results inside areas with enhanced α tended to overestimate and forfeit small hail at all.

The three hail size categories (small, large and giant) might be useful for warnings, but they appear to have too similar polarimetic variables to allow a precise distinction between hail diameters of 2.0 cm to 3.0 cm. Changing the classes by increasing the number of classes and having more narrow diameter ranges did not resolve the problem of misclassification. The approach to have finer classes or at least different classes might still be useful and should be investigated further. However, after using finer size classes, hail with diameters below 2.5 cm was not detected anymore, for reasons yet unknown.

To avoid overlapping and too close membership functions completely, hydrometeor classes were rearranged using unsupervised clustering to obtain a more robust classification. The approach enabled insights on how similar hydrometeors can appear in polarimetric radar data, but did not improve hydrometeor classification in this study. Still, future investigation might be worthwhile as e.g. Besic et al. (2016) show good results with their semi-supervised approach.

Modern machine learning interfaces and frameworks like Tensorflow and Keras allow for so called *DeepLearning*, which allows an algorithm to learn from input data until desired output is obtained (Abadi et al., 2015; Chollet et al., 2015). Instead of using simulated polarimetric signals, observational radar data could also be used in unsupervised learning approaches. Although this was not applied to the unsupervised clustering, a machine learning technique, so called variational auto-encoders (Davidson et al., 2018), was employed to compress the input of all measured polarimetric variables into relevant information. Hereby, the input data is compressed into a simpler representation, from which the neural network can reconstruct the original

data. This essentially filters out dependent and redundant information. However, the attempts made did not turn up significant improvements worth noting. Nevertheless, other machine learning approaches or preprocessing input data before using variational auto-encoders might succeed.

The 1D hail growth and melting model HAILCAST (Adams-Selin and Ziegler, 2016) was applied to numerical weather model analysis data with the aim to evaluate the adapted HSDA output at every point within radar range. However, the resulting maximum hail diameters underestimated the ground reports of the ESWD in all cases. Most likely the storms were not properly represented in the used numerical weather analysis. E.g., a misplacement of the storm or a too weak convection are possible problems (Brewster, 2003; Keil and Craig, 2007). Also, the updraft might have been stronger and more concise than the representation in the model due to too coarse model resolution.

Chapter 5

Dynamics, Precursors and Nowcasting

Hail growth is a dynamic process, difficult to observe and despite several key dependencies for optimal hail growth have been identified (Dennis and Kumjian, 2017), it is still an ongoing research topic (e.g. Adams-Selin and Heymsfield, 2019; Kumjian et al., 2019; Labriola et al., 2019; Kumjian and Lombardo, 2020). Large hail can cause severe damage and current nowcasting schemes do not predict hail growth, but advect hail-bearing storms based on their previous tracks (Hering et al., 2004).

Candidates for precursors of hail are investigated to improve lead times of nowcasting hail and detect hail growth as early as possible. Several studies proposed the intensification of vertical columns of enhanced differential reflectivity, so-called Z_{DR}-columns, as hail precursors (Kumjian et al., 2014; Snyder et al., 2015). E.g. simulations by Kumjian et al. (2014) resulted in peak Z_{DR}-column heights occurring between 12.5 and 15 minutes before peaks of maximal hail mass at the surface. However, most studies primarily use spectral bin microphysical models to investigate Z_{DR}-columns as precursors for hail.

In this chapter, hail growth and occurrence are analyzed based on observed polarimetric radar and surface observations by comparing time series of Z_{DR}-columns, their intensity and extent with observed hail occurrence and size detected at the ground. Data of a polarimetric C-band radar network and hail reports from the European Severe Weather Database (ESWD) are analyzed with the help of a custom made cell tracker, an attenuation correction algorithm (see chapter 3), and a Z_{DR}-column detector.

5.1 Techniques Applied for the Investigation of Hailstorms

A storm relative observation throughout time is designated to investigate and analyze the dynamics of convective cells and precursors of hail. Tools and techniques employed to process the radar data are introduced in this section.

5.1.1 Z_{DR}-column detection

Vertical columns of enhanced differential reflectivity Z_{DR}, so-called Z_{DR}-columns, repeatedly identified in polarimetric radar data (Wakimoto and Bringi, 1988; Picca et al., 2010; Kumjian et al., 2012; Snyder et al., 2015; Ryzhkov et al., 2017; Trömel et al., 2017; Witt et al., 2018, ...), signal large, and thus oblate drops lifted by sufficiently strong updrafts beyond the 0 °C isotherm. Thus, Z_{DR}-columns indicate strong updrafts within convective cells, which are necessary for hail generation and growth. Comprehensive information on the physics and detection of Z_{DR}-columns can be found in Kumjian et al. (2014).

So-called Range Height Indicator (RHI) scans with sweeping elevation at constant azimuth allow observation of Z_{DR}-columns at high resolution (see e.g. Trömel et al., 2017, Figure 2). Since no RHI scans are available for the DWD's network, the analysis is based on synthetic RHIs, reconstructed from the PPIs constituting a volume scan. This results in a reduced vertical resolution compared to genuine RHIs and temporal lags between the elevations of up to 4 min. The reduced vertical resolution (see available elevations in Table 2.1) is counteracted by linear interpolation in the vertical in order to allow for Z_{DR}-column detection also at far ranges and to better quantify the height of the Z_{DR}-columns. The linear interpolation virtually increases the available elevations from 10 to 30.

The detection of Z_{DR}-columns follows Snyder et al. (2015), who identify columns by counting up grid points along the vertical as long as $Z_{DR} \geq 1$ dB, starting at the 0 °C isotherm. The following modifications are applied. Due to the time lag between elevations, Z_{DR}-columns can be skewed, thus the modified algorithm accounts for advection effects between two elevations. The Z_{DR}-threshold of 1 dB mostly used at S band (Kumjian et al., 2014) is increased to 2 dB, which according to scattering simulations is more suitable at C band, to clearly distinguish between liquid and frozen particles. The height of the 0 °C isotherm is derived from spatially interpolated radio sounding data (kindly provided by the University of Wyoming Department of Atmospheric Science[1]), which are *in-situ* measurements, and not from model predictions.

5.1.2 Attenuation as primary hail fall indicator

In hail bearing storms strong attenuation can often be observed at C band. Figure 5.1 shows PPIs of the horizontal reflectivity factor for four time steps separated by 15 minutes. A prominent storm cell with reflectivity values reaching 60 dBZ generates a "shadow" of strong attenuation at an azimuth moving from about 280° to 310° when the cell moves past the radar.

According to T-matrix scattering simulations of specific attenuation, attenuation at C band of $\approx$ 50 dB is highly unlikely to be caused by rain only (see Figure 5.2). Concentration also affects the strength of attenuation. However, considering the

[1] http://weather.uwyo.edu/upperair/sounding.html

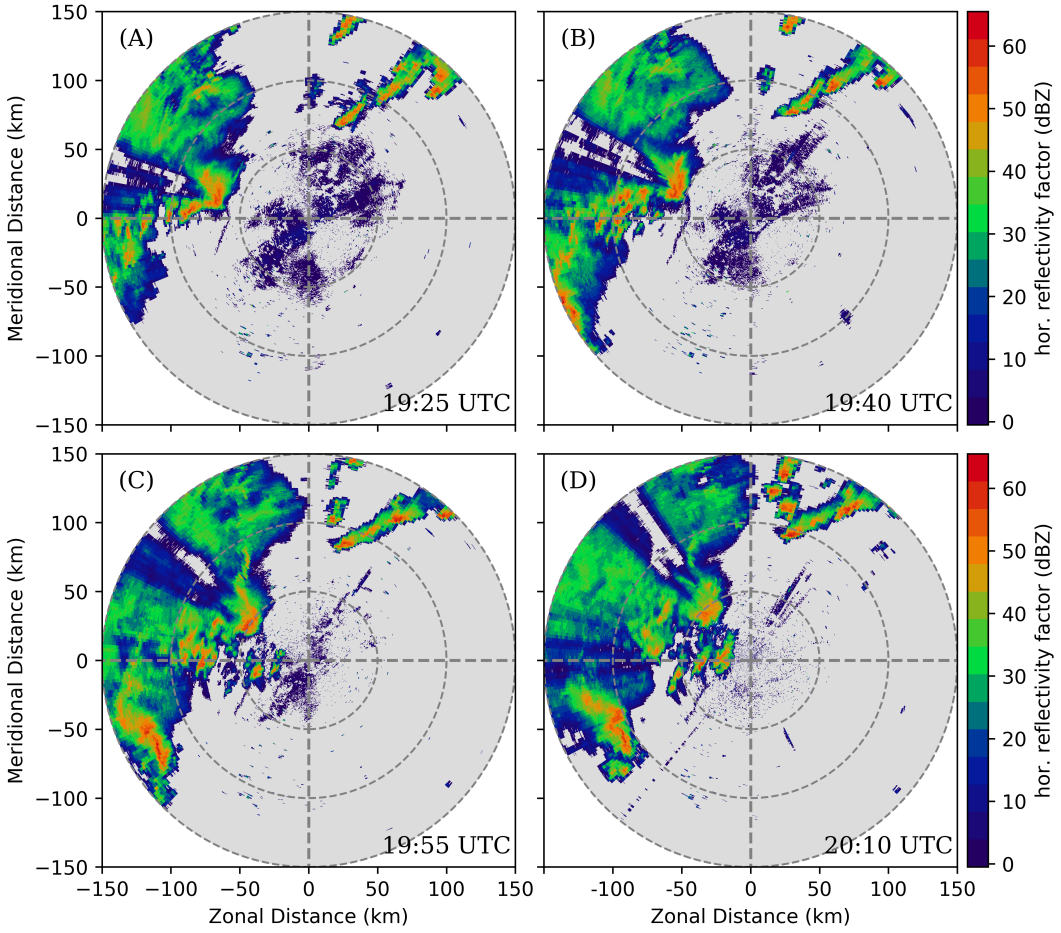

FIGURE 5.1: Plan Position Indicators (PPIs) of the horizontal reflectivity factor Z_H measured by the precipitation scan of C-band radar in Essen on 23.06.2016 at 19:25, 19:40, 19:55 and 20:10 UTC, showing a storm cell with strong attenuation at 280°, 290°, 300° and 310° azimuth angle respectively at about 50 km range.

magnitude of the specific attenuation and the confined width of the hail core, it is much more likely, that in the case shown in Figure 5.1 the attenuation was dominated by a few, larger particles with diameters e.g. $\geq$ 25 mm. Such diameters are usually reached only by hail particles. Observed hail with diameters beyond 5 cm and up to 9 cm between 18:10 UTC and 21:15 UTC support this finding (see data stored online in the European Severe Weather Database (ESWD)).

Strong attenuation at C band is likely related to hail in the radar beam, especially since hail shafts, e.g. in so-called hot spots, are spatially confined (Vulpiani et al., 2008; Tabary et al., 2009; Ryzhkov et al., 2013b). Specific attenuation (attenuation per length unit) A_h is not directly observed by radars, and sufficiently accurate estimates can be problematic in hail. To ameliorate this problem the analysis (and detection methodology) is confined to the temporal behavior of the attenuation coefficient α (dB/deg). While strong precipitation of rain can also cause significant attenuation at C band (Borowska et al., 2011), enhanced values of α are only possible in the presence of large and giant hail (Ryzhkov et al., 2013b). Therefore, a sudden increase in α indicates hail fall. An estimate of α is derived from the attenuation

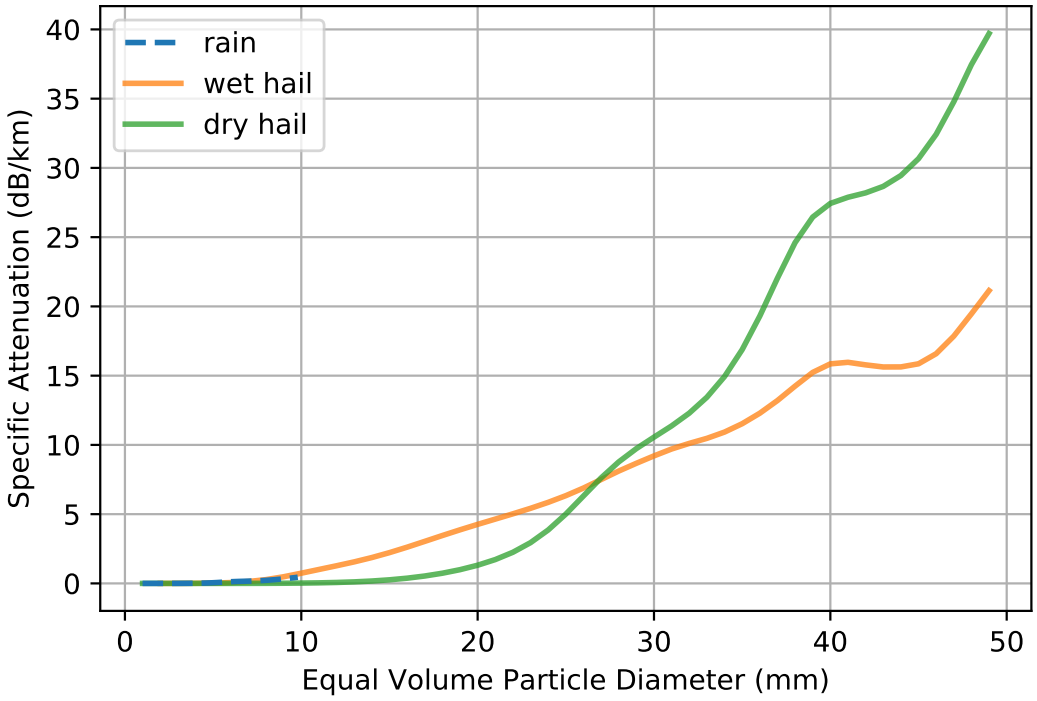

FIGURE 5.2: T-matrix scattering simulation of specific attenuation for liquid particles ("rain"), water coated ice particles ("wet hail") and ice particles ("dry hail"). For each 0.1 mm diameter step, a single particle is simulated, i.e. the particle concentration is $1\,\mathrm{mm}^{-1}\,\mathrm{m}^{-3}$, to keep the results normalized. The dieletric constants for water and ice are calculated for 0 °C following Cole and Cole (1941) and Zhang (2016) and the axis-ratio of the simulated, oblate ellipsoid is 0.75 for all diameters (to be in line with Depue et al., 2007). The standard deviation of the canting angle distribution is 10° for rain and 40° for hail. The FORTRAN code for the simulations is the same as used in Ryzhkov et al. (2010).

correction in hail following the methodology introduced in chapter 3.

5.1.3 Tracking of convective cells

In order to observe the evolution of Z_{DR}-columns in time, the encompassing storm cells need to be tracked first. Cells are tracked by first detecting cells in each time step and then finding matching cells in consecutive time steps. The cell detection uses 40 dBZ contour lines of a regridded 2D reflectivity factor field of the precipitation scan. The grid is Cartesian and has a resolution of 250 m, which is equal to the radial resolution of the precipitation scan. It is centered on the geometric location of the radar site.

For each possible pair-wise combination of cells in two consecutive time steps a similarity ς between cell-pairs is calculated. The index expresses the likelihood that a cell A at the time step t is the successor of a cell B at time step $t-1$. The calculation of ς consists of three components:

1. Pearson's correlation coefficient,
2. geometric distance and

3. perimeter difference.

Pearson's correlation coefficient is calculated between the coordinate vectors of the contours of the cell pairs on a Cartesian plane. Prior to the computation, each contour is approximated by a fixed amount of coordinate points to allow the calculation of Pearson's correlation coefficient. Here 35 points were used, as this was the average number most contours had already. The geometric distance between two cells composing a pair is calculated between the centers of each contour, which are obtained using the arithmetic average. The distances for all possible pairs are scaled to values between -1 and 1. -1 is the maximum, 0 the median and 1 the minimum distance. The perimeter of a cell is calculated by summing the distances between consecutive coordinate points of this cell's contour. Perimeter differences between two cells are scaled between 0 (maximum perimeter difference) and 1 (identical perimeters). The similarity ς of a cell pair is the sum of the three components (Pearson's correlation coefficient, geometric distance and perimeter difference) weighted by 1, 4, and 2, respectively, and is calculated for each possible pair of cells in consecutive time steps.

Pairs with the highest ς are matched and all pairs involving either of those cells are removed from the pool of pairs. This procedure is repeated for the remaining pairs until no more cell pairs with $\varsigma \geq 0.3$ are in the pool. This cut-off value has been chosen based on a sensitivity analysis of the here proposed tracker. For other data this value might require modification. Each pair of matched cells is interpreted as one identical cell of two consecutive time steps. If no consecutive cell is identified, the respective cell is assumed to have terminated. Remaining cells in the new time step are newly initiated cells.

According to subjective validation (manual tracking by eye) of the methodology, long living cells are tracked correctly, while short living (less than 20 min) and smaller cells (less than 9 grid cells) are not always matched correctly. In the following the analysis is based on long living cells.

For all tracked cells, polarimetric variables and derived quantities, like α and Z_{DR}-column properties, are assigned to the cells. This allows for a cell-relative analysis of e.g. Z_{DR}-column evolution. Additionally, hail reports from the ESWD are assigned to the tracked cells if they coincide in space and time. I.e. for any time step t within the cell's lifetime, the reported geographic location of the hail has to be inside the cell's contour at time step t and t has to be inside the reported time window.

5.2 Investigating Convective Cells for Hail Precursors

Based on the data described in chapter 2 and the tools above, in total 16 events with predominantly convective cells are investigated. The events were selected by searching the ESWD for severe, hail-bearing storms within the coverage of the DWD radar network. The analyzed time period was limited since radars with polarimetry upgrade first became available throughout 2013. From 54 initially selected severe

hail-bearing events, only 16 remained due to quality filtering of reports, hail occurrence in radar vicinity and available polarimetric radars.

5.2.1 Example events of severe, hail-bearing thunderstorms

Three of the selected 16 events are illustrated and discussed here briefly. On June 24, 2016 a convergence line initiated, among numerous, smaller convective cells, at least one supercell[2]. Severe hail damage by hail reaching 9 cm in diameter close to Reutlingen, Germany was reported[3]. The time series of Z_{DR}-column height above the melting layer and attenuation coefficient α for a hail-bearing cell, which moved across the reported hail location, are displayed in Figure 5.3 and 5.4, respectively. Between 18:45 UTC and 19:20 UTC the attenuation was most intense. During this time the hail shaft moved between radar and updraft location, impairing the Z_{DR}-column observation. Both time series occasionally show spikes. Their occurrences between Z_{DR}-column height and α seem to correlate with a time lag. E.g. at 18:40 UTC the Z_{DR}-column height suddenly increases 15 min to 45 min before hail is reported at the ground. About 15 min after the Z_{DR}-column spike an increase of α is observed as well, which coincides with the hail report at the ground. In this and also the following time series, the Z_{DR}-column height mostly peaks before the column collapses, and high α-values are observed which coincide with hail reports at the ground. This behavior fits the concept of hail development (e.g. Kennedy et al., 2001; Kumjian et al., 2014), which requires strong updrafts signaled by the increasing Z_{DR}-columns.

A tornadic event was observed by the radar Flechtberg on May 13, 2015. On this day a coldfront caused thunderstorms and in particular supercells to move towards the Black Forest and the Swabian Mountains, causing severe damage by hail with 5 cm diameter and two tornados[4]. The time series for a tracked cell moving across the location of issued hail reports are displayed in Figure 5.5 for Z_{DR}-column height and in Figure 5.6 for α. This cell exceeded 60 dBZ in reflectivity factor (not shown) and was consecutively tracked as a single cell for 3 h and 15 min. Although hot spots of other cells were very close and merging cannot be ruled out, supercells can live for more than 4 hours (Bunkers et al., 2006). Similar to the first example event, the time series of this cell shows fluctuations and spikes, which also coincide between the surface hail reports and the polarimetric observations. Z_{DR}-column height spikes precede attenuation spikes and ground reported hail between 10 min and 20 min.

Thunderstorms and a supercell coming from Belgium and crossing through the southern part of North Rhine-Westphalia caused severe damage on July 5, 2015. In and around Bonn reports of hail with diameters exceeding 7 cm were issued[5]. Radar

[2]Supercell thunderstorms have very well organized up- and down drafts, are mainly characterized by a single deep, rotating updraft and are associated with severe weather including giant hail (Browning, 1964; Cintineo and Stensrud, 2013; Kumjian and Ryzhkov, 2008).

[3]Source: https://www.youtube.com/watch?v=9khn4Srdhkw, last accessed on 09.12.2019 16:08UTC

[4]Source: https://www.skywarn.de/jahr-2015/13-mai, last accessed on 09.12.2019 17:53UTC

[5]Sources: https://www.youtube.com/watch?v=mEbYiOH46R0 and https://wetterkanal.kachelmannwetter.com/grosshagel-am-05-juli-rueckblick-und-bilder/, last accessed 09.12.2019 18:35UTC

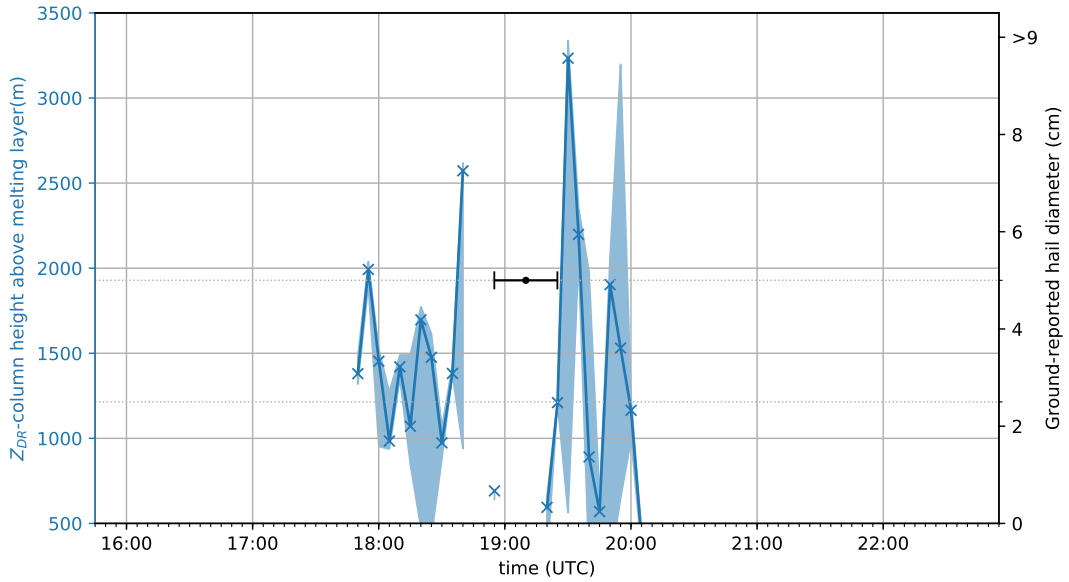

FIGURE 5.3: Height of Z_{DR}-columns above the melting layer for one tracked cell along the time observed by radar Türkheim on 24.06.2016. The temporal resolution is 5 min. The blue, solid lines with crosses show the median Z_{DR}-column height above the melting layer for a cell at each time step. The range between the minimum and maximum value in the cell is shown as colored area. Information from ground reports of the European Severe Weather Database (ESWD) are shown by black error bars (scale on the right axis). The dot in the center of the error bar represents the exact time on which the report mentions hail on the ground. The vertical pipes of the error bar indicate the error margin given with the report.

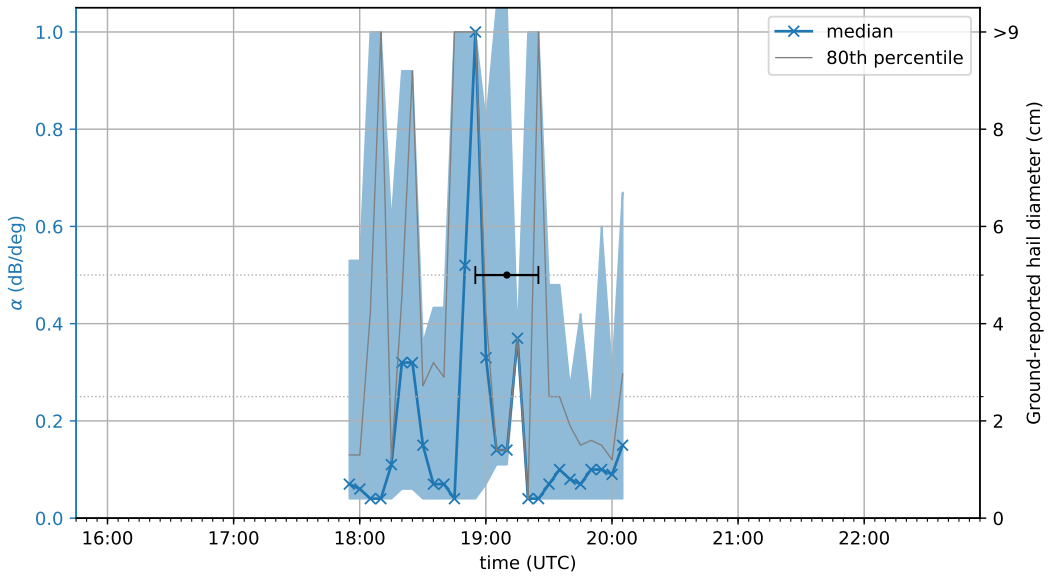

FIGURE 5.4: Like Figure 5.3, but for attenuation coefficient α. In gray the 80^{th} percentile is shown in addition to the median.

Essen observed multiple cells and the corresponding time series of Z_{DR}-column height above the melting layer and α are shown in Figure 5.7 and 5.8, respectively. Although multiple, tracked cells with shorter individual life times are shown, spikes are still visible. Attenuation intensified multiple times and hindered Z_{DR}-column detection in several time steps (14:00 - 14:20 (cell C, green), 14:55 - 15:05 (cell A, blue),

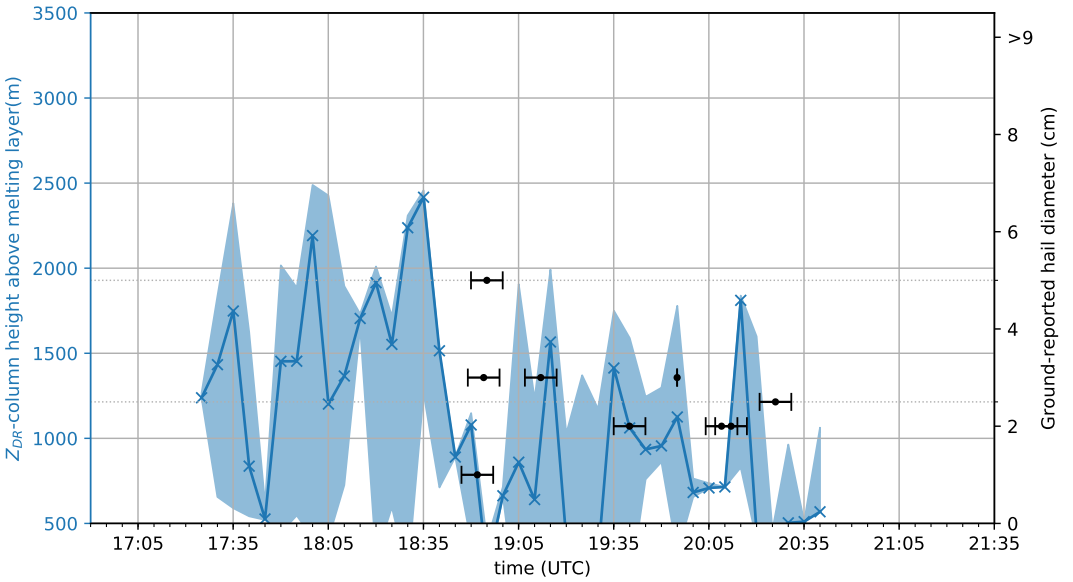

FIGURE 5.5: Like Figure 5.3, but for radar Flechtberg and observation on 13.05.2015. Only one cell is shown for better visibility.

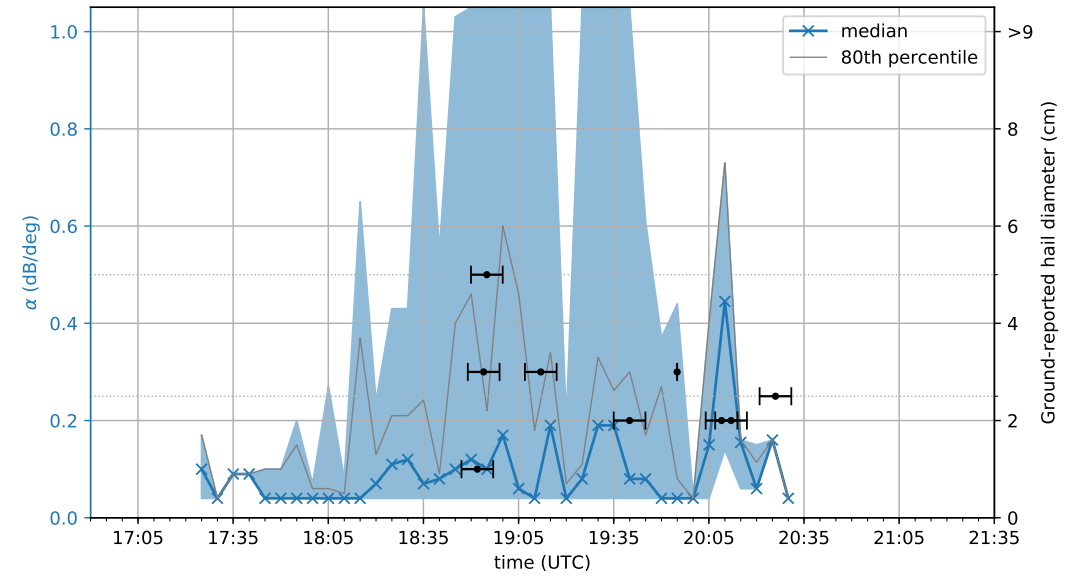

FIGURE 5.6: Like Figure 5.4, but for radar Flechtberg and observation on 13.05.2015. Only one cell is shown for better visibility.

15:20 - 15:30 and 15:55 - 16:30 (cell D, red), 16:50 - 17:15 (cell B, orange)). Most ground reports largely overlap with each other in time; thus it is more difficult to attribute them to individual spikes in all cases. E.g. the first report seems to relate to an α spike at 13:50 and a Z_{DR}-column height peak at 13:40. The ground reports of the two largest hail sizes (8.2 cm and 11 cm) can be related to α spikes at 16:25 and 16:45 and to Z_{DR}-column height peaks at 16:10 and 16:25, respectively. Thus, Z_{DR}-column height spikes precede hail reports also in this event by 10 min to 20 min.

The examples have shown that Z_{DR}-column height spikes precede attenuation spikes and ground reported hail. This might allow predicting hail before detection.

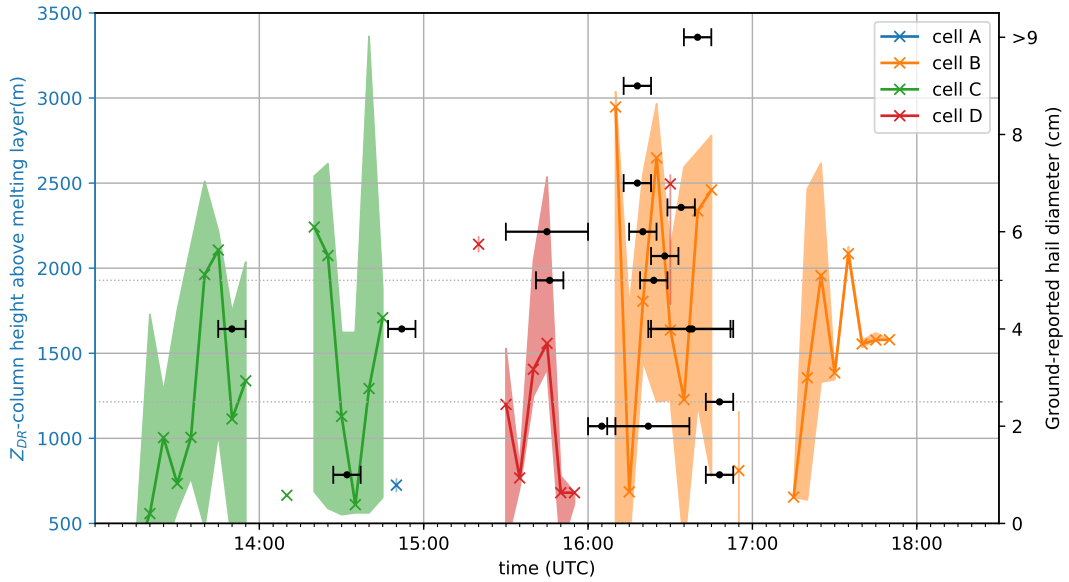

FIGURE 5.7: Like Figure 5.3, but for radar Essen and observation on 05.07.2015. Multiple convective cells are shown, each with a different color.

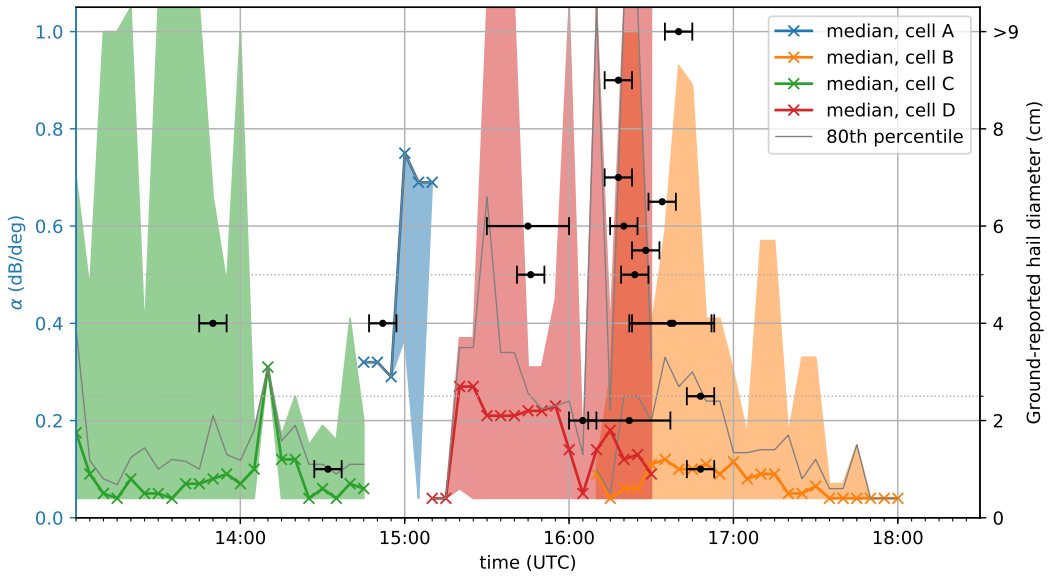

FIGURE 5.8: Like Figure 5.4, but for radar Essen and observation on 05.07.2015. Multiple convective cells are shown, each with a different color.

The time between the point in time when the prediction of hail is made, i.e. Z_{DR}-column height spike, and the detection of hail, i.e. attenuation spike, is defined as lead time. The following analysis investigates the question of how early hail can be predicted before detection.

5.2.2 Lead time statistics

The following criteria and rules are used for estimating lead times for all events. When reports have overlapping time windows the ones with lower hail sizes are

discarded, because the signal of larger hail probably blurs or even overrides the signal of smaller hail. If temporally overlapping reports indicate the same hail size, then the reports are only used if their time windows are not shifted, i.e. their time windows overlap entirely. Otherwise, finding the exact moment of hail fall, i.e. finding an attenuation spike matching to a hail report, can become ambiguous. Reports of the same hail occurrence from multiple observers are not discarded this way, as their time windows are not shifted.

From the 16 events, 5 had to be discarded for lead time analysis due to data quality (radar and/or ground reports) or ambiguity of reports. Events were discarded when there were no ground reports beneath areas with precipitation (reports were likely placed in the wrong area), or when the reports only occurred at the edge of the radar range. Unfortunately, one event with too many hail reports happening in a very short time in a very confined area had to be discarded due to ambiguity and severe attenuation. Another event (13.04.2016, radar Isen) was discarded due to extremely noisy Φ_{DP} and low ρ_{hv}, which rendered attenuation correction and Z_{DR}-column detection useless here. The remaining 11 events show good quality of radar data and reports.

The time windows of the ground reports typically extend from 15 min to 60 min, however, a more accurate timing is necessary to conduct an analysis on how early hail can be predicted. Hail causes significant attenuation at C band, as shown in section 5.1.2. Therefore, the timing of the α spikes is used to locate the time of impact on the ground within the time window of the report. Since hail takes less than 5 min to reach the ground, the timing of the α spikes is considered accurate enough. For every α spike within the time window attributed to a ground report of hail, a preceding peak in Z_{DR}-column height is searched for. The time interval between both peaks defines the lead time. The thus estimated lead times for the 11 severe hail events are listed in Table 5.1. Hail is categorized according to diameter into small (< 2.5 cm), large (≥ 2.5 cm and < 5 cm), and giant hail (≥ 5 cm). As the radar only allows for time steps of 5 min, the estimated lead times can only have the discrete and integer values of e.g. 10, 15 or 20 min. Figure 5.9 visualizes the range of estimated lead times against hail diameter/category. According to the estimation, a 20 min lead time is most likely for giant hail, while 15 min and 10 min lead times are more likely for large and small hail, respectively. Thus, the larger the hail, the longer the lead time.

5.2.3 Relation between Z_{DR}-column properties and hail size

In the previous section the investigation of Z_{DR}-columns was focused on relative, temporal changes in column height minutes ahead of attenuation intensification and hail occurrence on the ground. This made it possible to identify and approve Z_{DR}-columns as precursors of hail. More quantitatively, both the top height of Z_{DR}-columns above the melting layer and the maximum Z_{DR} inside Z_{DR}-columns show exploitable relations to the final hail size observed on the ground (Figure 5.10). Smaller hail diameters coincide with low values of Z_{DR}-column height and low

values of maximum Z_{DR} in Z_{DR}-columns. Vice versa, larger hail diameters coincide with high values of Z_{DR}-column height and high values of maximum Z_{DR} in Z_{DR}-columns. I.e. Z_{DR}-columns allow for nowcasting final hail size as soon as hail growth is detected.

To quantify this qualitative result, the correlation between Z_{DR}-column height above the melting layer, maximum Z_{DR} inside the Z_{DR}-column and hail diameter on the ground is calculated. However, the Pearson correlation coefficient only provides information about direction and strength of an association between two variables. Here, the multiple correlation coefficient R is used, which allows to quantify how strong the association between e.g. two explanatory (assumed independent) variables x_1, x_2 and a third (dependent) variable y is (Edwards, 1979)

$$R^2 = \frac{\rho_{y,x_1}^2 + \rho_{y,x_2}^2 - 2\rho_{y,x_1}\rho_{y,x_2}\rho_{x_1,x_2}}{1 - \rho_{x_1,x_2}^2} \,, \tag{5.1}$$

where ρ_{y,x_1}, ρ_{y,x_2} and ρ_{x_1,x_2} are the Pearson correlation coefficients for each of the possible combinations (Thiébaux, 1994)

$$\rho_{a,b} = \frac{\sum_i^n (a_i - \bar{a})(b_i - \bar{b})}{\sqrt{\sum_i^n (a_i - \bar{a})^2 \sum_i^n (b_i - \bar{b})^2}} \tag{5.2}$$

where $\bar{a}$ and $\bar{b}$ are the mean values (e.g. $\bar{a} = \frac{1}{n}\sum_i^n a_i$) of the respective random variables a and b.

The statistical significance of the obtained multiple correlation coefficient is tested using the so-called F-test. If the ratio between explained and unexplained variance F (Lomax and Hahs-Vaughn, 2001)

$$F = \frac{R^2/m}{(1 - R^2)\,/\,(n - m - 1)} \,, \tag{5.3}$$

where n is the sample size and m the number of predictors, exceeds a critical value F_{crit}, the null-hypothesis is rejected. F_{crit} is obtained from a Fisher-Snedecor distribution with m and $n - m - 1$ as degrees of freedom with significance level κ (Edwards, 1979; Lomax and Hahs-Vaughn, 2001).

The multiple correlation coefficient between Z_{DR}-column height above the melting layer (used for x_1), maximum Z_{DR} inside the Z_{DR}-column (used for x_2) and hail diameter on the ground (used for y) is 0.820 and $F = 31.77$. With $m = 2$ and $n = 34$ the critical score F_{crit} is 3.31 for significance level $\kappa = 0.05$ and 5.37 for $\kappa = 0.01$ and thus the null-hypothesis is rejected (Edwards, 1979). I.e. Z_{DR}-column properties can be used to predict a later hail diameter on the ground using a linear relation.

Also the lead time can be expressed in a linear relation of Z_{DR}-column height above the melting layer and maximum Z_{DR} inside the Z_{DR}-column. The multiple correlation coefficient of 0.542 indicates a weaker relation, but with $F = 6.46$ the relation is still statistically significant.

TABLE 5.1: Estimated lead times for observed hail signatures in polarimetric radar data during severe hail events in Germany. The time given here is limited to 5 min resolution due to the measurement scheme. The hail size of the associated ground reports from the European Severe Weather Database are shown in the categories small (diameter < 2.5 cm), large (diameter < 5 cm) and giant (diameter ≥ 5 cm). 165 ground reports were issued within the radar range for 11 events. 34 times a lead time estimation could be verified using the reports without ambiguity.

event date (yyyy-mm-dd)	radar	lead time (min)	hail size category
2013-08-06	Memmingen	10	large
		15	giant
		15	giant
		20	giant
		15	large
		15	large
		15	large
2015-05-13	Feldberg	15	small
		20	giant
		10	large
		15	large
2015-07-05	Essen	10	large
		15	giant
		20	giant
2015-07-05	Flechtdorf	10	large
		10	small
		20	giant
		15	large
		15	small
2015-07-05	Türkheim	20	giant
		15	large
2015-07-18	Dresden	15	large
		10	large
		15	large
2016-05-27	Offenthal	15	small
2016-06-23	Essen	10	small
		15	giant
		15	giant
		20	giant
		20	giant
2016-06-24	Neuheilenbach	20	giant
		10	small
2016-06-24	Essen	10	small
2016-06-24	Türkheim	15	giant

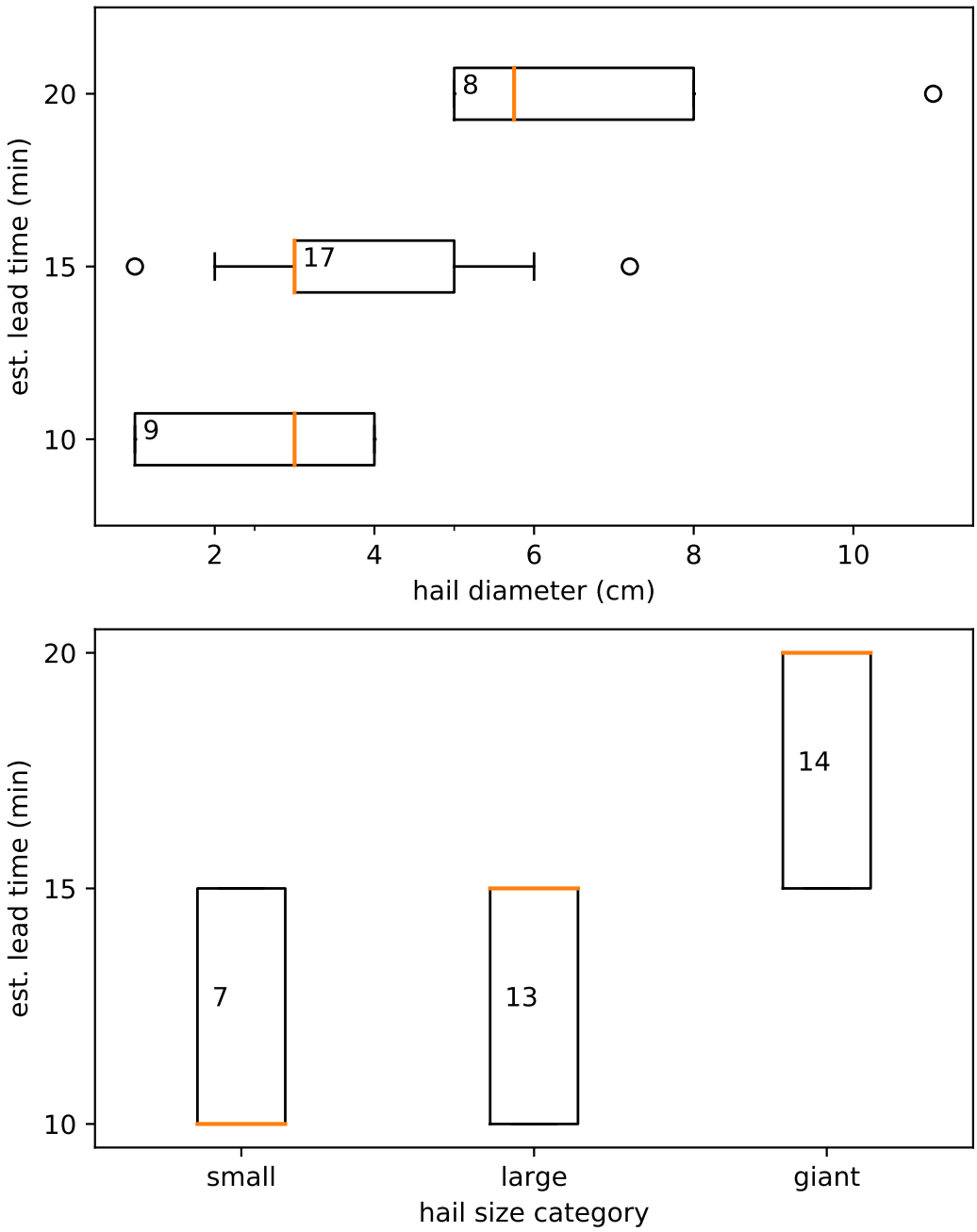

FIGURE 5.9: Boxplot of estimated lead times compared against hail diameter and category (same data as in Table 5.1). The thicker, orange line shows the median, while the box represents the range of 25- to 75-percentile of the data. Whiskers show the 5- and 95-percentiles. Outliers are denoted as circles. The numbers indicate the amount of data points used for each boxplot.

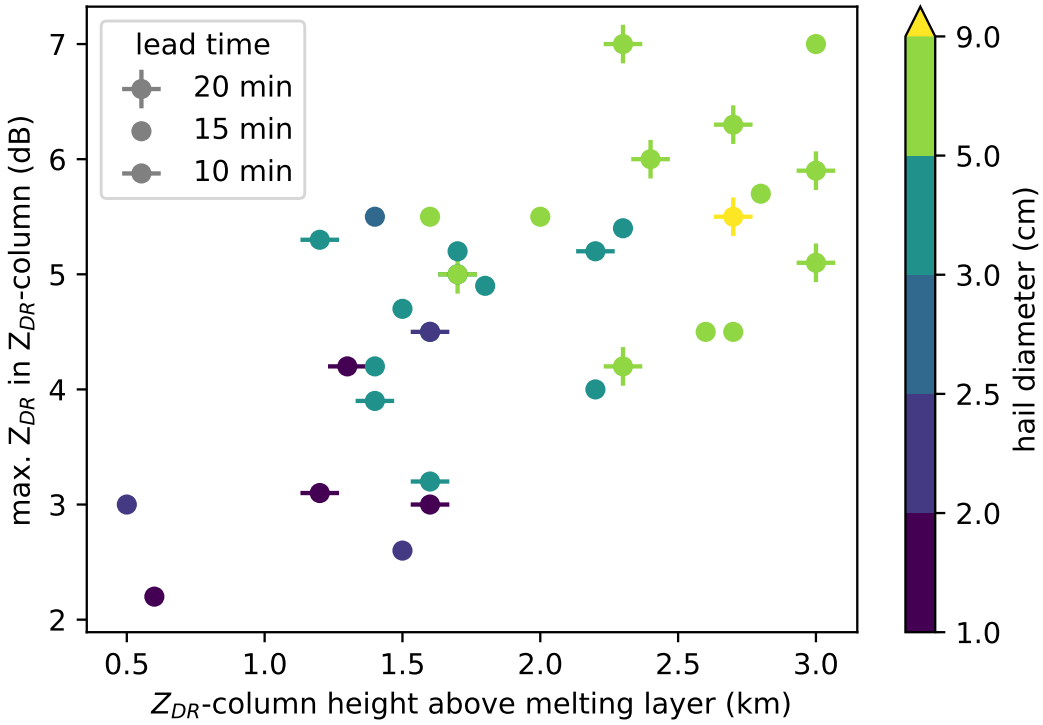

FIGURE 5.10: Scatter plot between Z_{DR}-column height above the melting layer in km and maximum differential reflectivity inside the Z_{DR}-column. The colors of the symbols indicate the ground reported hail diameter (see right scale). The symbol type quantifies the lead time between a Z_{DR}-column height spike and hail at the ground: Dots with minus signs indicate a lead time of 10 min, dots with plus signs 20 min and all others 15 min.

5.3 Nowcasting of Hail

Using the insights from sections 5.2.2 and 5.2.3 nowcasting schemes for hail and hail size at the ground based on radar polarimetry can be developed. A nowcasting scheme for predicting the final hail size once hail growth is detected ("prediction scheme"), and a scheme for detecting matured, falling hail and discriminating its size ("detection scheme"), are explained in the following.

5.3.1 Prediction scheme

The height of Z_{DR}-columns above the melting layer and maximum Z_{DR} inside the columns are used here for estimating the final hail diameter. In a first step, a fuzzy logic, similar to Park et al. (2009), is applied to obtain a hail size category. Based on the most likely size category, a lead time is then chosen according to the findings from section 5.2.2. With the hail size category and the lead time a prediction for future hail occurrence is obtained.

For each hail size category i and variable x in use, a membership function P_i can be defined with parameters a, b, c, d taken from Table 5.2, so that

$$P_i(x) = \begin{cases} 0, & \text{if } x < a, \\ \frac{x-a}{b-a}, & \text{if } a \leq x < b, \\ 1, & \text{if } b \leq x < c, \\ \frac{d-x}{d-c}, & \text{if } c \leq x < d, \\ 0, & \text{if } x \geq d \quad . \end{cases} \tag{5.4}$$

For computational efficiency, equation 5.4 is reformulated into

$$P_i(x) = \max\left[\min\left(\frac{x-a}{b-a}, 1, \frac{d-x}{d-c}\right), 0\right] \text{ for } a < b \leq c < d \quad . \tag{5.5}$$

The hail size category with the highest summed probability across all involved variables is then selected. Except for weighting, which is omitted, this is similar to the approach in section 4.1.1.

The fuzzy logic introduced above is applied at every time step for every cell to predict future hail size occurrence. Depending on the expected final hail size yielded by the fuzzy logic, the lead time is adjusted: 10 min for small hail, 15 min for large hail and 20 min for giant hail. This adjustment is based on the observed dependency of hail size on lead time (see section 5.2.2 and Figure 5.9). The cell for which the prediction was done is then marked with the hail size and expected lead time. Examples of how this prediction scheme performs is shown later in section 5.3.3.

TABLE 5.2: Parameters defining the shape of the trapezoidal membership function for the fuzzy logic to discriminate hail size by Z_{DR}-column intensity. The values have been rounded to the second decimal place.

	membership function parameters	small hail	large hail	giant hail
Z_{DR}-column height above melting layer (km)	a	0.50	0.82	1.76
	b	0.50	1.75	2.29
	c	1.12	1.78	∞
	d	1.93	2.53	∞
max. Z_{DR} in Z_{DR}-column (dB)	a	2.00	3.13	4.08
	b	2.00	4.40	5.83
	c	3.59	4.57	∞
	d	4.51	6.50	∞

5.3.2 Detection scheme

The prediction scheme analyses hail growth to make predictions for future hail size. As such, it cannot discriminate the size of present hail and thus has no ability to verify or correct its predictions. A reliable method to detect and discriminate hail size in real time is introduced as the detection scheme to complement the prediction.

The detection scheme does not rely on mere values of Z_{DR}-column properties, but rather analyzes the behavior of updraft intensity and attenuation. Hereby, strong attenuation at C band is exploited as a primary hail fall indicator.

For each cell at time step t a detection of hail is investigated using Z_{DR}-column height above the melting layer and attenuation coefficient α. It is assumed the hail occurrence is accompanied by α values above the climatological level of 0.08 dB/° (Ryzhkov et al., 2013b). Furthermore, it is assumed that an updraft has to persist for at least 15 min or 30 min to facilitate large or giant hail respectively (Ziegler et al., 1983; Miller et al., 1988, 1990; Kennedy et al., 2001; Kumjian et al., 2014). In radar data, Z_{DR}-columns seem to collapse after intensification. This is not necessarily a weakening of the updraft, but most likely due to contamination of the Z_{DR}-column by dry, tumbling hail, as Kumjian et al. (2014) point out. Therefore, these collapses are used as additional indicators of hail fall. A graphical display of the algorithm (Figure 5.11) provides the decision tree for no hail, small hail (diameter < 2.5 cm), large hail (diameter < 5 cm) and giant hail (diameter ≥ 5 cm). The algorithm first checks the updraft conditions based on the Z_{DR}-column properties, such as minutes of Z_{DR}-column existence and Z_{DR}-column height above the melting layer (ZCH), and stores the result as "possible hail size" category. In the second part, the algorithm checks for attenuation behavior, e.g. sudden intensification (spike) of α, and secondary hail fall indicators, such as sudden weakening of Z_{DR}-columns (collapse).

Finally, a detected hail size category is concluded using the "possible hail size" category and the hail fall indicators from the second part.

Spike detection

To detect spikes in the timeseries of variable X at time step t only the last w time steps are investigated. If $t < w$, then X is padded with zeros, so that the length of the vector $X(t-w,\ldots,t)$ equals w. If $X(t)$ does not meet a threshold $x_{\text{threshold}}$, then no spike is detected. Otherwise, a spike is detected if the following condition is met:

$$\Delta X(t) + X(t) - \bar{X} \geq \xi \cdot \sqrt{\tfrac{1}{w-1}\sum_{s=t-w}^{t}\left[X(s)-\bar{X}\right]^2}\ , \text{ where} \tag{5.6}$$

$$\bar{X} = \tfrac{1}{w}\sum_{s=t-w}^{t}\left[X(s)\right] \text{ and} \tag{5.7}$$

$$\Delta X(t) = X(t) - X(t-1)\ . \tag{5.8}$$

ξ is a factor to scale the condition. For the following, ξ was set to 1.5. w is set to 5 for the height of the Z_{DR}-column above the melting layer and to 4 for the attenuation coefficient α. The threshold $x_{\text{threshold}}$ is set to 500 m and 0.15 dB/° respectively. These values were selected after experimenting with different thresholds and were found to best match the data.

Collapse detection

Besides spiking behavior, Z_{DR}-columns can also show sudden weakening. These collapses do not behave like negative spikes, therefore a different condition is applied to identify a collapse of variable X at time step t:

$$X(t) - \text{median}\left[X\left(t - l_{Z_{DR}\text{-column}},\ldots,t\right)\right] \leq x_{\text{threshold,collapse}}\ , \tag{5.9}$$

where $l_{Z_{DR}\text{-column}}$ is the number of time steps of the currently observed Z_{DR}-column's lifetime. $x_{\text{threshold,collapse}}$ is set to -300 m. Collapse detection is not used for α, therefore no threshold for the condition is defined.

5.3.3 Nowcasting examples

The two developed schemes (prediction scheme (see section 5.3.1) and detection scheme (see section 5.3.2)) are designated for operational forecasting services. Nowcasting examples for three selected events are shown. For these examples, the output of the detection and prediction schemes are applied to the 40 dBZ contour of the tracked cell. I.e. the prediction or detection covers an area, not just a single point underneath the cell's updraft. In this study the focus is not the exact impact point of hail, but the ability to reliably predict and detect hail and discriminate its size. In the following the outputs of the two schemes are compared with ground truth to assess spatial and temporal agreement.

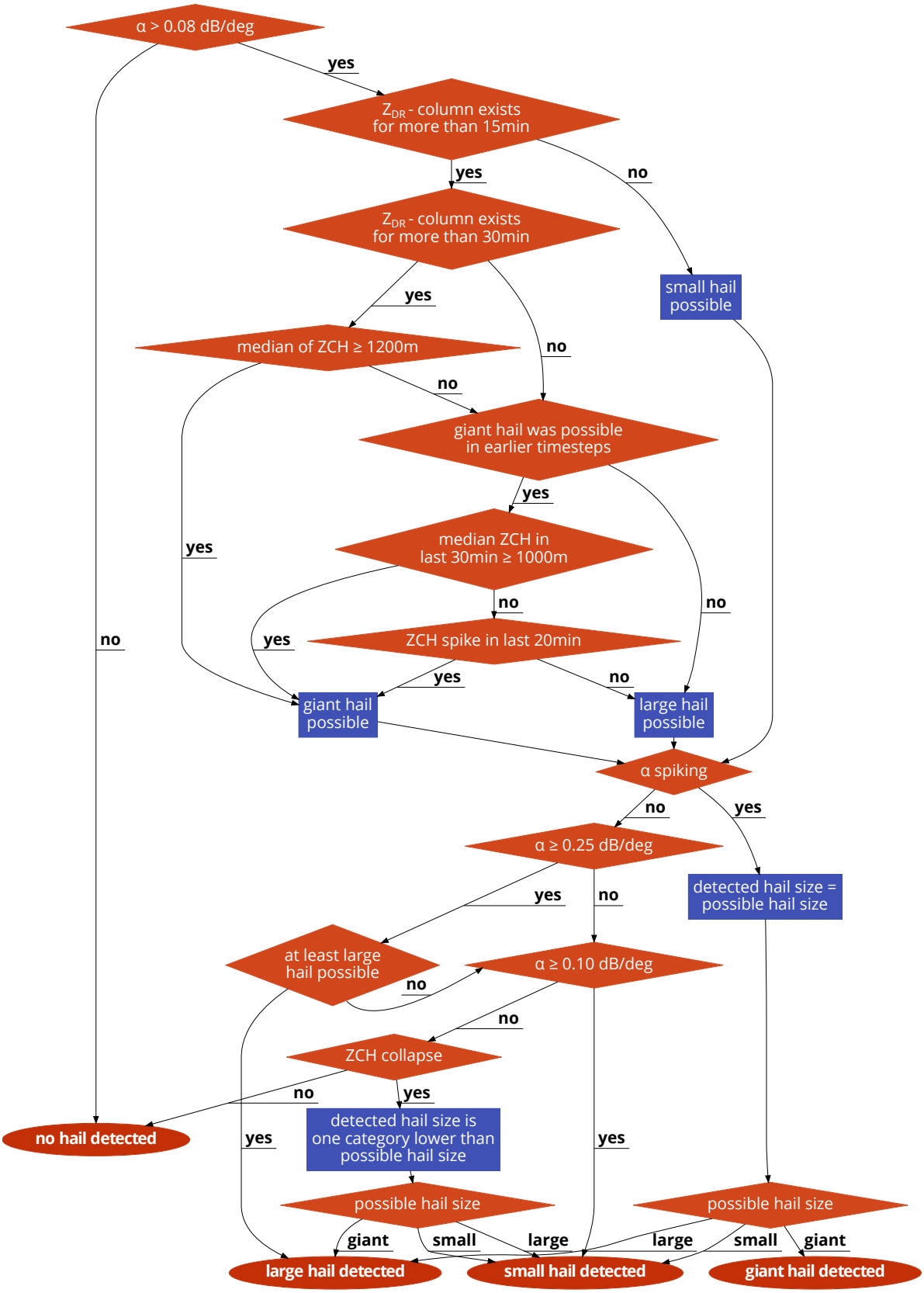

FIGURE 5.11: Flow chart of the hail detection scheme. The decision tree is executed at every time step t for every cell using the attenuation coefficient α, the number of minutes a Z_{DR}-column exists and the height of the Z_{DR}-column above the melting layer (ZCH). Spike and collapse detection takes equations 5.6 and 5.9 as conditions and follows the description in the text in section 5.3.2.

A supercellular event occurring on 06.08.2013 produced the largest hail (14.1 cm in diameter, 360 g) measured and preserved in Germany. Other hail stones had diameters mostly between 5 cm and 10 cm and caused severe damage to agriculture, buildings and vehicles[6]. A hail swath of the prediction scheme forecasts is displayed for this event in Figure 5.12. Reports of hail observed on the ground, depicted with red symbols, show a similar swath. Although not every report size was predicted correctly, the size categories do not differ by more than one and the overall structure and variation matches the reports.

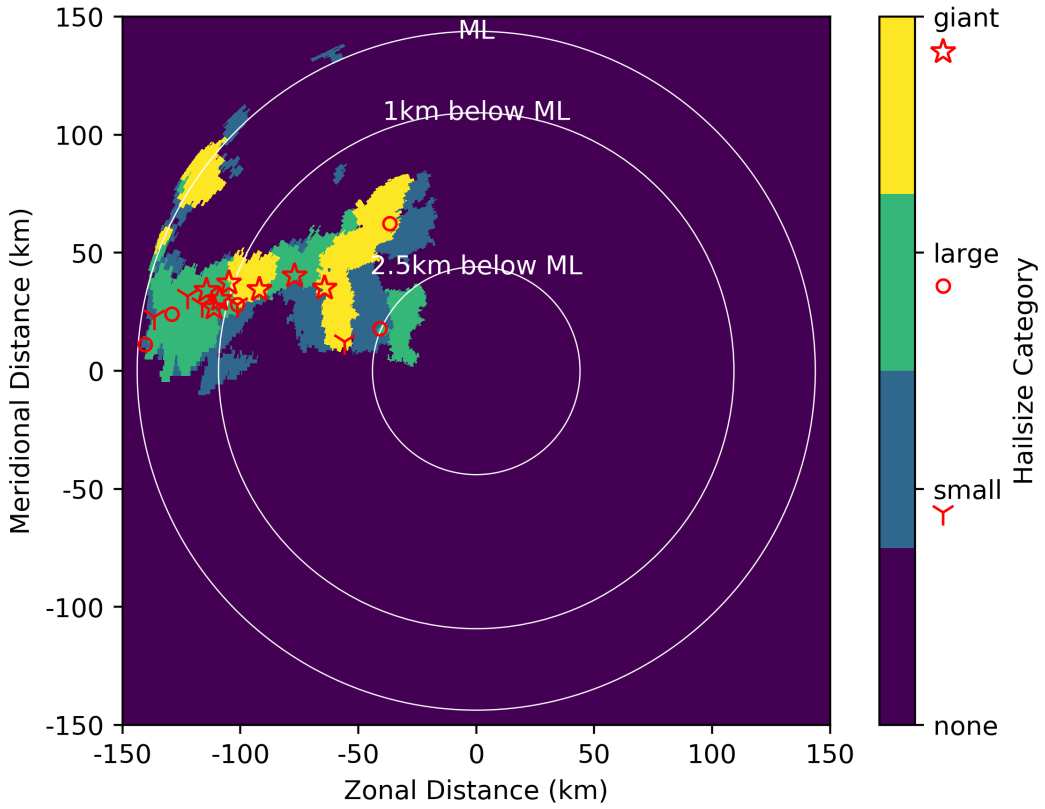

FIGURE 5.12: Predicted hail swath (colored contours) obtained by integrating the prediction scheme output over a time period from 11 - 15 UTC on 06.08.2013, monitored by radar Memmingen. Red symbols indicate size categories of hail ground reports. The white rings show the height underneath or at melting layer (ML) height, which was at 3960 m above ground level during this event.

In order to compare the temporal structure, too, time series of predicted hail and used Z_{DR}-column properties are shown in Figure 5.13. While the spatial structure of the prediction matched quite well (Figure 5.12), several giant hail stones were underestimated. Especially for the report with the largest hail (around 13:35 UTC) the Z_{DR}-column properties are quite low. For more than an hour this tracked cell is associated with large and giant hail. Due to increasingly strong attenuation and signal extinction in the core of the cell, the detection of Z_{DR}-columns became difficult and diminished for several time steps (~13:10 - 13:45). Overlapping radars might

[6]Source: https://www.wetteronline.de/wetter-videos/2013-08-26-cv, last accessed on 01.11.2019 14:14 UTC

solve this problem in other cases, however for this event, data of other, overlapping radars was not available.

The hail swath calculated by the detection scheme (Figure 5.14) differs from the prediction scheme, and corresponds slightly better with the hail reports. The left panel additionally shows the intermediate output of the detection scheme, the possible hail size (see Figure 5.11). This shows that, concerning the updraft condition, the tracked cell had the capability of producing giant hail almost everywhere along the swath.

By analyzing the time series of the detection scheme output (Figure 5.15, lower left panel) a better coverage of the giant hail by the detection scheme is achieved for this tracked cell. Also, the report with the largest hail (13:35 UTC) is correctly detected. The time series of the attenuation coefficient α (Figure 5.15, lower right panel) indicates very strong attenuation (median of α within whole cell stays above 0.4 dB/°) $\sim$ 15 min before and after the report with the largest hail.

On July 5th, 2015 several most-likely supercell thunderstorms brought severe winds and hail damage to Southwestern Germany. Hail diameters of up to 7 cm were measured[7]. The hail swath of forecasted hail by the prediction scheme is displayed in Figure 5.16. Only two locations of hail were indicated by the reports in the vicinity of radar Türkheim. However, both locations were successfully covered by the prediction scheme. While overestimating the hail at the position further to the North (100 km meridional distance, -75 km zonal distance) by one category, the lower position (90 km meridional distance, -100 km zonal distance) was correctly predicted as giant hail.

On August 30th, 2015 a most-likely supercellular storm over the Netherlands and North Rhine-Westfalia produced hail of up to 8 cm, killed at least 65 birds and caused severe damage to over 75 cars and several houses[8]. The hail swath of forecasted hail by the prediction scheme is displayed in Figure 5.17. The cell was already producing large hail when it arrives at radar range. Despite the far distances the first reports in the West (50 km meridonal distance and -110 km zonal distance) are correctly predicted. A bit closer to the radar two giant hail reports (40 km meridonal distance and -100 km zonal distance) are underestimated. Also, one report of large hail (10 km meridonal distance and -100 km zonal distance) is completely missed.

The time series for a tracked convective cell during this event, depicted in Figure 5.18, shows intense Z_{DR}-columns. Here again it is visible that the first hail reports have been predicted correctly and all later reports of giant hail are underestimated in size.

Also for this event, the hail swath calculated by the detection scheme (Figure 5.19) differs and detects almost all giant hail reports correctly. Nevertheless, the same

[7] Source: https://www.skywarn.de/jahr-2015/5-juli, last accessed on 06.11.2019 17:12 UTC

[8] Sources: http://www.derwesten.de/nrz/staedte/emmerich/hagel-toetete-65-stare-in-emmerich-id11046000.html, last accessed on 14.11.2019 17:24 UTC; https://www.bd.nl/zaltbommel/onweer-in-brabant-en-gelderland-verkeer-op-a2-stopt-vanwege-megahagel-foto-s-en-video~aab97ce0/, last accessed on 14.11.2019 17:25 UTC

large hail report (10 km meridonal distance and −100 km zonal distance) missed in the hail swath of the prediction scheme is missed here, too.

Analysing the time series for the same tracked convective cell as above (Figure 5.20) reveals that the detection scheme detected all large and giant hail correctly (lower left panel), except for one large hail report (centered at 21:05 UTC). While the updraft allowed giant hail to occur for the most time of the tracked cell (upper left and right panel), the attenuation varied (lower right panel), and allowed to precisely detect when giant hail actually fell.

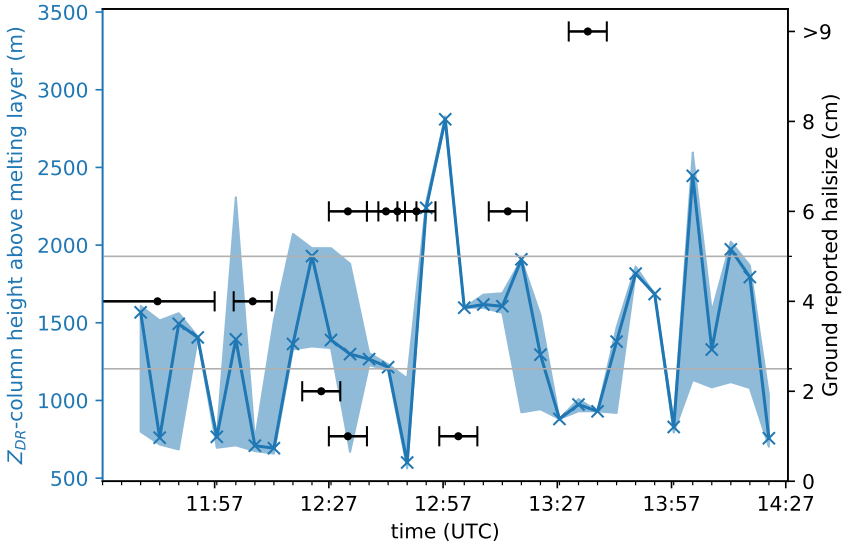

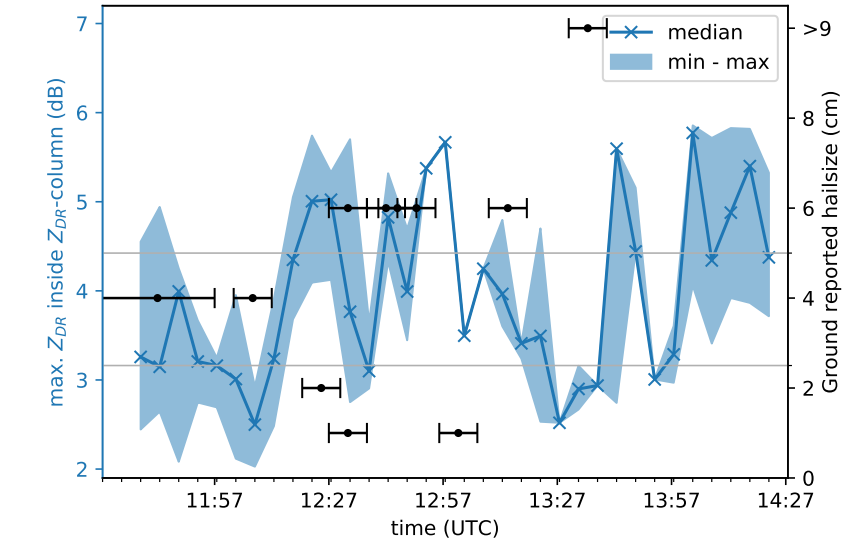

(A) Z_{DR}-column properties

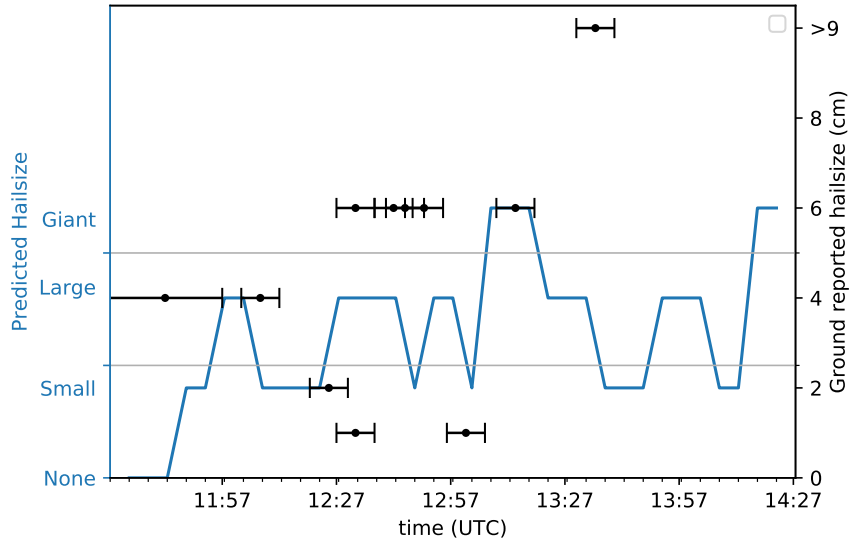

(B) predicted hail

FIGURE 5.13: Time series of Z_{DR}-column height above the melting layer, max. Z_{DR} inside Z_{DR}-columns and predicted hail size using the prediction scheme for a tracked cell on 06.08.2013, monitored by radar Memmingen. The black bars show the time window of the ground reports and the reported hail diameter (scale on the right axis).

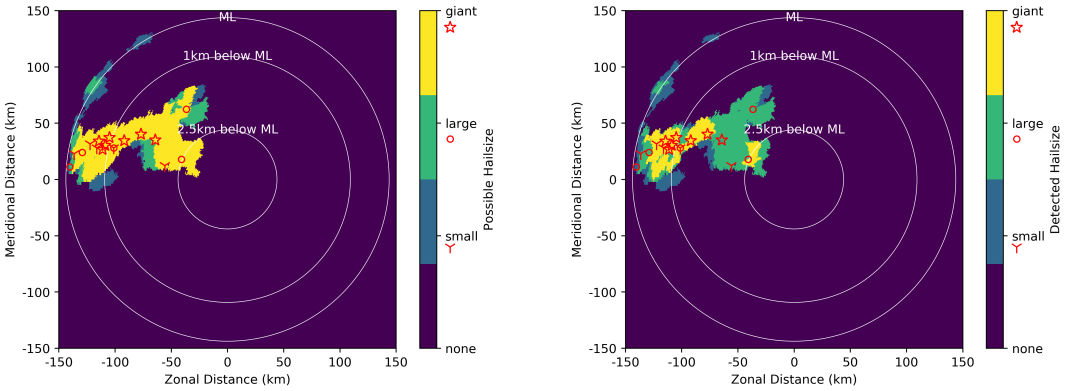

FIGURE 5.14: Possible (left) and detected (right) hail swath (colored contours) obtained by integrating the detection scheme output over a time period from 11 - 15 UTC on 06.08.2013, monitored by radar Memmingen. Overlaid in red symbols are size categories of hail ground reports. The white rings show the height underneath or at melting layer (ML) height, which was at 3960 m above ground level during this event.

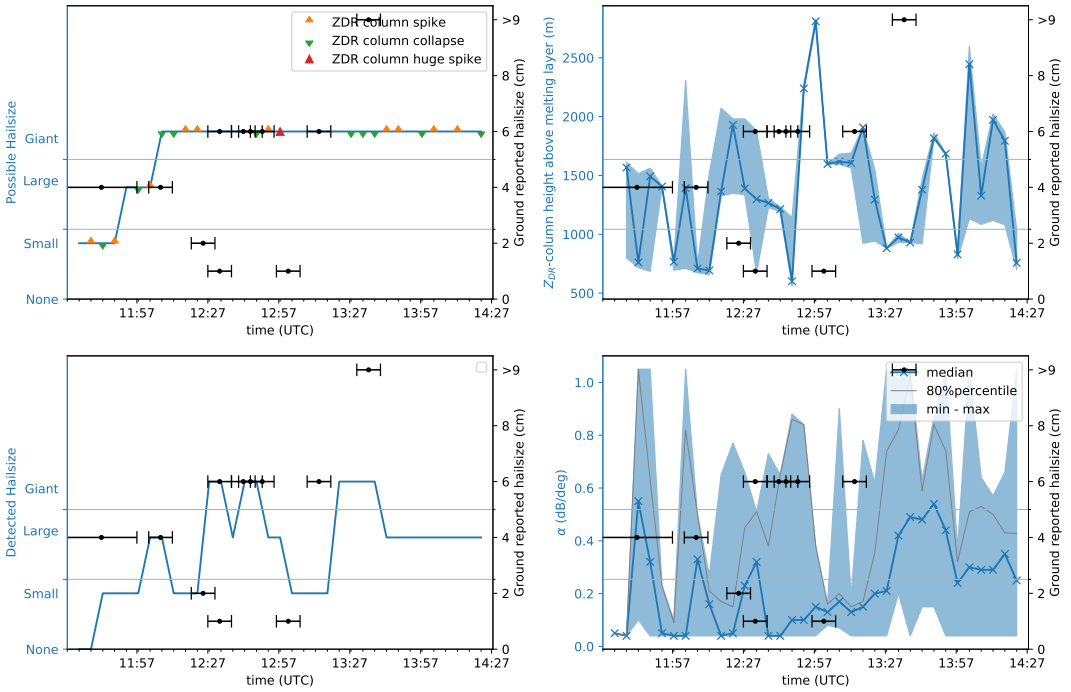

FIGURE 5.15: Time series of possible hail size (upper left), detected hail size (lower left), Z_{DR}-column height (upper right) and attenuation coefficient α (lower right) using the detection scheme for the same tracked cell as in Figure 5.13. The black error bars show the time span of the ground reports and the reported hail diameter (scale on the right axis).

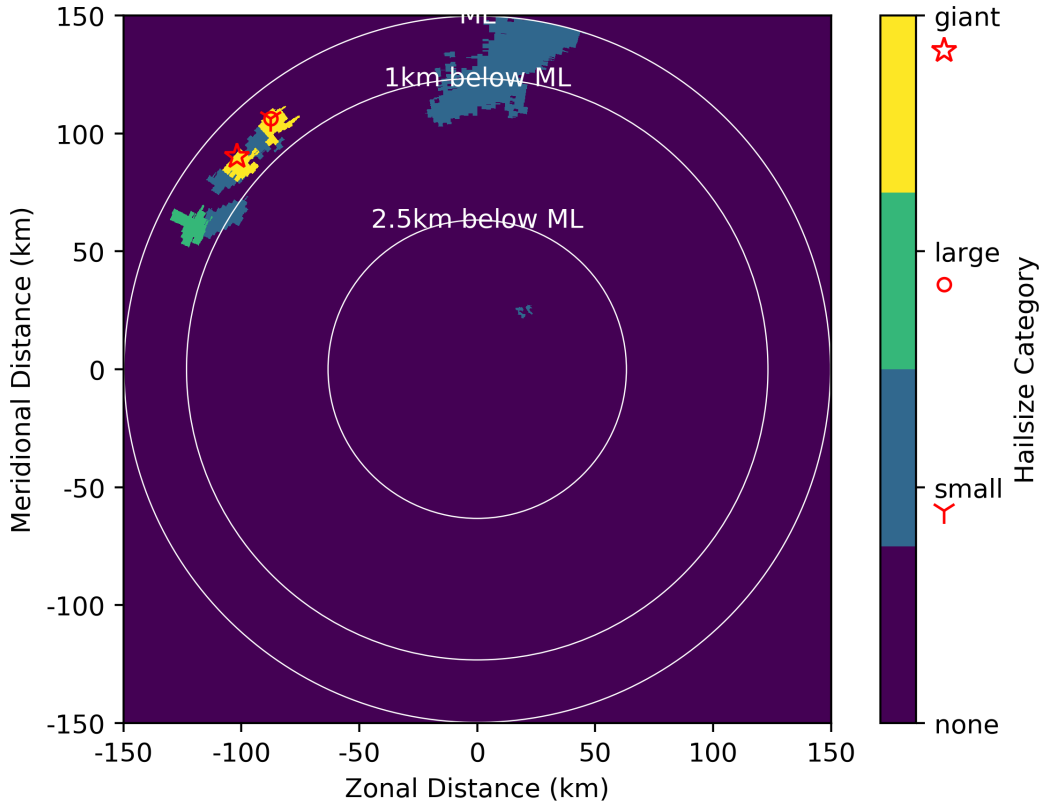

FIGURE 5.16: Predicted hail swath (colored contours) obtained by integrating the prediction scheme output over a time period from 18 - 22 UTC on 05.07.2015, monitored by radar Türkheim. Red symbols indicate size categories of hail ground reports. The white rings show the height underneath or at melting layer (ML) height, which was at 4390 m above ground level during this event.

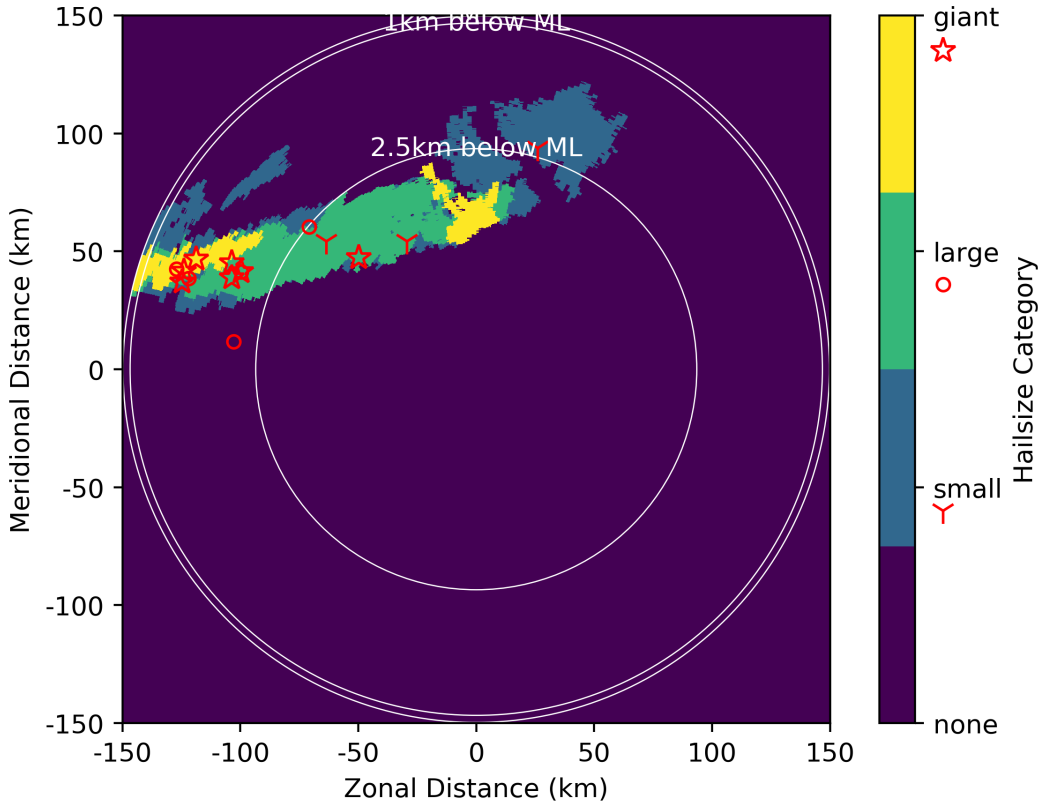

FIGURE 5.17: Predicted hail swath (colored contours) obtained by integrating the prediction scheme output over a time period from 19 - 00 UTC on 30.08.2015, monitored by radar Essen. Red symbols indicate size categories of hail ground reports. The white rings show the height underneath or at melting layer (ML) height, which was at 4510 m above ground level during this event.

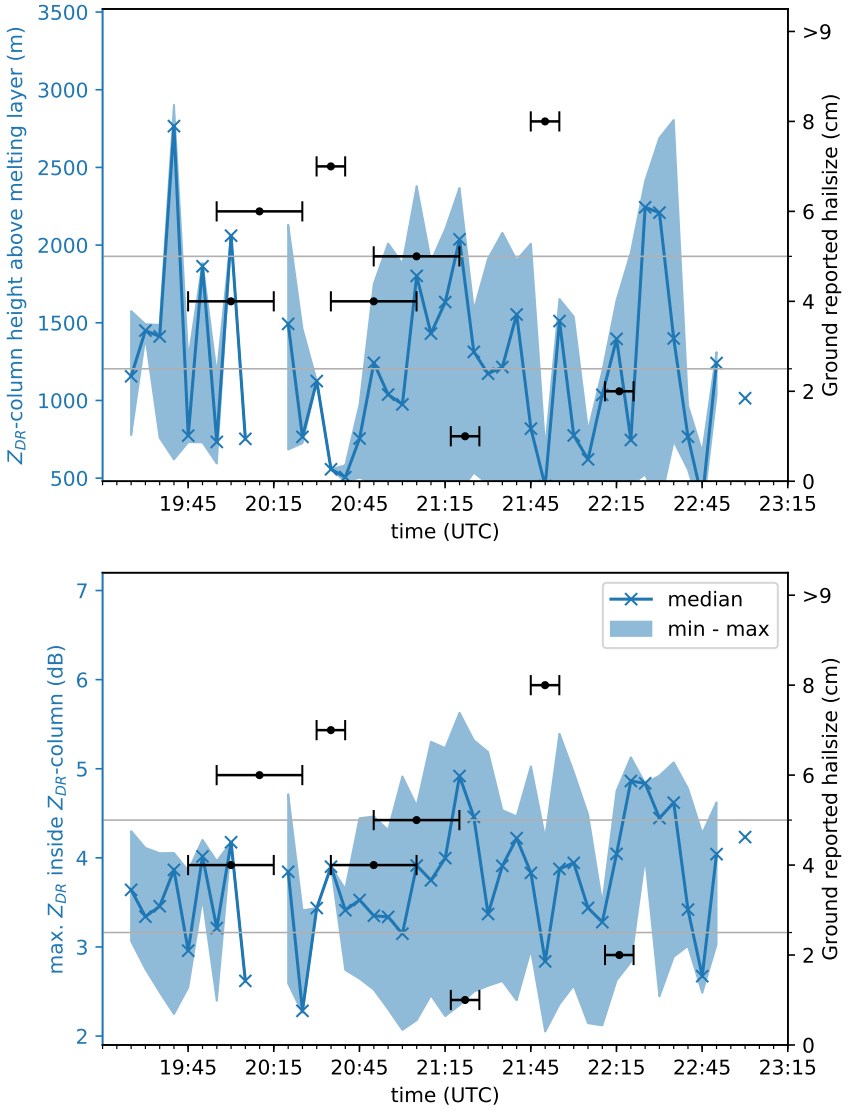

(A) Z_{DR}-column properties

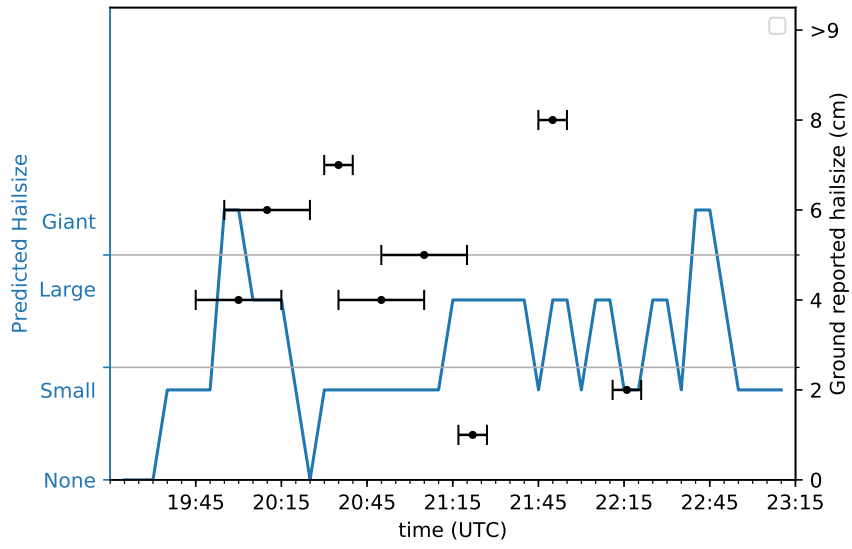

(B) predicted hail

FIGURE 5.18: Like Figure 5.13, but for 30.08.2015, monitored by radar Essen.

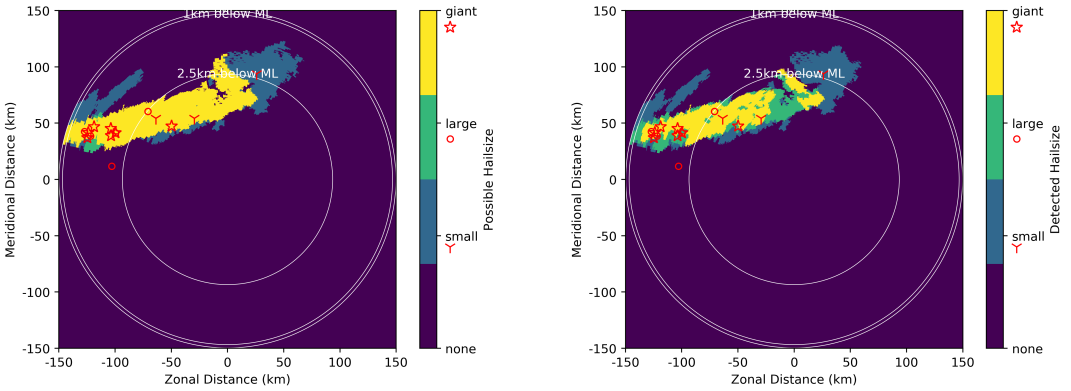

FIGURE 5.19: Possible (left) and detected (right) hail swath (in colored contours) obtained by integrating the detection scheme output over a time period from 19 - 00 UTC on 30.08.2015, monitored by radar Memmingen. Overlaid in red symbols are size categories of hail ground reports. The white rings show the height underneath or at melting layer (ML) height, which was at 4510 m above ground level during this event.

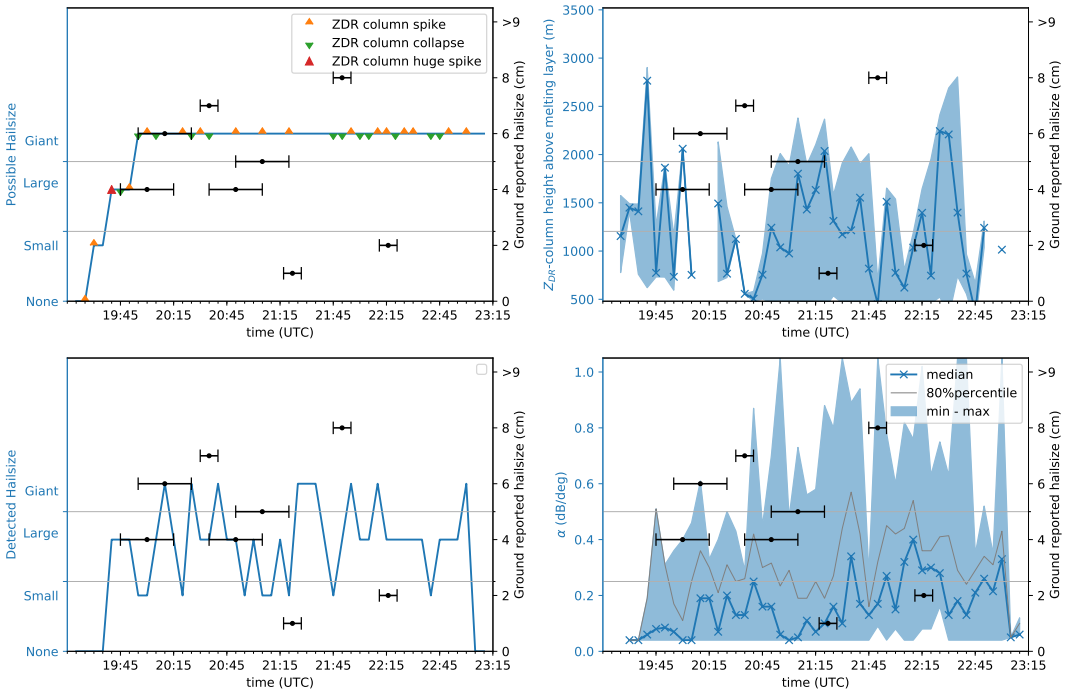

FIGURE 5.20: Time series of possible hail size (upper left), detected hail size (lower left) and Z_{DR}-column properties (right panels) using the detection scheme for the same tracked cell as in Figure 5.18. The black error bars show the time span of the ground reports.

5.4 Evaluation

The two developed schemes provide hail nowcasting capabilities and are evaluated against ground truth. For 16 hail bearing events in Germany radar data and ground reports from the European Severe Weather Database (ESWD) are used. For each event convective cells are identified and tracked, as described in section 5.1.3, and the two developed schemes are applied to obtain time series of "detected" and "predicted" hail. As the surface reports have temporal error margins of mostly 15 min and up to 120 min, the whole time window is assumed to be valid for hail occurrence.

To evaluate and score the prediction quality for each report, the following questions are decided in sequence. If any question is answered positively, further questions are skipped and the report is categorized accordingly. By iterating through all reports, no report is evaluated more than once or can be in multiple categories for a single event.

1. Is the correct hail size predicted at the time step in the middle of the time window of the report? → category "direct hit"
2. Is the correct hail size predicted within the time window of the report? → category "time-window hit"
3. Are all estimated hail sizes larger than the reported hail size within the time window of the report? → category "overestimated"
4. Are all predicted hail sizes smaller than the reported hail size within the time window of the report? → category "underestimated"
5. Are there other reports of bigger hail size within the time window of the report? → category "ambiguous"
6. Is no hail predicted within the time window of the report? → category "missed".

Otherwise, category "other" is selected, which means both under- and overestimation are present within the time window. The category "ambiguous" might be used for overlapping reports as superposition of bigger hail might diminish capabilities of smaller hail prediction, as pointed out in section 5.2.2.

The prediction scheme (Figure 5.21a) underestimates a quarter of all reports used, but hardly overestimates hail sizes at all. 10 % of all reports are missed, but more than a third is correctly predicted in time and size. The detection scheme (Figure 5.21b) misses slightly more reports (14.7 %), but scores much better with 61.3 % correct detection in time and size. Also, underestimation and overestimation are lower with less than a fifth of all reports in total. Both schemes have reports which could not be analyzed due to ambiguity, but this is not a shortcoming of the schemes.

Most of the differences between the overall scores of the schemes (Figure 5.21) are also visible throughout individual events (Figure 5.22). However, some events

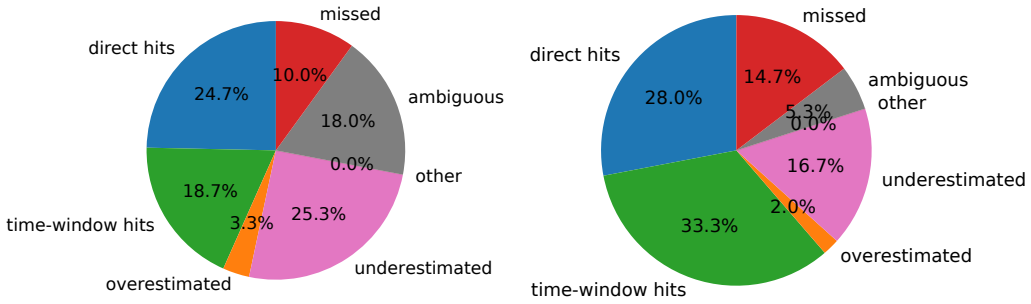

(A) prediction scheme

(B) detection scheme

FIGURE 5.21: Overall scoring result for evaluation of prediction and detection scheme for 16 hail bearing events. The scoring categories and the evaluation method are described in the text in section 5.4.

show major disagreements between the two schemes. E.g. the detection scheme (Figure 5.22b) misses most reports for the event on 2015-07-05 monitored by radar Flechtdorf, which the prediction scheme does not miss. During the event on 2013-08-06 monitored by radar Memmingen, the prediction scheme (Figure 5.22a) underestimates 6 reports, which are almost all scored as correctly detected by the detection scheme. The event on 2016-04-13 monitored by radar Isen misses all reports in both schemes. This event had only two reports of accumulated very small hail (mostly 1 cm to 2 cm or smaller in diameter). The attenuation was too low to trigger the detection scheme for the observed cells at the hail impact location. Small hail was detected approximately 5 km to the North-East of the hail impact location. Also, the prediction scheme failed, as no significant updrafts were detected in the vicinity. The event still caused damage to the local towns, as the hail accumulated within minutes and covered streets and buildings with a 5 cm thick layer[9].

5.4.1 Random prediction

There is no scoring category for false alarms, as ground reports can only state hail occurrence, not hail absence. To cope with this issue and to qualify the scoring results, the physical-based schemes are compared against random predictions. These random predictions are based on the statistics of the 150 reports that have been used for evaluation before. All hail sizes that have been reported within the vicinity of tracked cells are used to build a distribution of hail sizes. Among the reports used, all categories are almost equally likely, with the highest probability for giant hail ($p_{\text{size,giant}} = 39.1\,\%$), followed by large hail ($p_{\text{size,large}} = 32.3\,\%$) and small hail ($p_{\text{size,small}} = 28.6\,\%$). The lifetime of the tracked cells (the number of time steps a cell is observed by the radar) and the number of reports occurring during their lifetimes is used to calculate a probability of hail occurrence per cell per time step, which

[9]Source: https://www.merkur.de/lokales/bad-toelz/bad-toelz-ort28297/schweres-unwetter-gewitter-hagel-toelz-6306930.html, last accessed 15.11.2019 10:58UTC

results in $p_{\text{hail}} = 16.82\,\%$. I.e. for each time step the probability of e.g. giant hail occurring is $p_{\text{giant hail}} = p_{\text{hail}} \cdot p_{\text{size,giant}} \approx 6.58\,\%$. The probabilities are used to run a prediction 1000 times and is then evaluated analogous to the other two schemes. The overall scoring for this statistically based random prediction is shown in the pie chart in Figure 5.23. Although the random prediction inherits the probabilities of the reports, which are used to evaluate and score, the scores are very low compared to the other two physical-based schemes. More than half of the reports are missed and only a fifth are predicted correctly in time and size. The ratio of ambiguity is similar to the other schemes, as well as the rate of overestimation, while the ratio of underestimation is reduced.

5.4.2 Evaluation statistics

The scoring results for the prediction scheme, the detection scheme and the random prediction are condensed into three categories: a positive category, indicating a correct prediction ("direct hits" and "time-window hits"), a neutral category, where hail was predicted at the right time but not size ("overestimated", "underestimated" and "other") and a negative category, where hail was reported but not predicted ("missed"). In addition to that, a ratio of time steps with hail predictions, but no reports, i.e. a pseudo false-alarm-ratio, is added. These four categories are displayed in Table 5.3. Both physical-based schemes beat the random prediction by far in the first three categories introduced. Yet, the ratio of predicted hail without ground truth is quite high compared to the random prediction. However, this is not necessarily a high false-alarm ratio. Absence of hail reports does not indicate that there was no hail. E.g. the schemes might have correctly predicted hail and hail might have occurred at the ground without a report being issued. Reports are mostly issued by volunteers and trained storm spotters (Dotzek et al., 2009), therefore it cannot be expected that every hail occurrence is observed.

The schemes shown have different nowcasting time windows. As the detection scheme can only detect hail which is already falling, it does not provide an improvement to the lead time. The prediction scheme can improve the lead time by 10 min to 20 min as shown in sections 5.2.2 & 5.3.1. A random prediction obviously can predict for as many time steps into the future as desired, but the usability of this is questionable.

TABLE 5.3: Statistics of evaluation results for the detection and prediction scheme and statistically based random prediction. Results have been rounded to the first decimal place.

	Detection scheme	Prediction scheme	random prediction
Lead time (min)	0	10-20	∞
Correct prediction	64.8 %	52.9 %	20.9 %
Hail predicted, but wrong size	19.7 %	35.0 %	19.3 %
Hail present, but no prediction	15.5 %	12.1 %	59.8 %
Hail predicted, but no ground truth	38.0 %	35.6 %	11.1 %

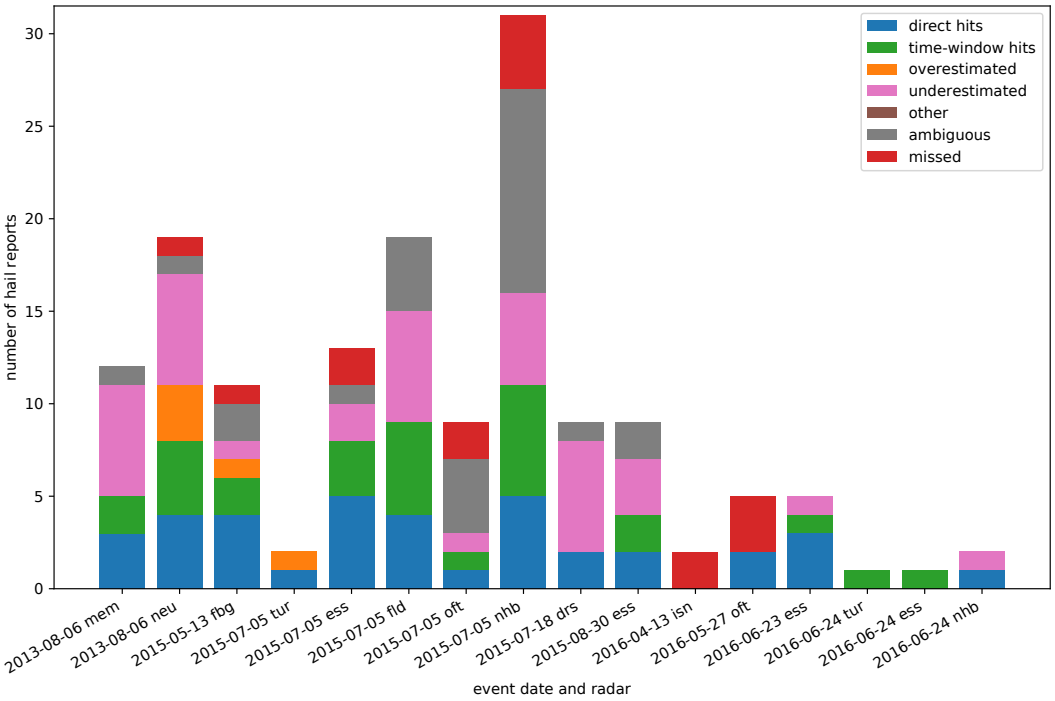

(A) prediction scheme

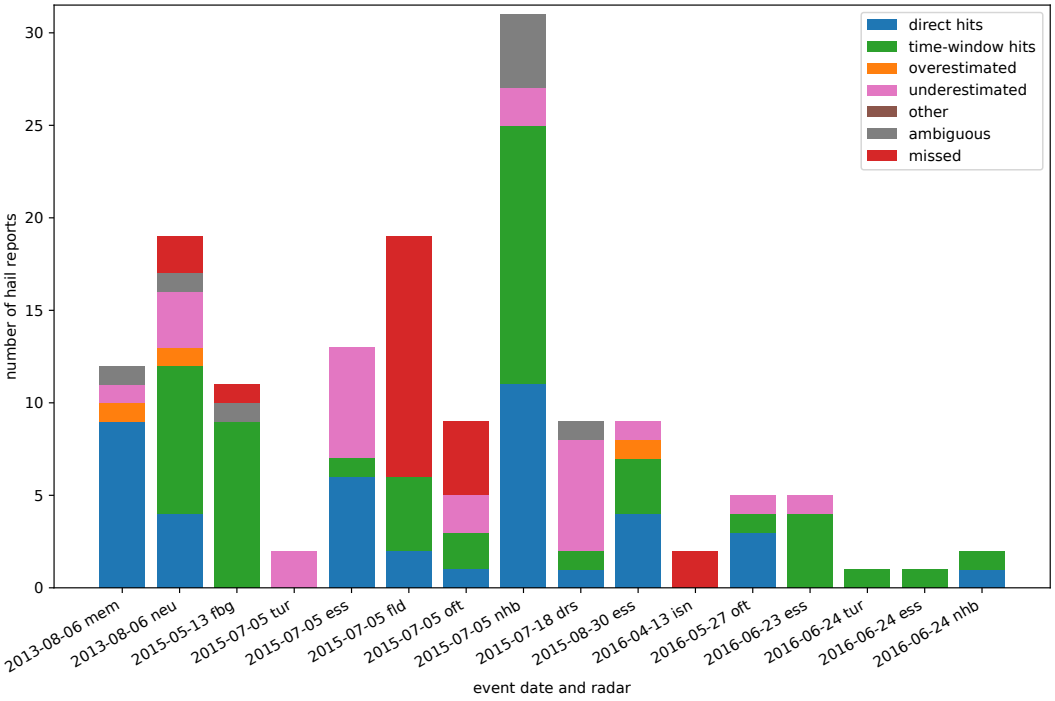

(B) detection scheme

FIGURE 5.22: Scoring result for evaluation of prediction scheme and detection scheme for each of the 16 hail bearing events. The scoring categories and the evaluation method are described in the text in section 5.4.

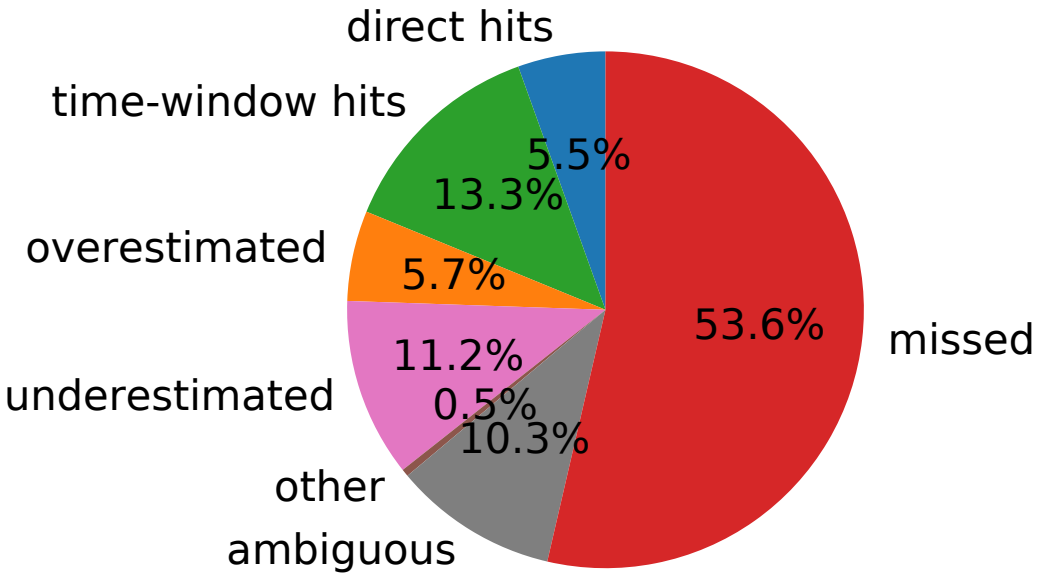

FIGURE 5.23: Scoring results for evaluation of the statistically based random prediction as described in section 5.4.1.

5.5 Discussion

131 of the in total 165 surface hail reports could not be used for analysis of the time-lagged correlation between spikes of Z_{DR}-column height and attenuation coefficient α (see section 5.2). Most of these reports were discarded because of temporal overlaps with other reports in cases when many cells produced hail in a very short time period (e.g. see Figure 5.7). These overlaps inhibited a clear matching of attenuation spikes to hail reports. The low temporal resolution of the radar data of 5 min is clearly a limitation for the analysis. This study would have benefited from the much higher resolution possible with polarimetric phased array radars. Simulations by Kumjian et al. (2014) and Ilotoviz et al. (2018) indicate that the time lag between peak Z_{DR}-column height and largest hail at the surface should lie between 12.5 min and 15 min, which agrees with the observational evidence presented here. Overall, the observation time windows in surface hail reports were often longer than 15 min and sometimes exceeded 1 h. This made it particularly difficult to automate the analysis with the radar observations. Especially challenging were the frequently overlapping time intervals, which limited the usable reports to 34. Data used was not attenuation corrected to avoid e.g. unrealistically high Z_{DR}-columns by over-correcting Z_{DR}. Less noisy results and a higher correlation might be achievable by repeating the investigation with more data of higher quality, and with attenuation correction. Also, by using multiple, overlapping radars, polarimetric variables can be checked for consistency in overlapping areas (similar to the approach in chapter 3, section 3.4.1). This also reduces the risk of over-correction of attenuation.

A strong, linear relation between maximum Z_{DR} inside the Z_{DR}-column, Z_{DR}-column height above the melting layer and hail diameter on the ground can be formulated. The relation has a multiple correlation coefficient R of 0.820, which was tested successfully for significance ($F = 31.77 >> F_{\text{crit}} = 5.37, \text{for } \kappa = 0.01$). Also, a weaker, but still significant linear relation between maximum Z_{DR} inside the Z_{DR}-column, Z_{DR}-column height above the melting layer and lead time was found ($R = 0.542,\ F = 6.46 > F_{\text{crit}} = 5.37, \text{for } \kappa = 0.01$).

The prediction scheme is based on the correlation between maximum Z_{DR} inside the Z_{DR}-column, Z_{DR}-column height above the melting layer and observed hail diameter on the ground and is affected by the same errors and noise as discussed before. This affects not only determining the size, but also the predicted lead time, as a dependency between the size and lead time is used (see subsection 5.3.1). Therefore, predictions made by this method might be wrong in both time and size, if the size prediction fails. The fuzzy logic approach mitigates some noise and accounts for overlapping hail size categories (Liu and Chandrasekar, 2000). Again, this method can be improved with a larger amount of data.

Although thresholds and parameters for the detection scheme were based on educated guesses and experimentation with the data, the scheme works well and scored high during evaluation. Hail is difficult to detect for hail-bearing cells on

the edge of the radar range and for those precipitating hail already on entering the radar range, because the detection scheme requires a tracked cell to have a Z_{DR}-column observed for at least 15 min before larger hail can be issued. However, a 3D-composite of multiple, overlapping radars might solve this problem.

A third scheme, an alternative to the introduced detection scheme, based on the correlation between hail diameter and lead time, was developed, too. If an attenuation spike occurs, the time lag to the last, preceding spike of Z_{DR}-column height spike is used to obtain a hail size according to the insights from section 5.2.2, i.e. the dependency between hail size and lead time. This method, however, missed nearly half of all reports and was discarded. Instead, the detection scheme became more complex to first check the updraft capabilities and then hail fall indicators. The dependency between hail size and lead time was not observed in other studies (e.g. Kumjian et al., 2014; Ilotoviz et al., 2018), and should be assessed with more data for further validation.

The nowcasting examples shown did not require advection of cells to nowcast for future development. Operational nowcasting needs to predict cell movement and development. The detection and prediction scheme attribute their results to the whole 40 dBZ contour of the tracked cells, where hail did not necessarily occur everywhere. The question whether these areas are too big or not, could not be evaluated, because of the limited nature of the ground truth. Hail reports are only single-point observations and can neither cover an entire area, nor exclude an area of hail, as no reports of no-hail exist. Also, hail reports are more often issued in urban areas and more seldom in rural areas (Witt et al., 1998b; Frisbie, 2006). Lastly, prediction of hail landing locations is difficult (Ortega et al., 2016; Kennedy and Detwiler, 2003) and hail trajectories are still up to research (Dennis and Kumjian, 2017; Adams-Selin and Heymsfield, 2019; Kumjian and Lombardo, 2020).

The evaluation and scoring process was thoroughly designed, however some improvements need to be discussed. First, false alarms could not be properly assessed as there are no reports for no-hail. Therefore, a predictor which always warns for hail would score a lot better. To make the scoring results more comprehensible, a random prediction was applied to compare the two physical-based schemes with. The probabilities for the random prediction were taken from the reports, which were used for evaluation, too. Thus, an advantage in favor of the random prediction was expected. Nevertheless, with more than 84 % correct hail prediction/detection both physical-based schemes performed better than the random prediction (around 40 % correct prediction of hail). Secondly, less strict categories to evaluate might be more useful. Sometimes the difference between prediction and observation was 1 cm or less. But as categories differ e.g. between 4.5 cm and 5.0 cm, these cases are evaluated as wrong diameters. Third, the evaluation involved events which were discarded for estimating the lead time statistics. At least one of these events (13.04.2016, radar Isen) showed problems with the radar data and should have been excluded from the evaluation, too. Generally, the evaluation process is highly dependent on ground

truth. The ESWD does cross-check every report and assign quality classes for each. Still, wrong reports may impose a not assessed source of errors.

Attenuation inhibited the Z_{DR}-column detection or reduced their intensity in some cases. Overlapping radars might be able to mitigate the problem, if unattenuated data from another radar is available for the attenuated area. However, this is not always possible, e.g. at the edge of a radar network. K_{DP}-columns are expected to still provide information in cases where Z_{DR}-columns are inhibited by attenuation (Kumjian and Ryzhkov, 2008; van Lier-Walqui et al., 2016), because K_{DP} is dependent on the phase. However, K_{DP} was very noisy in the data analyzed and suffered from the limitation in range resolution of 1 km. Moreover, K_{DP} is strongly affected by resonance effects at C band for hail of and above 4 cm diameter (Figure 5.24). K_{DP} for wet hail is positive only for narrow diameter ranges (11 mm to 16 mm, 27 mm to 31 mm, and 39 mm to 40 mm) in the limited simulation shown here. Other simulations confirm the general tendency of negative K_{DP} for hail diameters larger than a resonance size, e.g. 4 cm (Ryzhkov et al., 2013a; Ryzhkov and Zrnic, 2019). Values for dry hail at C band can be twice as high as at S band for the range 15 mm to 24 mm. For diameters above 1.6 cm K_{DP} at C band becomes negative in these simulations. K_{DP}-columns seem to appear after Z_{DR}-columns, as they are related to downbursts and strong precipitation (Fridlind et al., 2019). Thus, achievable lead time would be shorter when using K_{DP}-columns instead of Z_{DR}-columns.

High K_{DP} is suspected to indicate small, melting hail (Kumjian et al., 2019). In 14 out of the 16 analyzed cases K_{DP} above $10\,^{\circ}\,\mathrm{km}^{-1}$ was observed in the core of convective cells, accompanying reflectivity factors above 50 dBZ, and four events exhibited K_{DP} values of and above $15\,^{\circ}\,\mathrm{km}^{-1}$. These enhanced K_{DP} values occurred more than 10 min before giant hail - and in one case accumulated small hail - was reported at the ground. Since negative K_{DP} is expected for large hail diameters, the presence of large rain drops or small hail is suspected to dominate the signal in these cases. In addition, ground reports tend to emphasize larger hail sizes, and thus high K_{DP} may not correlate well with hail surface reports.

Columns of circular depolarization ratio are another proposed hail precursor (Ryzhkov et al., 2017). However, as CDR is not directly measured by radars using simultaneous transmission and reception, it has to be estimated. Ryzhkov et al. (2017) proposed a method to calculate a CDR proxy, depolarization ratio DR (see 2.1.2). DR requires linear depolarization ratio LDR, which is not observed for the DWD radar network due to simultaneous transmission and reception. Attempts to mitigate the missing LDR, by e.g. assuming it based on other variables, failed. Therefore, an investigation of hail precursors capabilities of CDR and DR at C band could not be pursued.

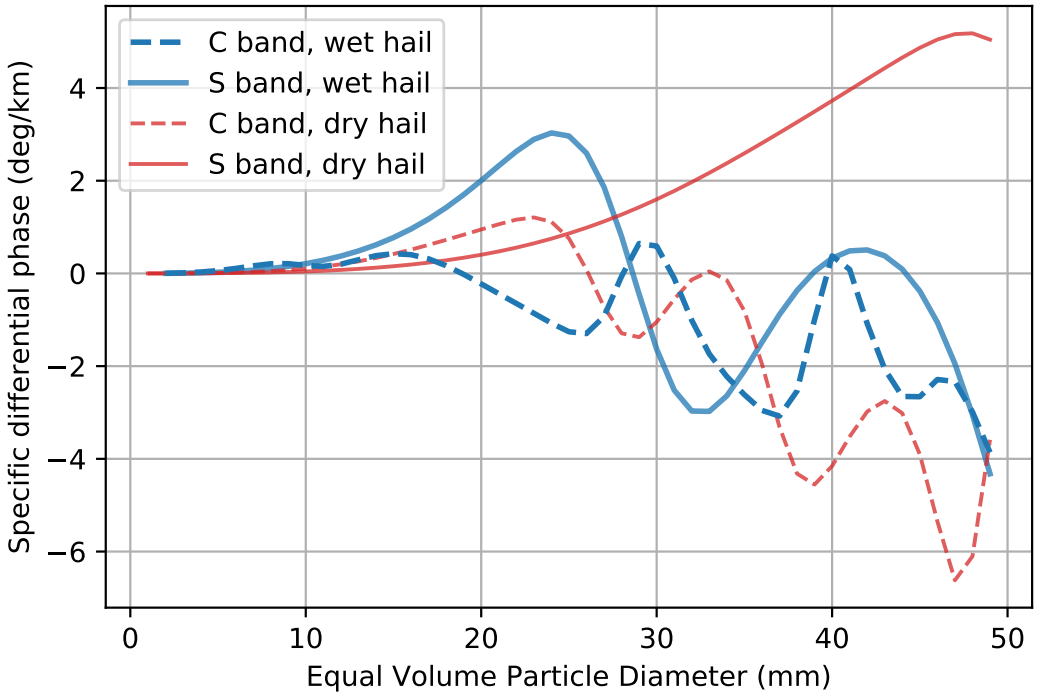

FIGURE 5.24: T-matrix scattering simulation of specific differential phase K_{DP} for water coated ice particles ("wet hail", blue) and ice particles ("dry hail", red) at S (solid lines) and C band (dashed lines). The dieletric constants for water and ice are calculated for 0 °C and axis-ratio of the simulated, oblate ellipsoid is 0.75 for all diameters. The width of canting angle distribution is 40°. Simulations are in line with Ryzhkov et al. (2010).

5.6 Summary and Conclusion

Methods to detect hail aloft, discriminate between size categories and techniques to predict hail while growing within a storm have been described and evaluated. 16 hail bearing storms monitored by the polarimetric C-band radar network of DWD in the years 2013 - 2016 together with hail reports from the European Severe Weather Database (ESWD) were investigated in order to examine hail precursors and their nowcasting capabilities. Z_{DR}-columns were proven to indicate hail growth and to provide lead times for warnings. High attenuation served as an indicator for hail aloft, which also allows locating hail reports in time better, when only uncertain time intervals were reported. In line with expectations Z_{DR}-columns, possibly indicating updrafts, precede high signal attenuation (α-spikes) indicating hail. From the 165 ground reports 34 could be used for lead time estimates.

A significant correlation between Z_{DR}-column properties and final hail diameter was determined. This allows to predict hail 10 min to 20 min before hail occurrence on the ground, which was exploited for a prediction scheme.

A hail detection scheme was developed based on observing temporal behavior of Z_{DR}-columns and attenuation coefficient α. Updraft conditions of current and past time steps within a tracked cell are reviewed first. Then hail fall indicators, such

as sudden intensification of attenuation or Z_{DR}-column collapses, are exploited to approve the detection.

A first evaluation yielded very good results for both detection and prediction of hail. The discrimination of hail size was also evaluated with good results for both detection and prediction. In comparison with random predictions, for which probabilities are taken from the reports used for evaluation, detection and prediction schemes outperformed the random predictions.

Chapter 6

Summary and Conclusion

Detection and nowcasting of hail and particularly its size has been investigated. In this chapter the research questions formulated in chapter 1 are addressed in view of the findings presented in this thesis.

Precipitation radar observations are the most important information source for detecting hail aloft. The polarimetric C-band radar network has been used as primary information source in this thesis, together with hail occurrence reports from the European Severe Weather Database (ESWD).

Techniques for correcting attenuation introduced by Testud et al. (2000), Gu et al. (2011) and Ryzhkov et al. (2013b) were extended for attenuation correction at C band during precipitation of hail. The attenuation correction methodology was successfully evaluated with observations of four overlapping C-band radars in 16 events.

T-matrix scattering simulations have been used to adjust a hail size discrimination algorithm (HSDA) developed for S-band radars for usage at C band. New parameters for the membership functions of the fuzzy-logic based HSDA were obtained. Further experiments with unsupervised learning methods were conducted to improve the HSDA.

Nowcasting methods were developed to detect hail aloft, discriminate between size categories and to predict hail occurrence before impact on the ground. Z_{DR}-columns were proven to indicate hail growth, resulting in usable lead times for warnings. A linear relation between Z_{DR}-column properties and observed hail diameter on the ground was exploited for hail occurrence and hail size nowcasting with lead times between 10 min to 20 min. The relation was tested positively for statistical significance. In addition to the nowcasting algorithm, a hail detection and size discrimination algorithm was developed, exploiting peaks in the time series of Z_{DR}-column evolution and attenuation intensification.

How accurately can the location and size of hail be determined from polarimetric C-band radar observations and what additional information from other sources is required?

The location accuracy ranges from a few kilometers up to 30 km depending on the size of the tracked cell. A more accurate landing location is still a difficult task and subject of ongoing research (Ortega et al., 2016), partially because no surface reports

of "no hail" are available. A dense network of disdrometers could be exploited for such a measure.

Hail size was detected with 65 % accuracy using the detection scheme. More research and observations might further improve this score. The prediction scheme successfully discriminates hail size with 53 % accuracy and allows nowcasting with lead times between 10 and 20 min. Radar observations with higher resolution in space and time would improve this figure. Genuine RHIs or polarimetric, phased-array radars could provide sufficiently high resolutions.

Besides the polarimetric radar data, the algorithm requires the melting layer height. In this study, *in-situ* measurements from soundings were used, but also polarimetric radar themselves could be used (Baldini and Gorgucci, 2006; Giangrande et al., 2008; Wolfensberger et al., 2015).

What are the most robust precursors for large hail, how can they be exploited for nowcasting and which lead times can be achieved?

Three hail precursor candidates were investigated: columnar enhanced areas of Z_{DR}, K_{DP} and CDR. All three relate to updrafts and thus potential hail fall (Kumjian et al., 2014; Hubbert et al., 1998; Ryzhkov et al., 2014).

It is well documented that Z_{DR}-columns intensify prior to hail occurrence (Picca et al., 2010; Kumjian et al., 2014; Snyder et al., 2015), with an expected, positive time lag of around 15 min between intensification of Z_{DR}-columns and hail occurrence. Observational evidence of this behavior has been provided in this study. However, Z_{DR}-column detection can be affected by attenuation and even inhibited, when hail shafts, e.g. of other cells, are closer to the radar than updraft regions. Despite the effect of attenuation on Z_{DR}-column retrievals, a lead time of 10 min to 20 min is possible with 88 % correct prediction of hail and 53 % correct prediction of hail with size discrimination.

K_{DP}-columns could partially replace or complement Z_{DR}-columns in high attenuated cases (Kumjian and Ryzhkov, 2008; van Lier-Walqui et al., 2016). Except for supercell thunderstorms, Z_{DR}-columns and K_{DP}-columns appear to be collocated (Zrnić et al., 2001; Loney et al., 2002), but Fridlind et al. (2019) show several cases with K_{DP}-columns following Z_{DR}-columns with a delay, thereby reducing potential lead times. No clear-cut cases of K_{DP}-column development could be observed in this study, which might be related to inherent C band properties. Also, stronger resonance effects, which only allow positive K_{DP} for small hail and some specific hail diameters (see Figure 5.2) could be a reason. Especially giant, wet hail appears to have only negative K_{DP} values (Ryzhkov and Zrnic, 2019). Furthermore, the coarse spatial resolution of DWD's volumetric radar data and noisy Φ_{DP} might have limited the success of the K_{DP} analysis. For these reasons, K_{DP}-columns might not be robust at C band at all, as they are difficult to obtain and require low noise and high resolution data.

CDR-columns might be an even better hail precursor since signals are stronger, more robust, and could be visible in greater heights than e.g. Z_{DR}-columns (Ryzhkov et al., 2017). CDR is not available for most radars as these operate in simultaneous transmission / reception mode, unless complex Voltages of the returned signal are available (Ryzhkov et al., 2014). Although methods to obtain an estimate of CDR have been elaborated (Ryzhkov et al., 2017), LDR is required. Unfortunately, LDR is not observed by the radar network used in this study. Therefore, CDR-columns could not be observed in this thesis.

In terms of robustness, K_{DP} columns are not affected by attenuation and therefore might be most robust, at least at S band. This feature does not seem to hold at C band. Also, CDR-columns appear to be much more prominent and taller than columns of Z_{DR}. However, LDR was not available, therefore CDR could not be estimated and tested for robustness. In the data available and for the desired operational purposes, without changing radar parameters, Z_{DR}-columns are the most robust precursors for large hail at C band. They can improve the lead time by 10 min for small, 15 min for large and 20 min for giant hail.

List of Abbreviations

CSI	**C**ritical **S**uccess **I**ndex
DWD	*Deutscher WetterDienst* (German national meteorological service)
FAR	**F**alse-**A**larm **R**atio
HCA	**H**ydrometeor **C**lassification **A**lgorithm
HSDA	**H**ail **S**ize **D**iscrimination **A**lgorithm
ML	**M**elting **L**ayer
MRR	**M**icro **R**ain **R**adar
NWP	**N**umerical **W**eather **P**rediction
OHS	**O**utside (of) **H**ot **S**pots
PIA	two-way **P**ath-**I**ntegrated **A**ttenuation
POD	**P**robability **O**f **D**etection
PPI	**P**lane **P**osition **I**ndicator
RHI	**R**ange **H**eight **I**ndicator
RMSE	**R**oot **M**ean **S**quare **E**rror
UTC	**C**oordinated **U**niversal **T**ime
WC	**W**eighted **C**entroid distance
WPA	**W**eighted **P**airwise **A**verage distance
ZCH	Z_{DR}-**C**olumn **H**eight above the melting layer

List of Symbols

A_h	specific horizontal attenuation	$\mathrm{dB\,km^{-1}}$
C_{dr}	circular depolarization ratio in linear scale	1
CDR	circular depolarization ratio in logarithmic scale	dB
D	particle diameter	mm
D_r	depolarization ratio (proxy for C_{dr})	1
DR	depolarization ratio (proxy for CDR)	dB
$\vec{E}_i$	incident electromagnetic wave	$\mathrm{V\,m^{-1}}$
$\vec{E}_s$	scattered electromagnetic wave	$\mathrm{V\,m^{-1}}$
F	ratio between explained and unexplained variance	1
F_{crit}	critical value of F	1
G_i	fuzzy logic aggregation value	1
k	wavenumber of background medium	$\mathrm{1/m}$
K_{DP}	specific differential phase	$^\circ\,\mathrm{km^{-1}}$
L_{dr}	linear depolarization ratio in linear scale	1
M_i	ith angular moment	1
LDR	linear depolarization ratio in logarithmic scale	$^\circ\,\mathrm{km^{-1}}$
N	particle size distribution	$\mathrm{m^{-3}\,mm^{-1}}$
O_j	overlap penalty vector for the jth polarimetric variable	1
Q_j	confidence vector for the jth polarimetric variable	1
R	multiple correlation coefficient	1
r_i	range gate with index i	m
$\bar{\bar{S}}$	(back)scattering matrix	1
s_a s_b $s_a^{(0)}$ $s_b^{(0)}$	complex scattering amplitudes of individual particles, along their major (b) or minor (a) axes. $^{(0)}$ in superscript denotes forward-scattering, otherwise it is backscattering.	1
S_{HH} S_{VV} S_{HV} S_{VH} $S_{HH}^{(0)}$ $S_{VV}^{(0)}$	scattering amplitudes; the subscripts indicate which channel (H for horizontal and V for vertical polarization) transmits (first subscript) and which receives (second subscript). $^{(0)}$ in superscript denotes forward-scattering, otherwise it is backscattering.	1
z_a	attenuated reflectivity factor in linear unity	$\mathrm{mm^6/m^3}$

Z_h	horizontal reflectivity factor	dBZ
z_h	horizontal reflectivity factor in linear units	$\mathrm{mm}^6/\mathrm{m}^3$
Z_{DR}	differential reflectivity	dB
Z_{dr}	differential reflectivity in linear scale	1
Z_v	vertical reflectivity factor	dBZ
z_v	vertical reflectivity factor in linear units	$\mathrm{mm}^6/\mathrm{m}^3$
α	attenuation coefficient	$\mathrm{dB}/^\circ$
α_0	background attenuation coefficient	$\mathrm{dB}/^\circ$
$\Delta\alpha$	hot spot attenuation coefficient increment	$\mathrm{dB}/^\circ$
δ	backscatter differential phase	$^\circ$
ϵ_0	dielectric constant in vacuum	$8.854 \times 10^{-12}\,\mathrm{F\,m^{-1}}$
ϵ_w	complex dielectric constant of water	$\mathrm{F\,m^{-1}}$
η	relative error reduction	1
γ	axis-ratio	1
κ	significance level	1
λ	(radar) wavelength	m
ϕ_{DP}	propagation differential phase	$^\circ$
Φ_{DP}	total differential phase	$^\circ$
ψ	canting angle	$^\circ$
ρ	Pearson correlation coefficient	1
ρ_{hv}	cross-polar correlation coefficient	1
σ_ψ	standard deviation of canting angle distribution	$^\circ$
ς	tracking likelihood estimator	1
ξ	spatial mean of radar RMSE	$\mathrm{dB\,km^{-2}}$

List of Figures

List of Tables

Bibliography

Abadi, M., A. Agarwal, P. Barham, E. Brevdo, Z. Chen, C. Citro, G. S. Corrado, A. Davis, J. Dean, M. Devin, and Coauthors, 2015: Tensorflow: Large-scale machine learning on heterogeneous systems, 2015. *Software available from tensorflow. org*, **1 (2)**.

Adams-Selin, R., and A. J. Heymsfield, 2019: Sensitivity of hail trajectories and size to embryo location, size, and density. *18th Conference on Mesoscale Processes*, AMS.

Adams-Selin, R. D., and C. L. Ziegler, 2016: Forecasting hail using a one-dimensional hail growth model within WRF. *Monthly Weather Review*, **144 (12)**, 4919–4939, doi:10.1175/mwr-d-16-0027.1.

Anderson, M. E., L. D. Carey, W. A. Petersen, and K. R. Knupp, 2011: C-band dual-polarimetric radar signatures of hail. *Electron. J. Oper. Meteor*, **12 (2)**, 1–30.

Aydin, K., T. A. Seliga, and V. Balaji, 1986: Remote Sensing of Hail with a Dual Linear Polarization Radar. *Journal of Climate and Applied Meteorology*, **25 (10)**, 1475–1484, doi:10.1175/1520-0450(1986)025<1475:RSOHWA>2.0.CO;2, URL http://journals.ametsoc.org/doi/abs/10.1175/1520-0450(1986)025%3C1475:RSOHWA%3E2.0.CO%3B2.

Baldini, L., and E. Gorgucci, 2006: Identification of the melting layer through dual-polarization radar measurements at vertical incidence. *Journal of Atmospheric and Oceanic Technology*, **23 (6)**, 829–839, doi:10.1175/jtech1884.1.

Besic, N., J. Figueras i Ventura, J. Grazioli, M. Gabella, U. Germann, and A. Berne, 2016: Hydrometeor classification through statistical clustering of polarimetric radar measurements: a semi-supervised approach. *Atmospheric Measurement Techniques*, **9**, 4425–45.

Blahak, U., 2016: 'radarmielm and radarmielib – calculation of radar reflectivity from model output. COSMO technical report no. 28, Consortium for Small Scale Modeling. URL http://www.cosmo-model.org/content/model/documentation/techReports/docs/techReport28.pdf.

Borowska, L., A. Ryzhkov, D. Zrnić, C. Simmer, and R. Palmer, 2011: Attenuation and differential attenuation of 5-cm-wavelength radiation in melting hail. *Journal of Applied Meteorology and Climatology*, **50 (1)**, 59–76, doi:10.1175/2010jamc2465.1, URL http://dx.doi.org/10.1175/2010JAMC2465.1.

Brewster, K. A., 2003: Phase-correcting data assimilation and application to storm-scale numerical weather prediction. part i: Method description and simulation testing. *Monthly Weather Review*, **131 (3)**, 480–492, doi:10.1175/1520-0493(2003)131<0480:pcdaaa>2.0.co;2.

Bringi, V., T. Keenan, and V. Chandrasekar, 2001: Correcting c-band radar reflectivity and differential reflectivity data for rain attenuation: a self-consistent method with constraints. *IEEE Transactions on Geoscience and Remote Sensing*, **39 (9)**, 1906–1915, doi:10.1109/36.951081.

Bringi, V. N., and V. Chandrasekar, 2001: *Polarimetric Doppler Weather Radar: Principles and Applications*. Cambridge University Press.

Bringi, V. N., V. Chandrasekar, N. Balakrishnan, and D. S. Zrnić, 1990: An examination of propagation effects in rainfall on radar measurements at microwave frequencies. *Journal of Atmospheric and Oceanic Technology*, **7 (6)**, 829–840, doi:10.1175/1520-0426(1990)007<0829:aeopei>2.0.co;2.

Bringi, V. N., T. A. Seliga, and K. Aydin, 1984: Hail detection with a differential reflectivity radar. *Science*, **225 (4667)**, 1145–1147, doi:10.1126/science.225.4667.1145, URL http://dx.doi.org/10.1126/science.225.4667.1145.

Browning, K. A., 1964: Airflow and precipitation trajectories within severe local storms which travel to the right of the winds. *Journal of the Atmospheric Sciences*, **21 (6)**, 634–639, doi:10.1175/1520-0469(1964)021<0634:aaptws>2.0.co;2.

Bunkers, M. J., M. R. Hjelmfelt, and P. L. Smith, 2006: An observational examination of long-lived supercells. part i: Characteristics, evolution, and demise. *Weather and Forecasting*, **21 (5)**, 673–688, doi:10.1175/waf949.1.

Chollet, F., and Coauthors, 2015: Keras. GitHub, https://keras.io.

Cintineo, R. M., and D. J. Stensrud, 2013: On the predictability of supercell thunderstorm evolution. *Journal of the Atmospheric Sciences*, **70 (7)**, 1993–2011, doi:10.1175/jas-d-12-0166.1.

Cole, K. S., and R. H. Cole, 1941: Dispersion and absorption in dielectrics i. alternating current characteristics. *The Journal of chemical physics*, **9 (4)**, 341–351, doi:10.1063/1.1750906.

Davidson, T. R., L. Falorsi, N. De Cao, T. Kipf, and J. M. Tomczak, 2018: Hyperspherical variational auto-encoders. *arXiv preprint arXiv:1804.00891*.

Dennis, E. J., and M. R. Kumjian, 2017: The impact of vertical wind shear on hail growth in simulated supercells. *Journal of the Atmospheric Sciences*, **74 (3)**, 641–663, doi:10.1175/jas-d-16-0066.1.

Depue, T. K., P. C. Kennedy, and S. A. Rutledge, 2007: Performance of the hail differential reflectivity (h DR) polarimetric radar hail indicator. *Journal of Applied Meteorology and Climatology*, **46 (8)**, 1290–1301, doi:10.1175/jam2529.1, URL http://dx.doi.org/10.1175/JAM2529.1.

Dixon, M., and G. Wiener, 1993: TITAN: Thunderstorm identification, tracking, analysis, and nowcasting—a radar-based methodology. *Journal of Atmospheric and Oceanic Technology*, **10 (6)**, 785–797, doi:10.1175/1520-0426(1993)010<0785:ttitaa>2.0.co;2.

Dolan, B., and S. A. Rutledge, 2009: A theory-based hydrometeor identification algorithm for x-band polarimetric radars. *Journal of Atmospheric and Oceanic Technology*, **26 (10)**, 2071–2088, doi:10.1175/2009jtecha1208.1, URL https://doi.org/10.1175%2F2009jtecha1208.1.

Doswell, C. A., R. Davies-Jones, and D. L. Keller, 1990: On summary measures of skill in rare event forecasting based on contingency tables. *Weather and Forecasting*, **5 (4)**, 576–585, doi:10.1175/1520-0434(1990)005<0576:osmosi>2.0.co;2.

Dotzek, N., P. Groenemeijer, B. Feuerstein, and A. M. Holzer, 2009: Overview of ESSL's severe convective storms research using the european severe weather database ESWD. *Atmospheric Research*, **93 (1-3)**, 575–586, doi:10.1016/j.atmosres.2008.10.020.

Doviak, R. J., and D. S. Zrnic, 2006: *Doppler radar and weather observations*. Courier Corporation.

Eccles, P. J., and D. Atlas, 1973: A Dual-Wavelength Radar Hail Detector. *Journal of Applied Meteorology*, **12 (5)**, 847–854, doi:10.1175/1520-0450(1973)012<0847:ADWRHD>2.0.CO;2, URL http://journals.ametsoc.org/doi/abs/10.1175/1520-0450(1973)012%3C0847:ADWRHD%3E2.0.CO;2.

Edwards, A., 1979: *Multiple Regression and the Analysis of Variance and Covariance*. Books in psychology, W. H. Freeman, URL https://openlibrary.org/books/OL4409524M/.

Evaristo, R., T. Bals-Elsholz, E. Williams, A. J. Fenn, M. Donovan, and D. Smalley, 2013: Relationship of graupel shape to differential reflectivity: theory and observations. *29th Conference on Environmental Information Processing Technologies, Austin, USA*.

Frech, M., 2014: The effect of a wind power plant in radar data. *Abstract of 8th European Conference on Radar in Meteorology and Hydrology*.

Frech, M., M. Hagen, and T. Mammen, 2017: Monitoring the absolute calibration of a polarimetric weather radar. *Journal of Atmospheric and Oceanic Technology*, **34 (3)**, 599–615, doi:10.1175/jtech-d-16-0076.1.

Frech, M., and J. Seltmann, 2017: The influence of wind turbines on dualpol radar moments and products. *38th Conference on Radar Meteorology, AMS, Chicago, IL, 28 Aug. 2017*.

Fridlind, A. M., M. van Lier-Walqui, S. Collis, S. E. Giangrande, R. C. Jackson, X. Li, T. Matsui, R. Orville, M. H. Picel, D. Rosenfeld, A. Ryzhkov, R. Weitz, and P. Zhang, 2019: Use of polarimetric radar measurements to constrain simulated convective cell evolution: a pilot study with lagrangian tracking. *Atmospheric Measurement Techniques*, **12 (6)**, 2979–3000, doi:10.5194/amt-12-2979-2019.

Frisbie, P., 2006: The population bias of severe weather reports west of the continental divide. *National Weather Digest*, **30**, 11–16.

Giangrande, S. E., J. M. Krause, and A. V. Ryzhkov, 2008: Automatic designation of the melting layer with a polarimetric prototype of the WSR-88d radar. *Journal of Applied Meteorology and Climatology*, **47 (5)**, 1354–1364, doi:10.1175/2007jamc1634.1.

Grazioli, J., D. Tuia, and A. Berne, 2015: Hydrometeor classification from polarimetric radar measurements: a clustering approach. *Atmospheric Measurement Techniques*, **8 (1)**, 149.

Gu, J.-Y., A. Ryzhkov, P. Zhang, P. Neilley, M. Knight, B. Wolf, and D.-I. Lee, 2011: Polarimetric attenuation correction in heavy rain at c band. *Journal of Applied Meteorology and Climatology*, **50 (1)**, 39–58, doi:10.1175/2010jamc2258.1, URL http://dx.doi.org/10.1175/2010JAMC2258.1.

Halkidi, M., Y. Batistakis, and M. Vazirgiannis, 2002: Clustering validity checking methods. *ACM SIGMOD Record*, **31 (3)**, 19, doi:10.1145/601858.601862.

Heistermann, S., M.; Jacobi, and T. Pfaff, 2013: Technical note: An open source library for processing weather radar data (wradlib). *Hydrol. Earth Syst. Sci.*, **17**, 863–871, doi:10.5194/hess-17-863-2013.

Helmert, K., P. Tracksdorf, J. Steinert, M. Werner, M. Frech, N. Rathmann, T. Hengstebeck, M. Mott, S. Schumann, and T. Mammen, 2014: Dwds new radar network and post-processing algorithm chain. *Proc. Eighth European Conf. on Radar in Meteorology and Hydrology (ERAD 2014), Garmisch-Partenkirchen, Germany, DWD and DLR*, Vol. 4.

Hering, A., C. Morel, G. Galli, S. Sénési, P. Ambrosetti, and M. Boscacci, 2004: Nowcasting thunderstorms in the alpine region using a radar based adaptive thresholding scheme. *Proceedings of ERAD*, Vol. 1.

Hubbert, J., V. N. Bringi, L. D. Carey, and S. Bolen, 1998: CSU-CHILL polarimetric radar measurements from a severe hail storm in eastern colorado. *Journal of Applied Meteorology*, **37 (8)**, 749–775, doi:10.1175/1520-0450(1998)037<0749:ccprmf>2.0.co;2.

Hubbert, J. C., M. Dixon, and S. M. Ellis, 2009: Weather radar ground clutter. part II: Real-time identification and filtering. *Journal of Atmospheric and Oceanic Technology*, **26 (7)**, 1181–1197, doi:10.1175/2009jtecha1160.1.

Hunter, J. D., 2007: Matplotlib: A 2d graphics environment. *Computing in Science & Engineering*, **9**, 90–95, doi:10.1109/MCSE.2007.55.

Ilotoviz, E., A. Khain, A. V. Ryzhkov, and J. C. Snyder, 2018: Relationship between aerosols, hail microphysics, and zdr columns. *Journal of the Atmospheric Sciences*, **75 (6)**, 1755–1781, doi:10.1175/jas-d-17-0127.1.

James, P. M., B. K. Reichert, and D. Heizenreder, 2018: NowCastMIX: Automatic integrated warnings for severe convection on nowcasting time scales at the german weather service. *Weather and Forecasting*, **33 (5)**, 1413–1433, doi:10.1175/waf-d-18-0038.1.

Jung, Y., M. Xue, and G. Zhang, 2010: Simulations of polarimetric radar signatures of a supercell storm using a two-moment bulk microphysics scheme. *Journal of Applied Meteorology and Climatology*, **49 (1)**, 146–163, doi:10.1175/2009jamc2178.1.

Kaltenboeck, R., and A. Ryzhkov, 2013: Comparison of polarimetric signatures of hail at s and c bands for different hail sizes. *Atmospheric Research*, **123**, 323–336, doi:10.1016/j.atmosres.2012.05.013, URL http://dx.doi.org/10.1016/j.atmosres.2012.05.013.

Keil, C., and G. C. Craig, 2007: A displacement-based error measure applied in a regional ensemble forecasting system. *Monthly Weather Review*, **135 (9)**, 3248–3259, doi:10.1175/mwr3457.1.

Kennedy, P. C., and A. G. Detwiler, 2003: A case study of the origin of hail in a multicell thunderstorm using in situ aircraft and polarimetric radar data. *Journal of Applied Meteorology*, **42 (11)**, 1679–1690, doi:10.1175/1520-0450(2003)042<1679:acsoto>2.0.co;2.

Kennedy, P. C., S. A. Rutledge, W. A. Petersen, and V. N. Bringi, 2001: Polarimetric Radar Observations of Hail Formation. *Journal of Applied Meteorology*, **40 (8)**, 1347–1366, doi:10.1175/1520-0450(2001)040<1347:PROOHF>2.0.CO;2, URL http://journals.ametsoc.org/doi/abs/10.1175/1520-0450(2001)040%3C1347%3APROOHF%3E2.0.CO%3B2.

Kong, F., Y. Zhang, and R. D. Palmer, 2013: Wind turbine radar interference studies by polarimetric measurements of a scaled model. *IEEE Transactions on Aerospace and Electronic Systems*, **49 (3)**, 1589–1600, doi:10.1109/taes.2013.6558006.

Königsberger, K., 2013: *Analysis 2*. Springer-Verlag.

Kumjian, M., 2013: Principles and applications of dual-polarization weather radar. part i: Description of the polarimetric radar variables. *Journal of Operational Meteorology*, **1 (19)**, 226–242, doi:10.15191/nwajom.2013.0119.

Kumjian, M., and K. Lombardo, 2020: Influences on hail size as inferred from hailstone growth trajectory model calculations. *100th American Meteorological Society Annual Meeting*, AMS.

Kumjian, M. R., S. M. Ganson, and A. V. Ryzhkov, 2012: Freezing of raindrops in deep convective updrafts: A microphysical and polarimetric model. *Journal of the Atmospheric Sciences*, **69 (12)**, 3471–3490, doi:10.1175/jas-d-12-067.1, URL http://dx.doi.org/10.1175/JAS-D-12-067.1.

Kumjian, M. R., A. P. Khain, N. Benmoshe, E. Ilotoviz, A. V. Ryzhkov, and V. T. J. Phillips, 2014: The anatomy and physics of ZDR columns: Investigating a polarimetric radar signature with a spectral bin microphysical model. *Journal of Applied Meteorology and Climatology*, **53 (7)**, 1820–1843, doi:10.1175/jamc-d-13-0354.1, URL http://dx.doi.org/10.1175/JAMC-D-13-0354.1.

Kumjian, M. R., Z. J. Lebo, and A. M. Ward, 2019: Storms producing large accumulations of small hail. *Journal of Applied Meteorology and Climatology*, **58 (2)**, 341–364, doi:10.1175/jamc-d-18-0073.1.

Kumjian, M. R., and A. V. Ryzhkov, 2008: Polarimetric signatures in supercell thunderstorms. *Journal of Applied Meteorology and Climatology*, **47 (7)**, 1940–1961, doi:10.1175/2007jamc1874.1.

Labriola, J., N. Snook, Y. Jung, and M. Xue, 2019: Explicit ensemble prediction of hail in 19 may 2013 oklahoma city thunderstorms and analysis of hail growth processes with several multimoment microphysics schemes. *Monthly Weather Review*, **147 (4)**, 1193–1213, doi:10.1175/mwr-d-18-0266.1.

Leinonen, J., 2014: High-level interface to t-matrix scattering calculations: architecture, capabilities and limitations. *Optics Express*, **22 (2)**, 1655–1660, doi:10.1364/OE.22.001655, URL http://www.osapublishing.org/abstract.cfm?uri=oe-22-2-1655.

Liu, H., and V. Chandrasekar, 2000: Classification of hydrometeors based on polarimetric radar measurements: Development of fuzzy logic and neuro-fuzzy systems, and in situ verification. *Journal of Atmospheric and Oceanic Technology*, **17 (2)**, 140–164, doi:10.1175/1520-0426(2000)017<0140:cohbop>2.0.co;2.

Lomax, R. G., and D. L. Hahs-Vaughn, 2001: *Statistical Concepts: A Second Course for education and the behavioral sciences*. 2nd ed., Lawrence Erlbaum Associates, doi:10.4324/9781410605672.

Loney, M. L., D. S. Zrnić, J. M. Straka, and A. V. Ryzhkov, 2002: Enhanced polarimetric radar signatures above the melting level in a supercell storm. *Journal of Applied Meteorology*, **41 (12)**, 1179–1194, doi:10.1175/1520-0450(2002)041<1179:eprsat>2.0.co;2.

Lucarini, V., J. J. Saarinen, K.-E. Peiponen, and E. M. Vartiainen, 2005: *Kramers-Kronig relations in optical materials research*, Vol. 110. Springer Science & Business Media.

Matrosov, S. Y., 2004: Depolarization estimates from linear h and v measurements with weather radars operating in simultaneous transmission–simultaneous receiving mode. *Journal of Atmospheric and Oceanic Technology*, **21 (4)**, 574–583, doi:10.1175/1520-0426(2004)021<0574:DEFLHA>2.0.CO;2, URL http://journals.ametsoc.org/doi/abs/10.1175/1520-0426%282004%29021%3C0574%3ADEFLHA%3E2.0.CO%3B2.

Miller, L. J., J. D. Tuttle, and G. B. Foote, 1990: Precipitation production in a large montana hailstorm: Airflow and particle growth trajectories. *Journal of the Atmospheric Sciences*, **47 (13)**, 1619–1646, doi:10.1175/1520-0469(1990)047<1619:ppialm>2.0.co;2.

Miller, L. J., J. D. Tuttle, and C. A. Knight, 1988: Airflow and hail growth in a severe northern high plains supercell. *Journal of the Atmospheric Sciences*, **45 (4)**, 736–762, doi:10.1175/1520-0469(1988)045<0736:aahgia>2.0.co;2.

Mishchenko, M. I., 2000: Calculation of the amplitude matrix for a nonspherical particle in a fixed orientation. *Applied Optics*, **39 (6)**, 1026–1031, doi:10.1364/AO.39.001026, URL http://www.osapublishing.org/abstract.cfm?uri=ao-39-6-1026.

Mishchenko, M. I., and L. D. Travis, 1998: Capabilities and limitations of a current FORTRAN implementation of the t-matrix method for randomly oriented, rotationally symmetric scatterers. *Journal of Quantitative Spectroscopy and Radiative Transfer*, **60 (3)**, 309–324, URL http://www.sciencedirect.com/science/article/pii/S0022407398000089.

Mishchenko, M. I., L. D. Travis, and D. W. Mackowski, 1996: T-matrix computations of light scattering by nonspherical particles: a review. *Journal of Quantitative Spectroscopy and Radiative Transfer*, **55 (5)**, 535–575, URL http://www.sciencedirect.com/science/article/pii/0022407396000027.

Novák, V., I. Perfilieva, and J. Močkoř, 1999: Mathematical principles of fuzzy logic. Kluwer, Boston.

Ortega, K. L., J. M. Krause, and A. V. Ryzhkov, 2016: Polarimetric radar characteristics of melting hail. part III: Validation of the algorithm for hail size discrimination. *J. Appl. Meteor. Climatol.*, **55 (4)**, 829–848, doi:10.1175/jamc-d-15-0203.1, URL http://dx.doi.org/10.1175/JAMC-D-15-0203.1.

Ortega, K. L., T. M. Smith, K. L. Manross, K. A. Scharfenberg, A. Witt, A. G. Kolodziej, and J. J. Gourley, 2009: The severe hazards analysis and verfication experiment. *Bulletin of the American Meteorological Society*, **90 (10)**, 1519–1530, doi:10.1175/2009bams2815.1.

Park, H. S., A. V. Ryzhkov, D. S. Zrnić, and K.-E. Kim, 2009: The hydrometeor classification algorithm for the polarimetric WSR-88d: Description and application to an MCS. *Weather and Forecasting*, **24 (3)**, 730–748, doi:10.1175/2008WAF2222205.1, URL http://journals.ametsoc.org/doi/abs/10.1175/2008WAF2222205.1.

Pérez, F., and B. E. Granger, 2007: IPython: a system for interactive scientific computing. *Computing in Science and Engineering*, **9 (3)**, 21–29, doi:10.1109/MCSE.2007.53, URL http://ipython.org.

Picca, J., M. Kumjian, and A. Ryzhkov, 2010: Zdr columns as a predictive tool for hail growth and storm evolution. 25th conf. on severe local storms, denver, co. *Amer. Meteor. Soc*, **11**.

Prodi, F., 1970: Measurements of local density in artificial and natural hailstones. *Journal of Applied Meteorology*, **9 (6)**, 903–910, doi:10.1175/1520-0450(1970)009<0903:moldia>2.0.co;2.

Púčik, T., C. Castellano, P. Groenemeijer, T. Kühne, A. T. Rädler, B. Antonescu, and E. Faust, 2019: Large hail incidence and its economic and societal impacts across europe. *Monthly Weather Review*, **147 (11)**, 3901–3916, doi:10.1175/mwr-d-19-0204.1.

Rinehart, R. E., 2004: *Radar for Meteorologists*. Rinehart, URL https://openlibrary.org/books/OL8531155M/Radar_for_Meteorologists.

Ryzhkov, A., M. Pinsky, A. Pokrovsky, and A. Khain, 2010: Polarimetric radar observation operator for a cloud model with spectral microphysics. *Journal of Applied Meteorology and Climatology*, **50 (4)**, 873–894, doi:10.1175/2010JAMC2363.1, URL http://journals.ametsoc.org/doi/abs/10.1175/2010JAMC2363.1.

Ryzhkov, A., P. Zhang, Q. Cao, S. Matrosov, V. Melnikov, and M. Knight, 2014: Measurements of circular depolarization ratio with the radar with simultaneous transmission/reception. *8th European Conference on Radar in Meteorology and Hydrology, Garmisch-Partenkirchen, Germany, DWD and DLR, Extended Abstracts*, URL http://www.eecradar.com/pdf/EEC-CDR-Extended-Abstract.pdf.

Ryzhkov, A., P. Zhang, D. Hudak, J. Alford, M. Knight, and J. Conway, 2007: Validation of polarimetric methods for attenuation correction at c band. *Proc. 33rd Conf. Radar Meteorol.*

Ryzhkov, A., S. Y. Matrosov, V. Melnikov, D. Zrnic, P. Zhang, Q. Cao, M. Knight, C. Simmer, and S. Troemel, 2017: Estimation of depolarization ratio using weather

radars with simultaneous transmission/reception. *Journal of Applied Meteorology and Climatology*, **56 (7)**, 1797–1816, doi:10.1175/jamc-d-16-0098.1.

Ryzhkov, A. V., M. R. Kumjian, S. M. Ganson, and A. P. Khain, 2013a: Polarimetric radar characteristics of melting hail. part i: Theoretical simulations using spectral microphysical modeling. *Journal of Applied Meteorology and Climatology*, **52 (12)**, 2849–2870, doi:10.1175/jamc-d-13-073.1, URL http://dx.doi.org/10.1175/JAMC-D-13-073.1.

Ryzhkov, A. V., M. R. Kumjian, S. M. Ganson, and P. Zhang, 2013b: Polarimetric radar characteristics of melting hail. part II: Practical implications. *Journal of Applied Meteorology and Climatology*, **52 (12)**, 2871–2886, doi:10.1175/jamc-d-13-074.1, URL http://dx.doi.org/10.1175/JAMC-D-13-074.1.

Ryzhkov, A. V., T. J. Schuur, D. W. Burgess, P. L. Heinselman, S. E. Giangrande, and D. S. Zrnic, 2005a: The joint polarization experiment: Polarimetric rainfall measurements and hydrometeor classification. *Bulletin of the American Meteorological Society*, **86 (6)**, 809–824, doi:10.1175/bams-86-6-809, URL http://dx.doi.org/10.1175/BAMS-86-6-809.

Ryzhkov, A. V., T. J. Schuur, D. W. Burgess, and D. S. Zrnic, 2005b: Polarimetric tornado detection. *Journal of Applied Meteorology*, **44 (5)**, 557–570, doi:10.1175/jam2235.1.

Ryzhkov, A. V., and D. S. Zrnic, 2019: *Radar Polarimetry for Weather Observations*. Springer-Verlag GmbH, URL https://www.ebook.de/de/product/34744381/alexander_v_ryzhkov_dusan_s_zrnic_radar_polarimetry_for_weather_observations.html.

Schaefer, J. T., 1990: The critical success index as an indicator of warning skill. *Weather and Forecasting*, **5 (4)**, 570–575, doi:10.1175/1520-0434(1990)005<0570:tcsiaa>2.0.co;2.

Schmidt, M., S. Troemel, A. V. Ryzhkov, and C. Simmer, 2017: Severe hail detection: An adaptive algorithm for anomalous attenuation correction and new insights from scattering simulations at c-band. *38th Conference on Radar Meteorology, AMS, Chicago, IL, 28 Aug. 2017*, URL https://ams.confex.com/ams/38RADAR/meetingapp.cgi/Paper/320715.

Seltmann, J., and T. Böhme, 2017: Wind turbine issues in germany. *38th Conference on Radar Meteorology, AMS, Chicago, IL, 28 Aug. 2017*.

Snyder, J. C., A. V. Ryzhkov, M. R. Kumjian, A. P. Khain, and J. Picca, 2015: A ZDR column detection algorithm to examine convective storm updrafts. *Weather and Forecasting*, **30 (6)**, 1819–1844, doi:10.1175/waf-d-15-0068.1.

Tabary, P., G. Vulpiani, J. J. Gourley, A. J. Illingworth, R. J. Thompson, and O. Bousquet, 2009: Unusually high differential attenuation at C band: Results from a two-year analysis of the french trappes polarimetric radar data. *Journal of Applied Meteorology and Climatology*, **48 (10)**, 2037–2053, doi:10.1175/2009jamc2039.1.

Testud, J., E. Le Bouar, E. Obligis, and M. Ali-Mehenni, 2000: The rain profiling algorithm applied to polarimetric weather radar. *Journal of Atmospheric and Oceanic Technology*, **17 (3)**, 332–356, doi:10.1175/1520-0426(2000)017<0332:TRPAAT>2.0.CO;2, URL http://journals.ametsoc.org/doi/abs/10.1175/1520-0426(2000)017%3C0332:TRPAAT%3E2.0.CO;2.

Thiébaux, H. J., 1994: *Statistical Data Analysis for Ocean and Atmospheric Sciences*. Academic Press.

Thompson, E. J., S. A. Rutledge, B. Dolan, V. Chandrasekar, and B. L. Cheong, 2014: A dual-polarization radar hydrometeor classification algorithm for winter precipitation. *Journal of Atmospheric and Oceanic Technology*, **31 (7)**, 1457–1481, doi:10.1175/jtech-d-13-00119.1.

Trömel, S., M. R. Kumjian, A. V. Ryzhkov, C. Simmer, and M. Diederich, 2013: Backscatter differential phase—estimation and variability. *Journal of Applied Meteorology and Climatology*, **52 (11)**, 2529–2548, doi:10.1175/JAMC-D-13-0124.1, URL http://journals.ametsoc.org/doi/abs/10.1175/JAMC-D-13-0124.1.

Trömel, S., A. V. Ryzhkov, M. Diederich, K. Mühlbauer, S. Kneifel, J. Snyder, and C. Simmer, 2017: Multisensor characterization of mammatus. *Monthly Weather Review*, **145 (1)**, 235–251, doi:10.1175/mwr-d-16-0187.1.

Trömel, S., M. Ziegert, A. V. Ryzhkov, C. Chwala, and C. Simmer, 2014: Using microwave backhaul links to optimize the performance of algorithms for rainfall estimation and attenuation correction. *Journal of Atmospheric and Oceanic Technology*, **31 (8)**, 1748–1760, doi:10.1175/jtech-d-14-00016.1.

van Lier-Walqui, M., A. M. Fridlind, A. S. Ackerman, S. Collis, J. Helmus, D. R. MacGorman, K. North, P. Kollias, and D. J. Posselt, 2016: On polarimetric radar signatures of deep convection for model evaluation: Columns of specific differential phase observed during mc3e*. *Monthly Weather Review*, **144 (2)**, 737–758, doi:10.1175/mwr-d-15-0100.1.

Virtanen, P., R. Gommers, T. E. Oliphant, M. Haberland, T. Reddy, D. Cournapeau, E. Burovski, P. Peterson, W. Weckesser, J. Bright, S. J. van der Walt, M. Brett, J. Wilson, K. Jarrod Millman, N. Mayorov, A. R. J. Nelson, E. Jones, R. Kern, E. Larson, C. Carey, İ. Polat, Y. Feng, E. W. Moore, J. Vand erPlas, D. Laxalde, J. Perktold, R. Cimrman, I. Henriksen, E. A. Quintero, C. R. Harris, A. M. Archibald, A. H. Ribeiro, F. Pedregosa, P. van Mulbregt, and S. . . Contributors, 2020: SciPy 1.0: Fundamental Algorithms for Scientific Computing in Python. *Nature Methods*, **17**, 261–272, doi:https://doi.org/10.1038/s41592-019-0686-2.

Vivekanandan, J., S. M. Ellis, R. Oye, D. S. Zrnic, A. V. Ryzhkov, and J. Straka, 1999: Cloud microphysics retrieval using S-band dual-polarization radar measurements. *Bulletin of the american meteorological society*, **80 (3)**, 381–388, URL http://journals.ametsoc.org/doi/abs/10.1175/1520-0477(1999)080%3C0381:CMRUSB%3E2.0.CO%3B2.

Vulpiani, G., P. Tabary, J. P. du Chatelet, and F. S. Marzano, 2008: Comparison of Advanced Radar Polarimetric Techniques for Operational Attenuation Correction at C Band. *Journal of Atmospheric and Oceanic Technology*, **25 (7)**, 1118–1135, doi:10.1175/2007JTECHA936.1, URL http://journals.ametsoc.org/doi/abs/10.1175/2007JTECHA936.1.

Wakimoto, R. M., and V. N. Bringi, 1988: Dual-polarization observations of microbursts associated with intense convection: The 20 july storm during the MIST project. *Monthly Weather Review*, **116 (8)**, 1521–1539, doi:10.1175/1520-0493(1988)116<1521:dpooma>2.0.co;2.

Waldvogel, A., B. Federer, and P. Grimm, 1979: Criteria for the detection of hail cells. *Journal of Applied Meteorology*, **18 (12)**, 1521–1525, doi:10.1175/1520-0450(1979)018<1521:cftdoh>2.0.co;2.

Walt, S. v. d., S. C. Colbert, and G. Varoquaux, 2011: The numpy array: a structure for efficient numerical computation. *Computing in Science & Engineering*, **13 (2)**, 22–30, doi:10.1109/MCSE.2011.37.

Wang, Y., and V. Chandrasekar, 2009: Algorithm for estimation of the specific differential phase. *Journal of Atmospheric and Oceanic Technology*, **26 (12)**, 2565–2578, doi:10.1175/2009jtecha1358.1.

Warren, S. G., 1984: Optical constants of ice from the ultraviolet to the microwave. *Applied optics*, **23 (8)**, 1206–1225.

Waterman, P. C., 1971: Symmetry, unitarity, and geometry in electromagnetic scattering. *Physical Review D*, **3 (4)**, 825–839, doi:10.1103/physrevd.3.825, URL https://doi.org/10.1103%2Fphysrevd.3.825.

Witt, A., D. W. Burgess, A. Seimon, J. T. Allen, J. C. Snyder, and H. B. Bluestein, 2018: Rapid-scan radar observations of an oklahoma tornadic hailstorm producing giant hail. *Weather and Forecasting*, **33 (5)**, 1263–1282, doi:10.1175/waf-d-18-0003.1.

Witt, A., M. D. Eilts, G. J. Stumpf, J. Johnson, E. D. W. Mitchell, and K. W. Thomas, 1998a: An enhanced hail detection algorithm for the wsr-88d. *Weather and Forecasting*, **13 (2)**, 286–303.

Witt, A., M. D. Eilts, G. J. Stumpf, E. D. W. Mitchell, J. T. Johnson, and K. W. Thomas, 1998b: Evaluating the performance of WSR-88d severe storm detection algorithms. *Weather and Forecasting*, **13 (2)**, 513–518, doi:10.1175/1520-0434(1998)013<0513:etpows>2.0.co;2.

Wolfensberger, D., D. Scipion, and A. Berne, 2015: Detection and characterization of the melting layer based on polarimetric radar scans. *Quarterly Journal of the Royal Meteorological Society*, **142**, 108–124, doi:10.1002/qj.2672.

Zadeh, L., 1965: Fuzzy sets. *Information and Control*, **8 (3)**, 338–353, doi:10.1016/s0019-9958(65)90241-x.

Zeng, Y., U. Blahak, and D. Jerger, 2016: An efficient modular volume-scanning radar forward operator for NWP models: description and coupling to the COSMO model. *Quarterly Journal of the Royal Meteorological Society*, **142 (701)**, 3234–3256, doi:10.1002/qj.2904.

Zhang, G., 2016: *Weather Radar Polarimetry*. CRC Press.

Ziegler, C. L., P. S. Ray, and N. C. Knight, 1983: Hail growth in an oklahoma multicell storm. *Journal of the Atmospheric Sciences*, **40 (7)**, 1768–1791, doi:10.1175/1520-0469(1983)040<1768:hgiaom>2.0.co;2.

Zrnić, D. S., A. Ryzhkov, J. Straka, Y. Liu, and J. Vivekanandan, 2001: Testing a procedure for automatic classification of hydrometeor types. *Journal of Atmospheric and Oceanic Technology*, **18 (6)**, 892–913, doi:10.1175/1520-0426(2001)018<0892:tapfac>2.0.co;2.

Zrnić, D. S., and A. V. Ryzhkov, 1999: Polarimetry for Weather Surveillance Radars. *Bulletin of the American Meteorological Society*, **80 (3)**, 389–406, doi:10.1175/1520-0477(1999)080<0389:PFWSR>2.0.CO;2, URL http://journals.ametsoc.org/doi/abs/10.1175/1520-0477%281999%29080%3C0389%3APFWSR%3E2.0.CO%3B2.

Acknowledgements

I hereby want to express my gratitude towards my supervisors, Silke Trömel and Clemens Simmer for giving me the opportunity to research on this topic and their supervision. I value their positive criticism, teaching and the time they spent with me - in and outside of the university - very much. Both always had an open door for me and an open mind for my ideas. I appreciate their effort they made for helping me out, the fruitful discussions and the witty and amusing social events. Joining them on conferences was always a very interesting and memorable time for me, on a scientific, but also on a social level. Thank you!

I would like to thank Alexander V. Ryzhkov for his expert information and guidance. Be it either remote or in person, he always had time to lend his expertise and opinion. I would also like to thank him for the opportunity to stay for several weeks at the University of Oklahoma (OU) and sharing the dual-layered T-matrix scattering code.

The formerly meteorological institute of the university of Bonn was always a welcoming and lively place to work for me. I would like to thank all of my colleagues who made the institute not only a nice place to be, but also a place where friends are. Instead of adding many names, I would like to point out a few persons, who I think deserve to hear a "thank you" more often. Especially, I would like to thank the secretaries Anne Debus and Ingeborg Rassow who always supported me and provided helpful information, no matter what kind of bureaucratic problem one had to face. Also, these thanks go to Lucias Hallas, who kept the library heart-warmingly welcoming and always knew good places to enjoy tea and nice chats.

A special thanks goes to my friends and partner, who always supported me and carried me throughout stressful times. Their love and care helped me a lot and made this thesis, among many other things in my life, possible.

During conferences I had the opportunity to meet many interesting scientists and join exciting talks. Among others, I would like to thank Joshua Sonderholm for his opinions on nowcasting methods and the many refreshing chats, Jeffrey Snyder for exchanging information about T-matrix scattering, Becky Adams-Selin for sharing the HAILCAST model code, Maike Hacker for helping out with obtaining NWP data, Pengfei Zhang for providing collocated S- and C-band radar data of a thunderstorm in Alabama, and Rudolf Kaltenböck for providing radar data of a tornadic event in Austria.

The Integrated Research Training Group (IRTG) of the Transregional Collaborative Research Centre 32 (TR32) provided excellent opportunities for scientific exchange, organized special workshops and funded the stay abroad at the University of Oklahoma (OU). Being part of their activities was always pleasant and I am thankful for their support.

I would like to thank all contributors to free and open-source software, datasets and publications, who have dedicated so much of their time and passion. I hereby

acknowledge my deepest gratitude for their work. Some of the used, free and open-source software is named in the following: Almost all the programming and research was done using the programming language *Python*[1]. Especially, *IPython*[2] and the *IPython notebook* environment, in which most of the development and scientific investigation was done, the modules *NumPy*[3] and *SciPy*[4] for numerical and scientific algorithms and computations, *ωradlib*[5] for reading and processing radar data, *h5py*[6] for reading model output and *Matplotlib*[7] for plotting were used and very helpful. *Tex Studio*[8] as interactive development environment for LaTeX code, *Language Tool*[9] for spell checking, and the version control system *GIT*[10] were used. Furthermore, I would like to thank the users and the network of *Stackexchange*[11] for great discussions and helpful solutions on many Python, LaTeX and other issues.

The research done would not have been possible without the data from the European Severe Weather Database (ESWD, https://www.eswd.eu). The polarimetric radar data was kindly provided by the German national meteorological service (DWD). The research project was funded by the DWD via its extramural research program, grant 2015EMF-7.

Thank you all and thank YOU for reading!

[1] Python Software Foundation, http://www.python.org, version 2.7.16
[2] Pérez and Granger (2007), https://ipython.org/, version 5.8.0
[3] Walt et al. (2011), http://www.numpy.org/, version 1.16.5
[4] Virtanen et al. (2020), http://www.scipy.org/, version 1.2.1
[5] Heistermann and Pfaff (2013), https://docs.wradlib.org/en/stable/, version 1.0.0
[6] Andrew Collette and contributors, http://www.h5py.org, version 2.5.0
[7] Hunter (2007), http://matplotlib.org/, version 2.2.2
[8] Benito van der Zander and contributors, http://www.texstudio.org/, version 2.12.14
[9] LanguageTool community and Daniel Naber, http://www.languagetool.org, version 4.1
[10] Junio Hamano, Linus Torvalds, among others, https://git-scm.com/, version 2.20.1
[11] Stack Exchange Inc., http://stackexchange.com/

BONNER METEOROLOGISCHE ABHANDLUNGEN

Herausgegeben vom Institut für Geowissenschaften der Universität Bonn, Abteilung Meteorologie, durch Prof. Dr. H. FLOHN (Hefte 1-25), Prof. Dr. M. HANTEL (Hefte 26-35), Prof. Dr. H.-D. SCHILLING (Hefte 36-39), Prof. Dr. H. KRAUS (Hefte 40-49), ab Heft 50 durch Prof. Dr. A. HENSE.

Heft 1-69: siehe `http://www.meteo.uni-bonn.de/bibliothek/bma`

70-91: open access, verfügbar unter `https://bonndoc.ulb.uni-bonn.de/xmlui/handle/20.500.11811/1627`

Heft 70: ***A S M Mostaquimur Rahman***: Influence of subsurface hydrodynamics on the lower atmosphere at the catchment scale, 2015, 98 S. + XVI.

Heft 71: ***Sabrina Wahl***: Uncertainty in mesoscale numerical weather prediction: probabilistic forecasting of precipitation, 2015, 108 S.

Heft 72: ***Markus Übel***: Simulation of mesoscale patterns and diurnal variations of atmospheric CO_2 mixing ratios with the model system TerrSysMP-CO_2, 2015, [erschienen] 2016, 158 S. + II

Heft 73: ***Christian Bernardus Maria Weijenborg***: Characteristics of Potential Vorticity anomalies associated with mesoscale extremes in the extratropical troposphere, 2015, [erschienen] 2016, 151 S. + XI

Heft 74: ***Muhammad Kaleem***: A sensitivity study of decadal climate prediction to aerosol variability using ECHAM6-HAM (GCM), 2016, 98 S. + XII

Heft 75: ***Theresa Bick***: 3D Radar reflectivity assimilation with an ensemble Kalman filter on the convective scale, 2016, [erschienen] 2017, 96 S. + IX

Heft 76: ***Zied Ben Bouallegue***: Verification and post-processing of ensemble weather forecasts for renewable energy applications, 2017, 119 S.

Heft 77: ***Julia Lutz***: Improvements and application of the STatistical Analogue Resampling Scheme STARS, 2016, [erschienen] 2017, 103 S.

Heft 78: ***Benno Michael Thoma***: Palaeoclimate Reconstruction in the Levant and on the Balkans, 2016, [erschienen] 2017, XVI, 266 S.

Heft 79: ***Ieda Pscheidt***: Generating high resolution precipitation conditional on rainfall observations and satellite data, 2017, V, 173 S.

Heft 80: ***Tanja Zerenner***: Atmospheric downscaling using multi-objective genetic programming, 2016, [erschienen] 2017, X, 191 S.

Heft 81: ***Sophie Stolzenberger***: On the probabilistic evaluation of decadal and paleoclimate model predictions, 2017, IV, 122 S.

Heft 82: ***Insa Thiele-Eich***: Flooding in Dhaka, Bangladesh, and the challenge of climate change, 2017, V, 158 S.

Heft 83: ***Liselotte Bach***: Towards a probabilistic regional reanalysis for Europe, 2017 [erschienen] 2018, VI, 114 S.

Heft 84: ***Yen-Sen Lu***: Propagation of land surface model uncertainties in terrestrial system states, 2017, [erschienen] 2018, X, 120 S.

Heft 85: ***Rüdiger Hewer***: Stochastic physical models for wind fields and precipitation extremes, 2018, 99 S.

Heft 86: ***Sebastian Knist***: Land-atmosphere interactions in multiscale regional climate change simulations over Europe, 2018, VIII, 147 S.

Heft 87: ***Jessica Keune***: Integrated terrestrial simulations at the continental scale: Impact of groundwater dynamics and human water use on groundwater-to-atmosphere feedbacks during the European heatwave in 2003, 2019, IX, 172 S.

Heft 88: ***Christoph Beekmans***: 3-D Cloud Morphology and Evolution Derived from Hemispheric Stereo Cameras, 2019, [erschienen] 2020, VIII, 118 S.

Heft 89: ***Nils Weitzel***: Climate field reconstructions from pollen and macrofossil syntheses using Bayesian hierarchical models, 2019, [erschienen] 2020, XII, 153 S.

Heft 90: ***Alexander Kelbch***: Investigations to quantify individual exposure to solar ultraviolet erythemal radiation including cloud meteorological impact, 2020, III, 107 S.

Heft 91: ***Mari L. Schmidt***: Improvement of hail detection and nowcasting by synergistic combination of information from polarimetric radar, model predictions, and in-situ observations, 2020, IV, 136 S.

INSTITUT FÜR GEOWISSENSCHAFTEN
ABTEILUNG METEOROLOGIE
MATHEMATISCH NATURWISSENSCHAFTLICHE FAKULTÄT
UNIVERSITÄT BONN

institut für
geowissenschaften
METEOROLOGIE